

The final 20-Layer-Prototype for the AMS Transition Radiation Detector: Beamtests, Data-Analysis, MC-Studies

Von der Fakultät für Mathematik, Informatik und Naturwissenschaften der
Rheinisch-Westfälischen Technischen Hochschule Aachen
zur Erlangung des akademischen Grades eines
Doktors der Naturwissenschaften
genehmigte Dissertation

vorgelegt von

Diplom-Physiker
Jörg Orboeck

aus Vechta

Diese Dissertation ist auf den Internetseiten der Hochschulbibliothek online verfügbar.

Berichter: Universitätsprofessor Dr. S. Schael
 Professor Dr. W. Wallraff

Tag der mündlichen Prüfung: 28. Mai 2003

Abstract

The work at hand deals with all the concerns of the final 20-layer prototype for the AMS TRD, which has been subjected to 2 high energy beamtest at CERN test facilities (X7,H6) in summer 2000. During these beamtests more than 3 million events of p^+ , e^- , π^- and μ^- data with beam energies up to 250 GeV have been recorded. The analysis of the measured data has determined the rejection factor for protons and pions against electrons as function of particle energy. In order to do so the frequently used Cluster Counting as well as three different Likelihood methods have been used. The best performance likelihood derived rejection factors for protons in the range from (1429 ± 408) at 20 GeV down to (143 ± 12) at 250 GeV beam energy. This same analysis carried out for the pion data results in rejections that range from (1000 ± 400) at 20 GeV beam energy up to (19.2 ± 0.7) at 100 GeV . This denotes on average an improvement by more than a factor of 2, compared to the Cluster Counting results.

In the second part of this thesis, GEANT 3.21 simulations have been employed to reproduce the measured energy spectra and rejection factors. For that reason existing GEANT supplements to generate and detect transition radiation have been adjusted and optimised such, that a best agreement to the measured energy spectra was achieved over the full range of proton energies. Rejection factors derived from MC samples are in good agreement with those from the data over the full range of pion energies. Above 160 GeV though this comparison at first depicted a clear discrepancy between the data and MC proton rejection distributions. An additionally introduced simple model of diffractive proton proton interactions was capable of resolving this discrepancy up to the highest measured beam energies. Other attempts to resolve this disagreement failed to follow suit.

Contents

1	Introduction	1
2	The AMS Experiment	5
2.1	Physics Goals	7
2.1.1	Search for Antimatter ($Z \geq 2$)	7
2.1.2	Search for Dark Matter	9
2.1.3	Further Research Goals	14
2.2	The AMS Detector	14
2.2.1	Silicon Tracker and Alignment	16
2.2.2	Superconducting Magnet	16
2.2.3	Anti-Coincidence Counter (ACC)	17
2.2.4	Time of Flight System (ToF)	17
2.2.5	Ring Imaging Čerenkov Counter (RICH)	18
2.2.6	Electromagnetic Calorimeter (Ecal)	18
2.2.7	Transition Radiation Detector (TRD)	19
3	The AMS Transition Radiation Detector	21
3.1	Transition Radiation	21
3.1.1	The Formation Zone	23
3.1.2	The Radiation Yield	24
3.1.3	Radiator	25
3.2	Transition Radiation Detection	26
3.2.1	dE/dx Energy Loss	26
3.2.2	Photon Detection	27
3.2.3	The gasfilled Proportional Chamber	31
3.3	The AMS Transition Radiation Detector	32
3.3.1	Radiator	33
3.3.2	Straw Module	33
3.3.3	Electronics and DAQ	34
3.3.4	Gas Supply System	36
3.3.5	Mechanical Support Structure	37
3.3.6	”Structural Verification”	38
3.3.7	Thermal Model	39
4	The TRD Prototype	41
4.1	Laboratory Preparations	41
4.1.1	Gas Gain Measurements	44

4.2	The 20-Layer Prototype	49
4.2.1	The TRD Parameter Choice	49
4.2.2	Mechanical Layout	50
4.3	Beamtests of the TRD Prototype	53
4.3.1	General Set-up	53
4.3.2	The X7-Beamline	55
4.3.3	The H6-beamline	56
5	Data Analysis	59
5.1	Data Preparation	59
5.1.1	Track Reconstruction and Event Selection	60
5.1.2	Channel-by-Channel Inter-Calibration	62
5.1.3	Gas Gain Correction	64
5.1.4	Energy Calibration	64
5.2	Radiator Test	66
5.3	Proton Rejection Analysis	67
5.3.1	Cluster Counting Method	69
5.3.2	Likelihood Method	72
5.4	Pion & Muon Rejection Analysis	78
5.4.1	Rejection versus Lorentz Factor	79
6	Monte Carlo Simulations	81
6.1	The GEANT Software and its Supplements	81
6.1.1	Simulation of dE/dx in low Density Gases	82
6.1.2	The Simulation of TR	83
6.2	Real Detector Monte Carlo	83
6.2.1	Mechanical Setup	83
6.2.2	Readout Electronics	85
6.2.3	First MC Simulations	86
6.3	MC Parameter Optimisation	87
6.3.1	dE/dx Adjustment	87
6.3.2	Adjustment of TR	89
6.4	MC Rejection Analysis Results	93
6.4.1	Cluster Counting Analysis	94
6.4.2	Likelihood Analysis	96
6.4.3	A possible Solution: Diffractive Proton Dissociation	98
7	Conclusion	101
	Acknowledgement	105
	List of Figures	108
	List of References	109
	Curriculum Vitae	114

Chapter 1

Introduction

Outer space, and its cosmic rays, have always been a very powerful natural laboratory for physics research. From ancient history on, mankind has been fascinated by the view of the night sky. In the 16th century Kepler found some of the first hints on gravitation and classical mechanics in planetary motion by his detailed observations of the solar system. Kepler's laws combined with his own three laws of motion enabled Newton to find his famous *law of general gravitation*. This is well known and understood today and generalized by *The General Theory of Relativity* invented by Einstein at the beginning of the 20th century. In addition to solving some of the mysteries of astronomy of that time, it predicted many new phenomena like the existence of gravitational waves and the expansion of the universe [1].

With highly sophisticated technologies, such as the Hubble Space Telescope (HST), astronomers today are able to reach deep into space and gain information and spectacular pictures from even far remote interstellar objects. Figure 1.1 for example shows the encounter of the two spiral galaxies NGC 2207 and IC 2167. The distance to these objects is 35 *Mpc* and the image was taken with the "Wide Field Planetary Camera 2" of HST.

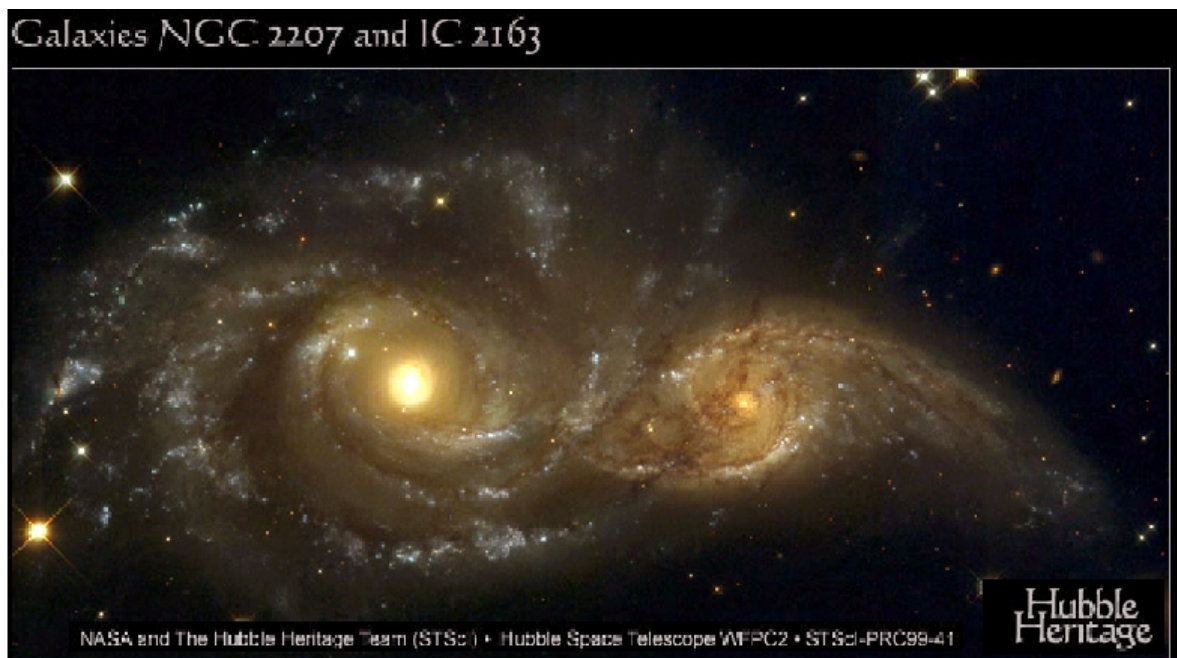


Figure 1.1: *The grazing encounter of the two spiral galaxies NGC 2207 and IC 2163 [2].*

The Origin of the Universe Further observations and experiments, that make use of these technologies, have tested the existing laws of physics, confirmed Einstein's predictions, and even extended our knowledge of science and astronomy in particular and of nature in general. We know today that the universe expands and believe that this expansion originates from a huge explosion at the beginning of space and time, the so called *Big Bang*. The experimental evidence of a 2.7 K blackbody radiation, first found in 1964 and referred to today as *Cosmic Microwave Background Radiation (CMBR)*, the reputed remnant of this explosion, strongly supports this view of the Big Bang as the origin of the universe.

Large Scale Structures In defiance of this conclusive evidence all Big Bang scenarios reveal new puzzles when combined with further observations. The detailed study of the CMBR at the end of last century by experiments like COBE¹ has shown the smoothness of this cosmic background radiation with temperature fluctuations on a scale of $\delta T/T \sim 10^{-5}$ only. This observation seemed to be inconsistent with the commonly known large scale structures of matter in the universe like galaxies, and even clusters of them. With the theory of inflation, which foresees a short period ($10^{-32}s$) of an exponentially expanding universe, cosmologists seem to have found a way to solve this contradiction [1, 3, 4].

Dark Matter More such questions and puzzles of various different kinds still remain unanswered. One of those major unsolved astrophysical problems deals with the existence and identification of unseen mass (referred to as *dark matter*) – responsible for certain characteristics of galactic rotational velocity curves, for instance – and this dark matter's share in the mass of the whole universe. One of the formerly promising candidates to have a large share in this dark matter mass was the neutrino. Several different underground experiments, like "Superkamiokande" located in Japan, have provided us with profound insights into cosmic neutrino physics. However, the existing upper mass limits on the three neutrino generations rule them out as the only dark matter contribution. The theory of Supersymmetry provides another promising candidate, the Neutralino, that is believed to build halos around galaxies. It is this possible SUSY contribution to the dark matter that AMS will focus its search on [5].

Cosmic Antimatter? Another major unsolved problem in astrophysics is that of the predominance of matter in an astronomical region of at least 20 *Mpc* around our *Milky Way Galaxy*. Whereas modern particle physics states that particles must have been produced in matter-antimatter pairs of even numbers out of the high energetic universe of that early era. In that sense primordial antimatter particles, identical to their matter counterparts but with opposite attributes, such as the electric charge, are supposed to exist, somewhere far away in the universe, in same amounts than the matter we all exist off.

Cosmic Radiation Answers to these and further puzzles of astrophysics may be found in a detailed study of the *Cosmic Radiation*, a flux of high energetic charged particles that strikes Earth's atmosphere. Those cosmic rays may carry a small amount of primordial antimatter and/or new particles so far unknown, or at least never detected. Energy spectra of the major components of these cosmic rays, predominantly protons, plus a comparison with predictions, offers the chance to find evidence for so far unknown types of dark matter, and to explore new, and so far unimagined phenomena.

¹COSmic Background Explorer

Cosmic Ray Spectroscopy However, up to now no long term and high precision measurement of these charged cosmic rays has been carried out. This is because charged particles interact with Earth's atmosphere, which means that the primary cosmic ray particles cannot be detected on Earth's surface. Therefore, measurements of that kind have to be carried out outside the atmosphere's zone of influence. To distinguish between the various kinds of charged particles that cosmic rays consist of, a magnetic spectrometer equipped with various special supplements is required. Up to now such a device has never been operated in space for periods of more than a few days.

ISS The International Space Station (ISS), which is currently under construction, provides the chance to realise a project like that. This platform can supply power, mechanical support and stability as well as the necessary infrastructure in space, needed for a high precision and long term experiment like AMS.

AMS The Alpha Magnetic Spectrometer (AMS) Experiment will be the first large acceptance particle detector operated in space for a duration of 3 years. By utilizing the knowledge and the state of the art technologies developed in modern particle physics, AMS will measure and identify charged particles as well as high energetic gamma rays. In order to do so, detector components similar to those used in terrestrial high energy physics experiments are adapted to be operated under the harsh environmental conditions, such as the extreme and drastically changing temperatures or the almost perfect vacuum, outside Earth's atmosphere.

Search for SUSY Dark Matter Particularly for the search for supersymmetric particles in the universe, one has to look for the annihilation or decay products of the mentioned Neutralinos. The best candidates for such investigations appear to be positrons and anti-protons, since the backgrounds for these two type of particles in cosmic rays are known to be lowest compared to all other major components. At high energies, unfortunately, a tracking device alone can not distinguish between positrons and proton particles anymore. To pursue precision positron spectroscopy one still has to tell those light from heavy particles up to particle energies of ~ 300 GeV. For such purposes it is best to use a combination of an electromagnetic calorimeter (Ecal) and a Transition Radiation Detector (TRD), for cases where high separation powers are needed. Such a combination of detector components will come into operation in the AMS experiment. Taking into account the flux ratio of protons (p^+) and positrons (e^+) of a factor of $\sim 10^4$, one will easily understand that a e^+/p^+ separation power of better than 10^6 is necessary to accumulate a high precision cosmic positron energy spectrum. The TRD will contribute to this separation power with a rejection factor of better than 10^2 up to 250 GeV proton energy.

This Work The AMS TRD is being built by an international group of institutes under the leadership of the I. Physikalisches Institut of RWTH Aachen. The scientific work at hand deals with all the concerns of the final 20-layer-prototype for the TRD built and tested in Aachen, and subjected to 2 high energy beamtests at CERN, in summer 2000. More than 3 million electron, muon, pion and proton events have been recorded during these beamtests, carried out at the CERN X7- and H6-beamlines.

The major part of this work focuses on the analysis of the data taken, the Monte Carlo (MC) simulations of those measurements, and the necessary MC optimisation. It will result in detailed information on the e^+/p^+ separation power of the TRD foreseen for the AMS Experiment, confirmed by results from detailed Monte Carlo simulation studies.

Chapter 2

The AMS Experiment

The main goal of the Alpha Magnetic Spectrometer (AMS) Experiment is to precisely explore and study the components and dynamics of the Cosmic Radiation. By doing so AMS is making use of all the state of the art technologies developed for and used in present day particle physics experiments. The first of the major concerns in this research project is to find Antimatter ($Z \geq 2$). In this concern, even a small number of detected anti-carbon (\bar{C}) nuclei would lead to the conclusion that at least a whole star, like our sun, made out of antimatter once existed in a region of the universe far remote from Milky Way and apart from any large amount of matter. AMS will look for such antiparticles itself, as well as high energetic gamma rays, produced from matter-antimatter annihilations in a transition region between matter and antimatter domains of the universe.

The second major aim to study the cosmic radiation in detail, is to find hints on further components of dark matter. As an extra of doing so, an answer to a still unsolved question of today's high energy physics might be found. If observations would provide an indication for "Supersymmetric" particles, like Neutralinos (χ), one could answer the question about the existence of Supersymmetry and find another contribution to dark matter at a stroke. AMS is trying to do so by precisely practicing positron spectroscopy. The identification of a positron surplus in a certain energy range, as first hints for were observed by the HEAT Experiment [6], would give evidence on possible $\chi\bar{\chi}$ annihilation processes in the halo of our galaxy. A third objective target for AMS is to explore new and unknown phenomena. For these purposes the AMS experiment, with its large acceptance, is going to take data outside Earth's atmosphere, attached to the International Space Station (ISS), for a period of 3 years at an altitude of ~ 400 km. The shuttle launch for AMS is currently scheduled for late 2005. Figure 2.1 shows the experiment's position on board the ISS.

The International Space Station The "exciting gateway to new frontiers" as NASA¹ calls the International Space Station is based on a 88.4 m girder as its centerpiece. At both ends of this main support beam solar panels are attached with an overall area of more than 4000 m². They supply the electrical power to the whole station. In the center of this main girder, space for 6 full-sized laboratory, additional astronauts accommodation and service modules is available. Mounted to this same truss, shifted out from the center, AMS will come to operation. At an average operating altitude of 407 km and an inclination of 51.6 degrees to the Equator, 85 % of Earth's surface is observable from the ISS.

¹National Aeronautics and Space Administration

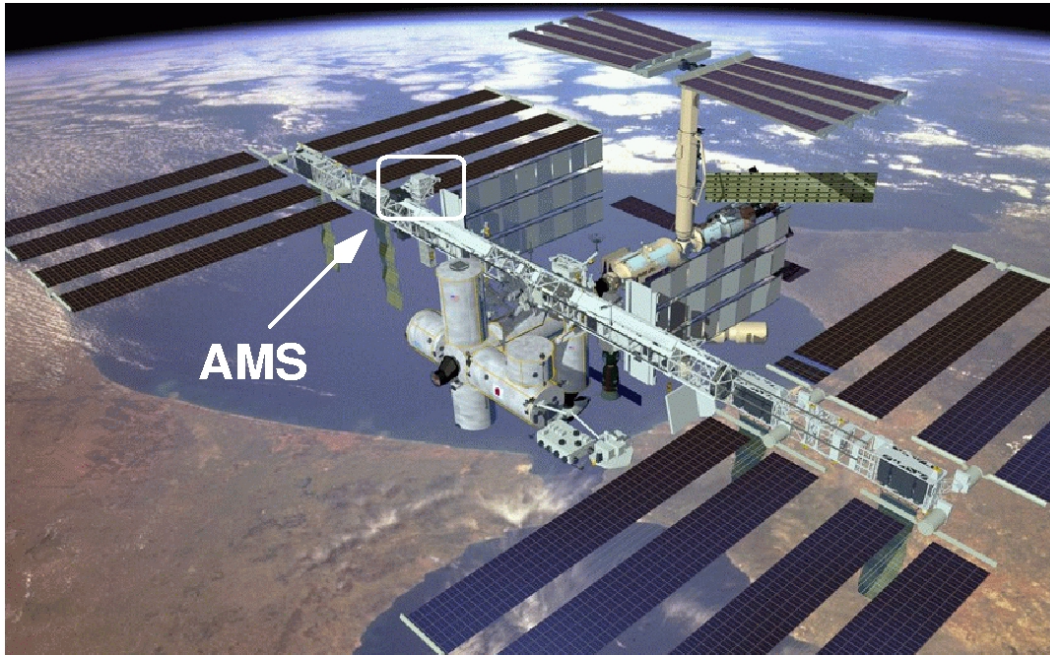


Figure 2.1: *The AMS-Detektor on board the ISS [7].*

The ISS assembly already started in November 1998 and since November 2000 a permanent crew of at least 3 astronauts is in orbit. In October 2004 the contribution of the European Space Agency (ESA), the "Columbus" module, will be deployed to orbit and according to current NASA schedules the ISS assembly will be complete by April 2006 [8].

During the three years operation time on board the ISS, AMS will benefit from its orbit at high altitude and thus negligible atmospheric disturbances². AMS' additional large acceptance³ of $\sim 0.5 \text{ m}^2\text{sr}$ will gain insights into the cosmic radiation with unmatched precision. For example, the search for antimatter will either be successful or at least extend the existing exclusion limits by 3 to 4 orders of magnitude. In doing so, AMS' reach into space will exceed a distance of 150 *Mpc* [9].

The AMS' Predecessors The predecessors to AMS are mainly balloon experiments like HEAT ([6]) and BESS ([10]), which both made use of similar apparatus like a superconducting magnet or in the HEAT case a TRD. In comparison with AMS, their disadvantages are their lower altitude of about 40 *km*, a short measurement time of about 24 hours for each measurement campaign, and a smaller acceptance of no more than $0.3 \text{ m}^2\text{sr}$ in the BESS case. Already a major step forward was the precursor flight of AMS, a feasibility study called AMS-01, with the spaceship "Discovery" in 1998. The data taken during these 10 days exposure to the cosmic radiation, improved the current exclusion limits, concerning the search for antimatter, by more than one order of magnitude [11].

The next step forward in the exploration of cosmic radiation will be the PAMELA Experiment [12]. PAMELA will take data for a period of three years on a Russian satellite with an average altitude of 500 *km* on an elliptical orbit. It has a similar detector layout as AMS with a TRD, an Ecal and a magnetic spectrometer as its centerpiece. The only important difference is the rather small acceptance of only $0.0021 \text{ m}^2\text{sr}$.

²the impact on the measur. by interact. of the cosmic rays with molecules of the rem. atmosphere.

³For e^+ spectroscopy this accept. is reduced to $\sim 0.05 \text{ m}^2\text{sr}$, due to the limited size of the Ecal.

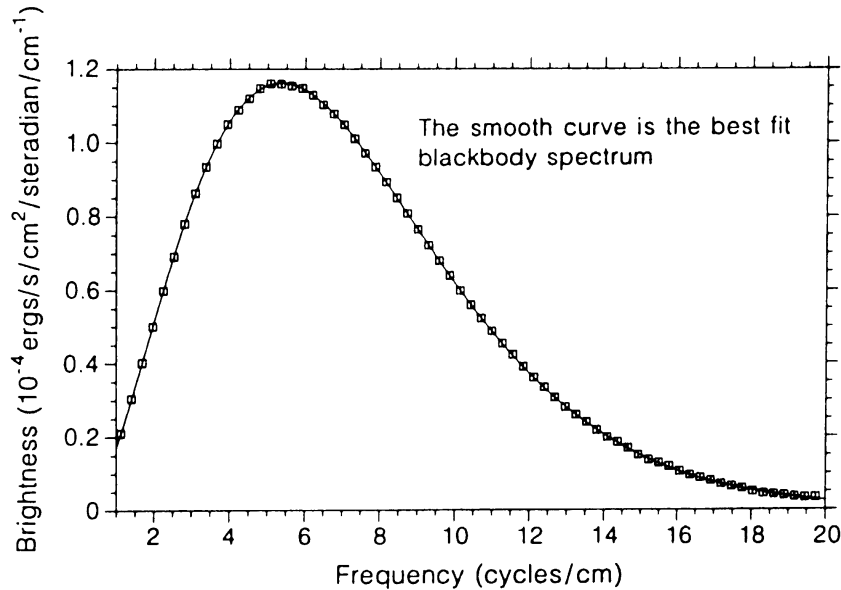


Figure 2.2: The COBE measurement of the CMBR 2.73 K blackbody spectrum [1].

2.1 Physics Goals

2.1.1 Search for Antimatter ($Z \geq 2$)

Already in 1920 E. Hubble found the first evidence for an expanding universe, predicted by Einstein's *General Theory of Relativity*. At the latest after the discovery of the Cosmic Microwave Background Radiation (CMBR) in 1964 by two "Bell Labs" engineers (A. Penzias and R. Wilson) a great majority of physicists was finally convinced that the universe was given birth by a huge explosion, referred to today as the "Big Bang". The CMBR seems to be a perfect blackbody radiation of 2.73 K temperature and the last remnant of this Big Bang explosion. The COBE⁴ Experiment, among other important observations, has precisely measured the spectrum of the CMBR as figure 2.2 shows [1].

According to this theory of the Big Bang, the universe emerged from a point-like singularity with infinite energy density and is ever since expanding. With the increasing size of the universe its energy density decreased and thus its temperature dropped down to the current value of the CMBR. During this expansion, as a result of homogeneity fluctuations, structures on large scales like galaxies, and even clusters of them, were formed. The development of the universe according to this theory is portrayed in figure 2.3 [13].

Contradictory to this conclusive evidence all Big Bang scenarios reveal new puzzles when combined with further observations. The puzzle about the smoothness of the Cosmic Background Radiation, as mentioned in the preface, found a theoretical solution. However, so far no experimental evidence for or against the theory of inflation has been found. Other puzzles and contradictions still seek for explanation. Reasons for the almost perfect flatness of the universe, for instance, are not yet found.

Observations of the universe, surrounding us, have come to the conclusion that a region of at least 20 *Mpc* radius around the Milky Way Galaxy is entirely matter dominated. Considering the theory of the Big Bang and the Standard Model (SM) of particle physics, all of the particles in our universe today originate from the burst of particle-antiparticle production that was fueled by the energy released at the end of the inflation period.

⁴Cosmic Background Explorer

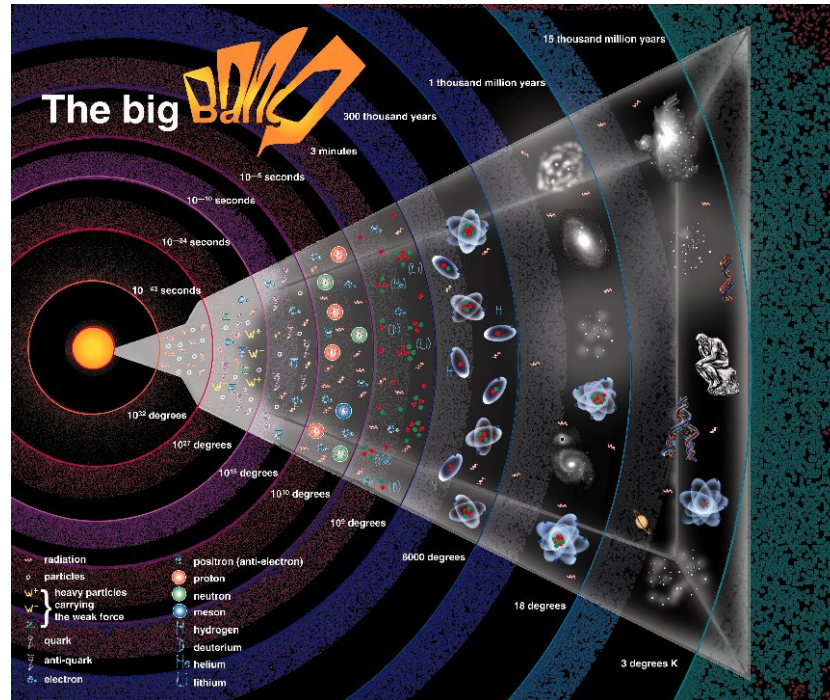


Figure 2.3: *The development of the universe from the Big Bang until today [13].*

The fate of the antimatter, produced in that early era, still asks cosmologists riddles. Do clusters of galaxies made of antimatter exist somewhere far away from Milky Way or is antimatter simply extinguished right after its creation during the first Femtosecond after the Big Bang? Both parts of this question could solve the puzzle and both scenarios have their supporters.

Matter-Antimatter Symmetry As early as 1933 P. Dirac, who first predicted the existence of antiparticles, summarized his view on cosmic antimatter in his Nobel Lecture as follows [14]:

“... we must regard it rather as an accident that the Earth ... contains a preponderance of negative electrons and positive protons. It is quite possible that for some of the stars it is the other way about, In fact there may be half the stars of each kind ... and there would be no way of distinguishing them from present astronomical methods.”

This last statement is only partly true today. But even at present time only one way exists to acquire evidence for cosmic antimatter. That is to “fish” for primordial antimatter particles in the “broth” of cosmic rays. Whilst there is a large number of secondary antiprotons from interactions of high energetic cosmic rays with the interstellar medium, it is to more than 50 orders of magnitude excluded to find secondary antiparticles ($Z \geq 2$) within the cosmic rays, produced in such collisions with the interstellar medium [15]. That means, detecting such antiparticles would give rise to the assumption, that a whole domain of antimatter exists somewhere far remote from our matter dominated region. But what could have separated matter and antimatter that far? The answer again could be inflation. For some reason matter and antimatter could have clustered separately right after their creation and the inflationary era has parted them by great distance [1, 3, 4].

Matter-Antimatter Asymmetry A variety of so called Grand Unified Theories (GUT) of particle physics exists, that try to find ways to unify all four fundamental forces in an extension to the success of combining electromagnetic and weak forces. Some of those GUTs explain the total absence of antimatter as a result of a slight asymmetry in the production of quarks and antiquarks out of hypothetical X particles. The photons of the CMBR are, according to this hypothesis, the products of the annihilation processes of the "symmetric numbered" particles and antiparticles. Out of those remaining unpaired baryons, one for every billion annihilated baryon-antibaryon pairs, the entire baryonic type matter in the present universe was formed. A more detailed analysis results even in a plausible explanation of the so called baryonic number of the universe⁵, a number as small as 10^{-10} [4].

Three Fundamental Conditions In 1967 the Russian physicist A. Sakharov pointed out that three fundamental conditions are necessary for such a baryon genesis. First, the universe must be out of equilibrium. This is a natural consequence of the expansion of the universe. Second, the conservation of the baryon number⁶ must be violated. From modern particle physics we know, that this quantum number is strictly conserved (upper limit: p^+ lifetime $\tau_p > 10^{31}y$ [16]). But during the epoch of grand unification, 10^{-35} seconds after the Big Bang, where particles had thermal energies exceeding 10^{15} GeV, it is conceivable that this conservation did not hold. The third crucial condition is the CP-violation, that means the combined conservation of the two properties called "charge conjugation C" and "parity P" must be violated. This violation was experimentally found in Kaon and B-Meson decays. Experiments on these decays have worked out that CP violation occurred in about one decay in a thousand. If one could transfer this result to the field of baryons an easy explanation would be found for the required one occurrence in a billion decays necessary for baryons inevitably to be generated in the early universe [1, 3, 4].

The Prospect for AMS Both described approaches are speculative and a definite answer to the question of antimatter's fate could only be given by a direct detection of, for instance, antihelium or anticarbon nuclei. The detection of $\bar{H}e$ nuclei would give a hint on the existence of primordial antimatter, whereas detected antimatter particles with $Z > 2$ would give evidence for "anti-stars" or even galaxies made of antimatter [9]. Whereas no detection of antimatter in the 3 years operation time of AMS on the ISS would still, by 3 to 4 orders of magnitude, push the boundaries of our matter domain farther out into space and favour more the nonexistence of antimatter. Both outcomes of these measurements with the AMS detector will result in more detailed insights into our understanding of the universe and its birth during the Big Bang.

2.1.2 Search for Dark Matter

Critical Density It was again E. Hubble in 1926 who found some of the first evidence for dark matter in observations of galactic densities. Calculations based on these observations stated that the mass contained in the visible parts of the galaxies amounts to only $\sim 1\%$ of the "critical density" of the universe. This specific density parameter divides the geometry of the universe into recollapsing, referred to as "closed", or forever expanding, "open".

⁵baryonic no. means the ratio in number of baryons to photons in the CMBR

⁶baryon no. relates to the expression from partical physics

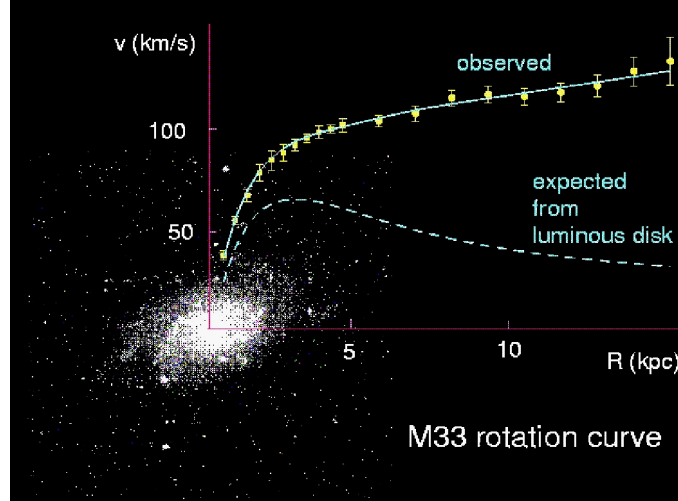


Figure 2.4: *Rotational velocity distribution from M33 galaxy.*

The particular case of a universe whose expansion will continue to slow down, but come to a halt only at infinite time, is called "flat" and its density is called "critical". All astronomical density values are referred relative to this specific density ($\sim 10 p^+/m^3$), using the so called density parameter Ω , where $\Omega = 1$ denotes a flat universe. The data on the CMBR obtained by the experiments COBE and recently WMAP [17] together with the theory of inflation now predict that our universe has such an almost "flat" geometry, which stands in direct contradiction to Hubble's observation of visible mass. The conclusion to this dilemma was the postulation of invisible or dark matter, that almost solely accounts for the critical density of the universe.

Galactic Rotational Velocities A second hint on large amounts of invisible mass relates to the studies of rotational velocities in galaxies. Observations of the visible part⁷ of galaxies lead to the assumption that the major fractions of their masses are gathered in their centers. Assuming this to be true, one would expect a dependence of the rotational velocity v_{rot} on the radius r from the galactic center as $v_{rot} \sim r^{-1/2}$. This is supposed to hold for all radii exceeding a certain radius r_{max} , where v_{rot} has its maximum. The observed v_{rot} distributions from numerous galaxies, as figure 2.4 exemplary shows, indicate a different behaviour, with respect to r . The rotational velocities are constant up to large distances from the galactic nucleus. The way out of this dilemma is again the existence of nonluminous matter contained in the galactic halos that account for more than 90 % of the galactic mass.

The Nature of Dark Matter Still the nature of this dark matter gives only rise to speculations. It is a known fact that even the ordinary, baryonic type matter that we all exist of, comprises no more than 10 percent of the dark matter in the universe. But what type is the predominant fraction of the invisible mass in the universe? Recent discoveries give rise to the assumption that a prevalent percentage, $\Omega_\Lambda \simeq 0.73$ [17], of the universe' density is in the form of so called dark energy, often associated with Einstein's "Cosmological Constant" Λ . This dark energy is simply the energy density contained in the vacuum itself, the zero-point energy of the quantum field, and thus a direct consequence of quantum theory. The further dark matter contributions are, in the order of importance, the nonbaryonic type with a share of $\Omega_{NB} \simeq 0.22$ and the baryonic, $\Omega_B \simeq 0.044$ [17].

⁷this can be extended down to infrared and up to radio- and γ -ray frequencies.

Likely, dark matter relics of the early universe are stable, weakly interacting massive particles, so called WIMPs. One already well known group of candidates are the neutrinos and their possible antiparticles, if only they possess even just a small amount of mass. Due to their huge number, some 100 per cubic-centimeter in each of the three species and "anti"-species, neutrinos could carry an important share of unseen mass. Large underground detectors like the experiments "Super-Kamiokande" [18] and SNO [19] are trying to find evidence for neutrino oscillations and consequently for the mass of the neutrinos. An upper mass limit for the considered lightest of the neutrinos, the electron neutrino ν_e , is $\sim 3 \text{ eV}$ [16], derived from measurements of the Tritium β -decay. To account for all the non-baryonic matter an average neutrino mass of $\sim 50 \text{ eV}$ would be necessary. Besides that, neutrinos move with almost the speed of light and therefore structure formation due neutrinos would be far too slow to explain the observed structures in the universe.

Supersymmetric Contribution One of the most compelling theories for WIMP dark matter is the Supersymmetry (SUSY) [16]. Supersymmetry is an elegant extension for the standard model of particle physics. SUSY as part of a GUT appears to be an attractive route to unify all four forces, as already mentioned earlier in this text. The conservation of R-parity, a SUSY theory-invoked quantum number, prevents SUSY particles from decaying into the lighter SM particles. This predicts the existence of a lightest supersymmetric particle (LSP), which, if electrically neutral, has very weak interactions (like neutrinos).

LSPs are thought to build halos around galaxies and consequently serve as an excellent candidate for dark matter. As a matter of fact, such LSPs would effectively contribute to the formation of galactic gravitational potentials, and could account for a remarkable contribution, $\Omega_{LSP} \simeq 0.1$, to the density of the universe [5, 6]. In supersymmetric theories, the most likely dark matter candidate is a quantum mechanical superposition, called the Neutralino $\tilde{\chi}^0$, of electrically neutral, supersymmetric fermions:

$$\tilde{\chi} = N_1 \tilde{\gamma} + N_2 \tilde{Z}^0 + N_3 \tilde{H}_1^0 + N_4 \tilde{H}_2^0 \quad \text{with} \quad \sum_{i=1}^4 |N_i|^2 = 1$$

where $\tilde{\gamma}$ is the photino, \tilde{Z}^0 is the zino and \tilde{H}_1^0 and \tilde{H}_2^0 are the super-partners of the two different neutral scalar Higgs particles needed in supersymmetric theories. The coefficients N_i are chosen such that the squared sum is normalised to 1. Finding evidence for such Neutralinos would, at a stroke, provide profound new insights into two of the recently most discussed subjects of modern astro- and particle physics. It would be the first evidence for SUSY ever found and spot another component of non-baryonic dark matter.

Evidence for Neutralinos Due to the fact that Neutralinos are believed to be uncharged particles, they cannot be directly detected as primary particles. Detectable indicators for Neutralinos could be their annihilation or decay products as an admixture to the cosmic radiation. Such annihilation processes may generate ordinary matter like protons, electrons and neutrinos, individually or together with their antiparticles, as well as high energetic photons. Unfortunately, there are various other sources of such particles in the universe, leading to large backgrounds for all components of the cosmic radiation. A comparison of cosmic ray fluxes results in choosing antiprotons and positrons as best candidates. Still high precision particle identification and energy resolution in combination with high statistics will be necessary, on the one hand.

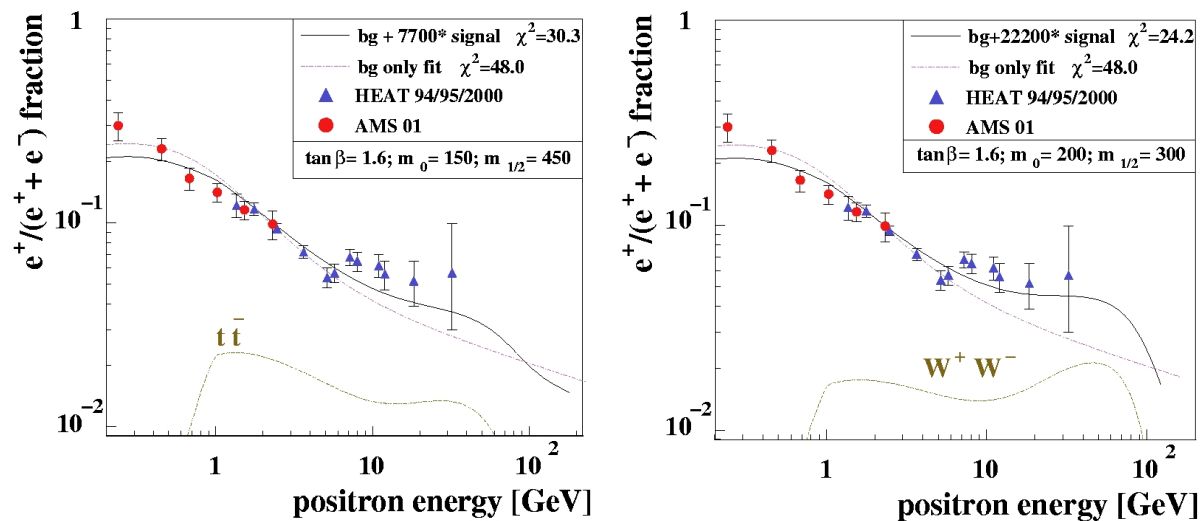


Figure 2.5: *Two SUSY fit results to the HEAT and AMS01 data [5, 6].*

On the other hand, the predicted energy spectra need to be precisely known, in order to notice any possible excess, when compared with the measured data spectra. This includes the knowledge of the composition and structure of the interstellar medium and the galactic halo as well as the particle propagation through space. With respect to this, AMS will collect a total of half a million antiprotons and an accurate spectrum of high energetic positrons over the full period of three years on the ISS.

AMS' Contribution to the Dark Matter Search: In general an electromagnetic calorimeter (Ecal) is playing an important role for positron spectroscopy. It is used to distinguish between protons and positrons or electrons and antiprotons, where in both cases the first named contributes to the background of the latter at high particle energies. In general an Ecal can provide a rejection power of $10^3 - 10^4$ for protons against positrons up to particle energies of ~ 500 GeV [20]. For a further reduction of particle misidentification, additional separation power can be provided by a Transition Radiation Detector (TRD). The TRD used in the AMS experiment will supply another factor of better than 10^2 up to 250 GeV proton energy, as will be shown later on.

But what can be learned from such a precisely measured positron spectrum? What would a Neutralino signal look like? The first hint on such a Neutralino signal was found by the HEAT Experiment. The accumulated positron spectra taken during their 1995 and 1996 measurement campaigns, and confirmed during a third campaign in 2000, are showing a positron excess in the energy range above 5 GeV. These extra positrons may have been generated in Neutralino annihilations in the galactic halo of our Milky Way. Detailed studies with different sets of SUSY parameters have led to best fits to the HEAT, combined with the AMS01, data samples. Exemplary, two such fits are shown in figure 2.5 [5]. These calculations have been processed using the assumption that the background predictions are correct, knowing though that particle propagation through the galaxy and the structure of the galactic halo are not well understood so far. The second necessary adoption lies in the believed "clumping" of Neutralinos similar to ordinary matter, inside our own solar system or galaxy. To quantify this possible increase in the Neutralino density a so called "boost" factor is used as one of the fit parameters.

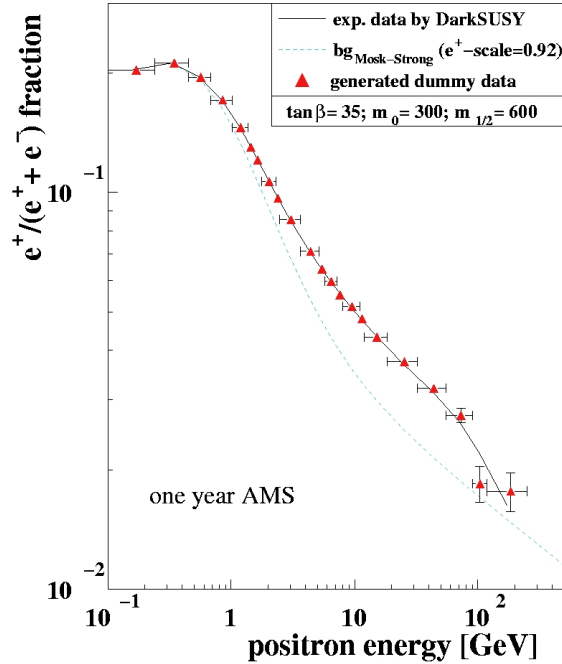


Figure 2.6: Positron fraction as expected after one year of AMS on the ISS, assuming a Neutralino of 240 GeV mass and a boost factor $\sim 10^4$ [5].

Boost Factor This boost factor is the multiplication factor, which the number of $\chi\bar{\chi}$ annihilations, occurring in a smooth halo, has to be enhanced by, to match the measured data. By such clumping boosts of greater than 10^4 can be explained, which is in the range of the maximum value resulting from those fits. This can be understood by the simple example of our own galaxy. The Milky Way Galaxy contains an average of $\sim 10^5 p^+/m^3$, and a similar number density is assumed for the Neutralinos. The comparison to the mean number density in our solar system leads to a "proton density boost" of $\sim 10^2$ and thus a simple explanation for the necessary Neutralino annihilation boost factor⁸.

Despite those conjectures, it turned out to be difficult to describe the measured data with a background only hypothesis. As the plots show, a contribution from Neutralino annihilation can improve the fits considerably, by roughly a factor of 2 in the fit's χ^2 . Unfortunately though, the statistical errors on the existing data samples are still too big for a statement on the existence and mass of any LSP to be conclusive. Still it is indecisive whether this surplus seen in the measured positron spectra is a hint on new physics or just due to an underestimated or badly known background. This is mainly because the HEAT data were taken within only a few days. But on this sector surely with AMS, and maybe even prior to that with the PAMELA experiment, major improvements are put on their way. For instance, after one year of AMS on the ISS the same spectrum as before would look as figure 2.6 shows, assuming annihilations of 250 GeV Neutralinos to occur with boost factors $\sim 10^4$, based on an Ecal inclusive AMS' acceptance of $0.04 m^2 sr$ [5].

In addition AMS will take measurements of high energetic gamma rays in two ways. A direct measurement making use of the electromagnetic calorimeter as well as by detecting the e^+e^- -pairs that are produced by conversion of the γ inside the detector. These gamma rays may serve as a hint on anti- as well as dark matter depending on their energies.

⁸Remark: The boost factor used for the fit is calculated as the square of the density boost factor.

2.1.3 Further Research Goals

AMS will also study other issues in astrophysics with high statistics measurements. This high sensitivity and the large acceptance of AMS will enhance the capability of searching for new and unimagined astrophysics phenomena. But even less speculative, one can gain deeper insights into the understanding of the universe shortly after the Big Bang and the primordial formation of the lightest elements. For that reason AMS will detailedly study the isotopes' proportions in cosmic rays of these lightest elements such as D/p , ${}^3\text{He}/{}^4\text{He}$ or ${}^{10}\text{Be}/{}^9\text{Be}$. In this concern, the Beryllium case is of special importance due to the long half-life, about one million years, of the radioactive ${}^{10}\text{Be}$ isotope. A high ratio would mean that most of the cosmic rays are, in astronomical terms, relatively young - less than a million years. Otherwise the cosmic rays would have been traveling much longer, giving the ${}^{10}\text{Be}$ nuclei time to decay [21].

2.2 The AMS Detector

The AMS project is being realized in two phases. In June 1998, a baseline configuration of the experiment, referred to as AMS-01, has completed a very successful precursor flight on board the Spaceshuttle "Discovery". During this mission (STS-91) the AMS collaboration gathered important information on the detector performance in actual space conditions. On top of this AMS-01 has measured cosmic ray fluxes in the GeV region, for the first time, covering Earth's surface between 52° northern and southern latitude. By doing so, AMS was able to improve the current limits on the search for antimatter by more than one order of magnitude. For further information on the detector layout, performance and the physics results, one may refer to [11]. The following section will, in brief, present the AMS-02 design foreseen for its operation on the International Space Station.

AMS-02 Design The AMS Experiment will use state of the art technologies from modern high energy particle physics. The great challenging aspects of this project are the very strict limitations that any space application has to adhere. For instance, the total weight of the whole detector has to be kept below 7 tons as well as the total allowed electrical power consumption must not exceed a value as little as 2.1 kW. To keep this given weight limit, the whole detector is covered by only a minimal mechanical shielding against meteorite impact, for instance. Despite those weight limits, the full detector still has to sustain the accelerations during the Shuttle launch and landing. Figure 2.7 shows the experimental configuration of AMS-02.

Engineering Challenges The great engineering challenge about this project is to get well known detector components to a stable operation in such inhospitable or harsh conditions as outside Earth, in space. For mechanical stability, needed to "survive" the Shuttle launch, the entire detector will be surrounded by a support framework. All subdetectors and subsidiary systems, like power and gas supplies, will be mounted to this "Unique Support Structure" (USS). With the aid of this USS the AMS detector will be integrated into the Cargo Bay of the Shuttle as well as attached to the ISS.

Among the great challenges two of the most important ones can be named as the almost perfect vacuum and the extreme and drastically changing temperatures on board the ISS. Regarding this for instance, the temperature of AMS' outer casing will range from 92 K to 322 K (-180°C to $+50^\circ\text{C}$) during ISS' 90 minute orbits around Earth. Compared to this the operating conditions of AMS' superconducting magnet will be 1.8 K at 20 mbar.

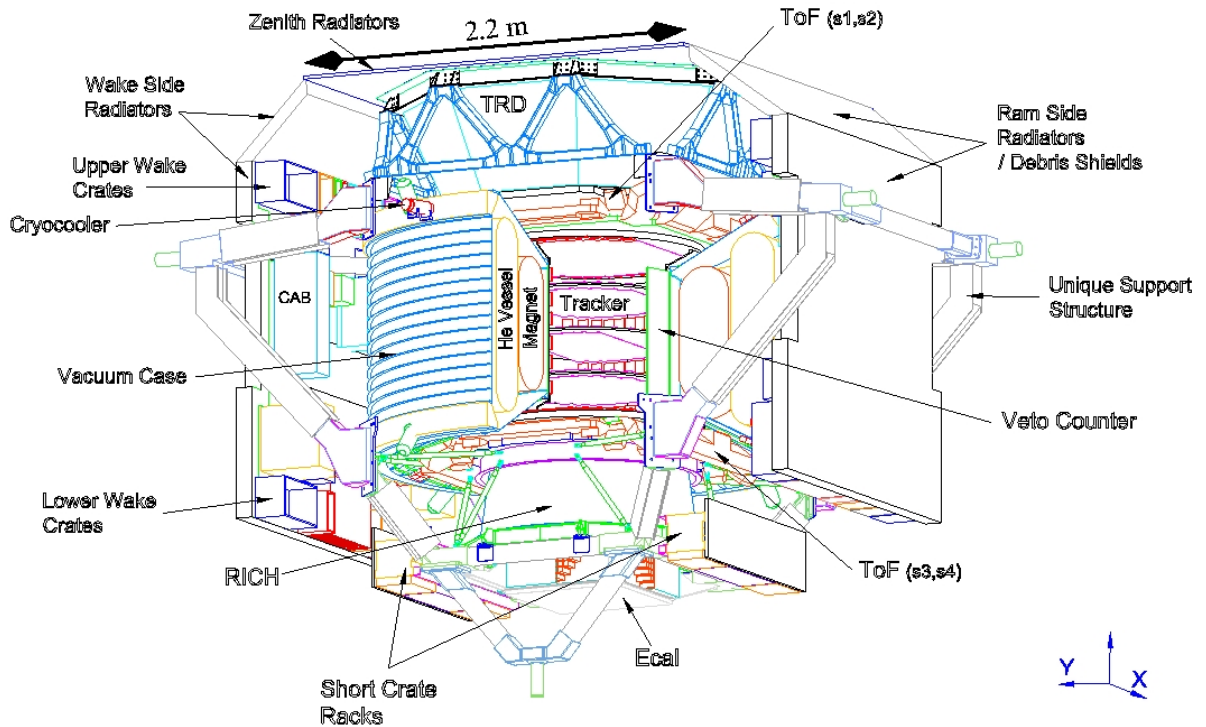


Figure 2.7: AMS-02 configuration on the ISS [22].

In that same sense, it is necessary for every gasfilled detector, like the proportional chambers of the AMS TRD, to have a stable environment, concerning temperature and pressure, since the gas amplification is strongly dependent on the gas density. To guarantee such a stable operation the temperature gradient, ΔT , inside the TRD of the AMS experiment has to be kept within a limit of $1K$. Whilst the overall temperature T inside the detector can vary during operation from about $270 K$ to $300 K$, depending on the angle of the ISS orbit towards the sun. For that to be possible, the TRD will be individually wrapped in a set of multi layer insulation (MLI) foils.

A second challenge refers to the vacuum and it again especially concerns the TRD with its gasfilled proportional chambers. Due to the limits in mass for the whole detector, the gas supply is restricted to $50 kg$. Therefore it is necessary to build gasdetectors which have a minimum net weight but still are gas tight down to the diffusion level to get by on the limited gas supply. In addition to this, NASA asks for the strict adherence to their requirements on space qualification. According to this, only NASA approved materials can be used and special concern lies on the outgasing rates of materials. Additionally, vibration and thermo-vacuum tests have to be carried out for all components of the AMS detector. Further information on the work involved in this subject can be found in [23].

AMS Schedule However, all those and further challenges are finally matched and the AMS project has reached the building stage for each subdetector. The schedule foresees the completion of this stage by the end of 2003. The AMS assembly will start latest in summer 2004 in order for AMS to be accomplished in November, one year before the lift-off. Right after the finished assembly, the detector will be handed over to NASA, where it has to undergo several final tests. In the months before the start a team of AMS collaborators will do the final preparation and integration steps.

Six to eight weeks before the launch this work has to be finished, in order for the detector to be mounted into the cargo bay of the Shuttle, this latter to be moved to the launch pad and from there to be lifted to the ISS.

2.2.1 Silicon Tracker and Alignment

In combination with the magnet, the silicon tracker represents the centerpiece of the AMS detector. This silicon tracker consists of 8 planes of double sided silicon microstrip detectors. The spatial resolution will be better than $10\ \mu\text{m}$ in the magnet's bending plane and $30\ \mu\text{m}$ perpendicular to that. The planes are placed inside the magnet, with the six innermost combined to build pairs. The two outermost layers serve as the entrance and outlet windows. All 8 tracker planes together comprise 192 silicon ladders corresponding to an active area of about $6\ \text{m}^2$ of silicon and ~ 200.000 readout channels. Still the entire tracker electronics only consume 800 W of power. For protons the momentum resolution dp/p is expected to be $\sim 3\%$ at 100 GeV, as figure 2.8 illustrates, compared to $\sim 20\%$ for AMS-01 [24, 25].

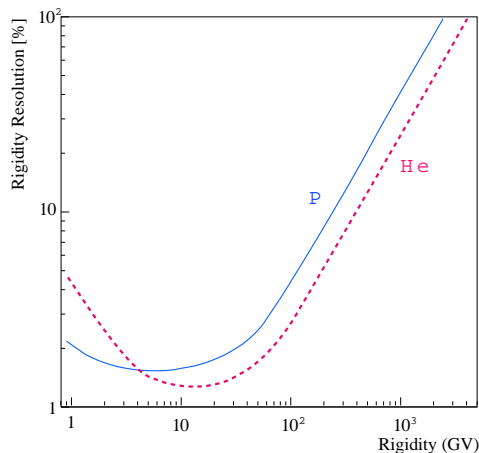


Figure 2.8: *Momentum resolution of the Silicon-Tracker [24].*

In addition, the tracker is equipped with an IR laser alignment system, which is built at Aachen I. It will continuously monitor the X- and Y-position of the tracker layers with respect to each other. The principle of this system is to pass a laser beam of infrared (IR) wavelengths, through selected spot areas - the so called "Alignment Holes" - in each detector plane. Benefiting from the partial transmittance of crystalline silicon at IR wavelengths, a signal in all 8 tracker planes can be generated from only one beam. For redundancy, the full alignment system will consist of 5 pairs of beams, placed in the center of the tracker [26].

2.2.2 Superconducting Magnet

The superconducting magnet consists of 2 dipole and 12 racetrack coils made of aluminium stabilized $NbTi$ wire, through which a current of 460 A is run. This magnet will be the largest superconducting magnet up to now used in space. Its operating conditions are 1.8 K at 20 mbar, which requires superfluid helium for cooling. To ensure at least 27 months operating time, 4 cryocoolers are employed to keep the vessel, containing the magnet's liquid Helium tankage of 2600 liters, at low temperatures. With this configuration a cen-

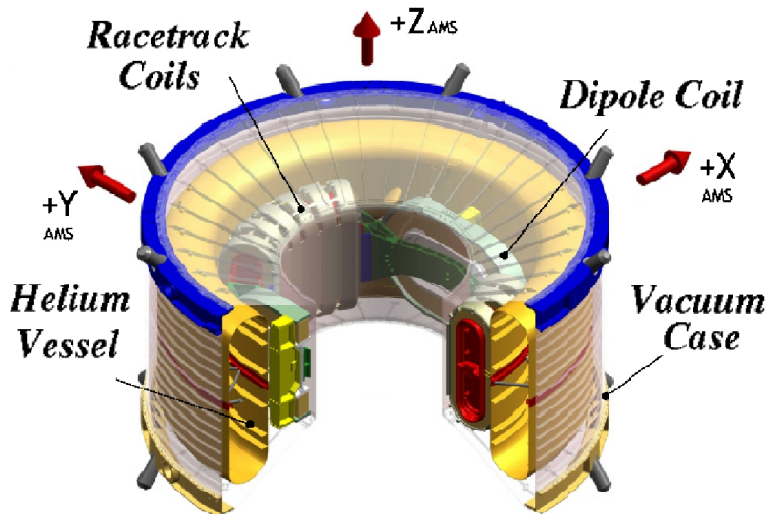


Figure 2.9: *The superconducting magnet [27].*

tral magnetic field of 0.87 T , in the indicated positive X-direction (see fig. 2.9) - leading to a central bending power⁹ (BL^2) of 0.78 Tm^2 - can be achieved. This denotes an increase in the magnetic field strength by a factor of 6 compared to that of the permanent magnet of AMS-01. This will extend the maximum detectable rigidity limit up to $\sim 3\text{ TV}$. The field configuration is designed such that the stray field at a radius of 230 cm (at the outer skin of the helium vessel) is less than 15.2 mT . The weight of the whole magnetic system is budgeted to 3 tons at a height of 860 mm and an inner diameter of 1056 mm [27].

2.2.3 Anti-Coincidence Counter (ACC)

A layer of plastic scintillators, divided into 16 modules, is covering the inner wall of the magnet, surrounding the tracker planes. These scintillators, as displayed in figure 2.10, are used to veto stray trajectories and secondary particles, produced in interactions of the primary particle with the detector planes. In addition it will detect backscattering off the Ecal and particles incident through the sidewalls of the magnet. They are read out by photomultipliers (PMs), which will be mounted onto the outer collar of the magnet to avoid the high magnetic stray field. Wavelength shifting lightguide fibres, as additionally shown in the figure, serve as connectors between the scintillators and the PMs. The ACC subsystems for AMS02 is the responsibility of Aachen I [28].

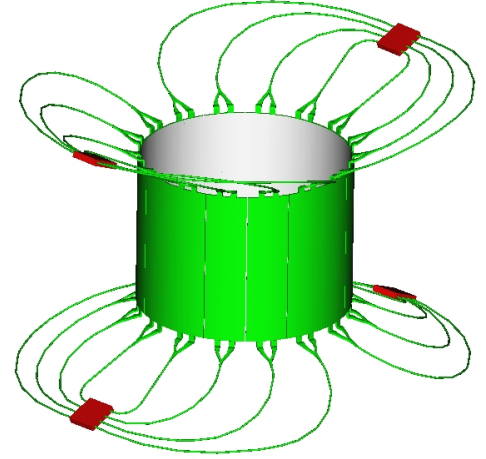


Figure 2.10: *Anti-counter system* [22].

2.2.4 Time of Flight System (ToF)

The ToF subsystem provides a fast trigger for the experiment with a time resolution of $\sim 120\text{ ps}$. This subsystem is divided into two parts of two scintillator planes, each. One pair is mounted directly on top of the magnet and the other is attached to the lower end. The upper ToF is attached to the so called M-support structure of the TRD, as will be explained in more detail later on. Each of the layers, as illustrated in figure 2.11, consists of 11 cm wide and 1 cm thick scintillator panels. The light produced in the panels is collected via light guides and read out by photomultipliers¹⁰, two at each end of each panel. Making use of the high time resolution, the ToF system is able to measure the velocity and the direction of the particles that pass through the detector. Via the measurement of the energy loss of the traversing particle the relative particle charge (Ze/e) can be determined in the same way as inside each of the tracker planes and TRD detector layers [29].

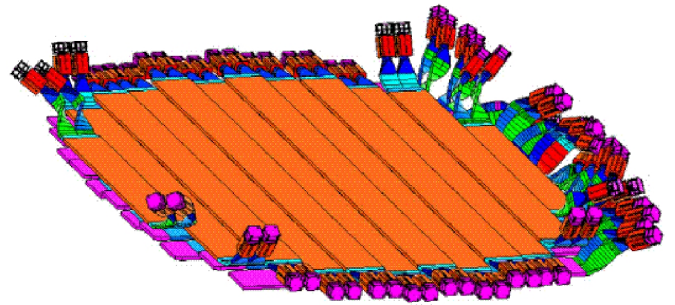


Figure 2.11: *Time of flight system* [22].

⁹where B = magnetic field, L = path-length of the particle inside the central magnetic field

¹⁰The various orientations of the PMs are chosen for best performance in the magnetic stray field.

2.2.5 Ring Imaging Čerenkov Counter (RICH)

As a substitution, the RICH replaces the Aerogel Čerenkov Counter from AMS-01. It is using the "proximity focusing" technique. This type of counter, as displayed in figure 2.12, consists of a radiator plane, in which the Čerenkov light is produced. A drift space of 414 mm , in which the Čerenkov rings can expand, separates the radiator from the detector plane. This radiator plane is made of an Aerogel material with a refractive index $n=1.05$ and a thickness of 30 mm . The detector plane consists of 680 sensors, where each of them consists of a lightguide cone segmented into 16 parts and a PM with pixels, reading out the lightguide segments individually. The central area of this lower plane is left open as a "window" to the Ecal. The total weight of this subsystem is 184 kg and it will consume 110 W of electrical power. The main aim for this subdetector is to separate isotopes up to an atomic number $Z \simeq 26$ and the measurement of the particle velocity. This will be possible above a threshold of $\beta > 0.95$ with an accuracy of $\Delta\beta/\beta \leq 0.1\%$. At low energies, below a threshold of about 4 GeV , it can provide extra e^+/p^+ separation power [30].

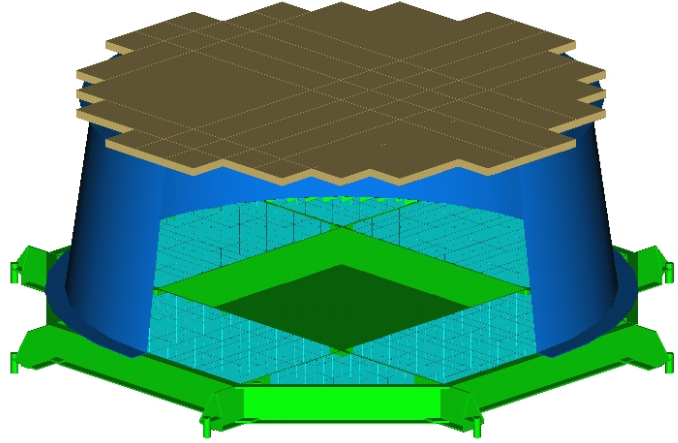


Figure 2.12: Ring imaging Čerenkov counter.

2.2.6 Electromagnetic Calorimeter (Ecal)

The Ecal is one of the two devices, together with the TRD, to distinguish between light and heavy particles. This electromagnetic calorimeter is a 3 dimensional sampling calorimeter of the SpaCal¹¹ type. It consists of 9 "superlayers" made out of lead and scintillation fibres. Each of these Superlayers includes 10 planes of a combined lead converter and scintillator layer. The Superlayers are alternately oriented in x- and y-direction, perpendicular to each other. The full height of this subdetector, as figure 2.13 illustrates, will be 166 mm with an overall radiation length of $\sim 16.5 X_0$ and a weight of 512 kg . Single-sided, the fibres will be read out by a total of 324 PMs, each segmented into 16 pixels, evenly distributed on the four lateral sides of the calorimeter. Due to the limited size (a direct consequence of the weight limit), the Ecal restricts the overall AMS acceptance by roughly a factor 10, down to $0.05\text{ m}^2\text{sr}$.

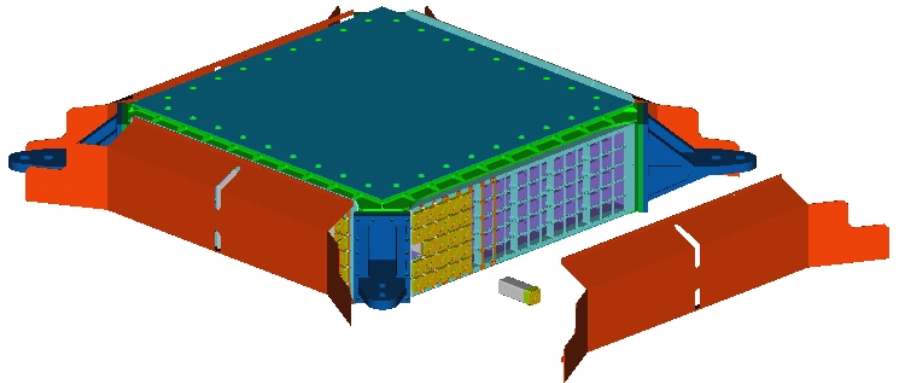


Figure 2.13: The electromagnetic calorimeter [22].

¹¹Spaghetti Calorimeter

For the AMS Experiment it is of special importance to be able to identify high energetic particles of the same electric charge, such as e^+ and p^+ or \bar{p} and e^- . In such cases, where the particle energies are very high, the tracker cannot distinguish between those named leptons and hadrons anymore, but still the electromagnetic shower form inside the Ecal will be different. This shower form is measured with a granularity of ~ 0.5 Molière radii in both X- and Y-direction and $\sim 0.9 X_0$ in Z. With such a setup the Ecal can provide a separation power of $10^3 - 10^4$ up to energies of 500 GeV. Besides the separation power, the Ecal will measure the full energy of electrons and positrons and detect high energetic γ rays [20].

2.2.7 Transition Radiation Detector (TRD)

Straw tube proportional chambers arranged in 20 layers, covered with radiator material, are designed to provide "non-destructive" particle identification additionally to the Ecal. The straw tubes which have 6 mm diameter and a length of up to 2.2 m will be combined to modules of 16 straws each. The full detector, as displayed in figure 2.14, will consist of 328 such modules filled with a Xe/CO_2 (80/20) gas mixture. In between the detector layers a 22 mm layer of radiator material is placed, inside which the transition radiation is generated. The radiator is composed of a polypropylene fiber material with a fiber diameter of $10 \mu m$ and an overall density of $0.06 g/cm^3$. The full height of this subsystem will amount to 60 cm with a weight of 475 kg including the mechanical support for the TRD and the upper ToF. The capability for e^+/p^+ separation will be better than 10^2 referring to an electron efficiency of 90% up to particle energies of 250 GeV.

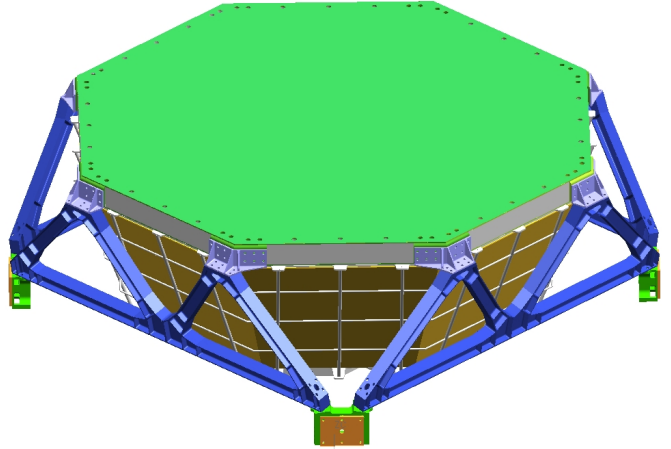


Figure 2.14: *The transition radiation detector with the M-support structure [22].*

As a second function, this subdetector will be used to gain track information of the traversing particle outside the central magnetic field. Additionally to this, the ionisation energy loss dE will be measured in each of the layers. Together with the mean path length of the traversing particle inside the detector tubes, this measurement can be used to gain information on the particle's velocity and charge, additionally to the RICH and the Tracker.

Since this TRD is subject of this work a full and detailed description of this subsystem can be found in the following chapter as well as the detailed review of the physics of transition radiation and its absorption in the proportional gas.

Chapter 3

The AMS Transition Radiation Detector

The effect of Transition Radiation (TR) has a history of more than 50 years and is used in many recent particle detector projects, such as Hera-B or ATLAS. It has become very important in modern particle physics, because it can provide "non-destructive" particle identification even for highly relativistic particles. Other methods are primarily measuring the particle's velocity, making for instance use of the Čerenkov effect. These techniques imply technical feasibility limits, especially when large solid angles have to be covered. This is because it requires long distances that a high energetic particle can travel through and thus huge detector volumes. On the other hand, the effect of Transition Radiation depends on the Lorentz factor $\gamma = \frac{E}{mc^2}$ of the particle, which provides the possibility to identify particles up to very high energies, as long as only their masses differ significantly, using a detector of reasonable size [31].

Electromagnetic radiation is emitted by a charged particle moving in a medium, attributed to two mechanisms. If the particle is decelerated in the electromagnetic field of an atomic nucleus, radiation known as bremsstrahlung is emitted. A change in the refractive index of the medium results in a different phase velocity of the particle's wavefunction. To fulfill the continuity conditions at the boundary of the two media, the so called transition radiation is emitted. For ultra-relativistic particles the TR spectrum extends into the x-ray region, which makes this phenomenon become useful for particle detectors. The number of photons radiated per transition is of the order of the fine structure constant α , which requires ~ 100 media transitions necessary to gain a detectable radiation yield of at least one x-ray photon per detector layer.

A summary of the transition radiation theory, based on references [31, 32, 33], can be found in the next section. The second section of this chapter deals with the description of the physics of x-ray photon absorption and, because this contribution can not be avoided, the energy loss of charged particles inside the proportional gas. This chapter will conclude with a full description of the AMS TRD subsystem.

3.1 Transition Radiation

The effect of transition radiation (TR) is occurring as the result of a charged particle traversing the boundary between two media of different dielectrical constants $\epsilon_1 \neq \epsilon_2$. An elegant way to understand this is to imagine a charged particle in front of a perfectly conducting metal surface, as displayed in figure 3.1.

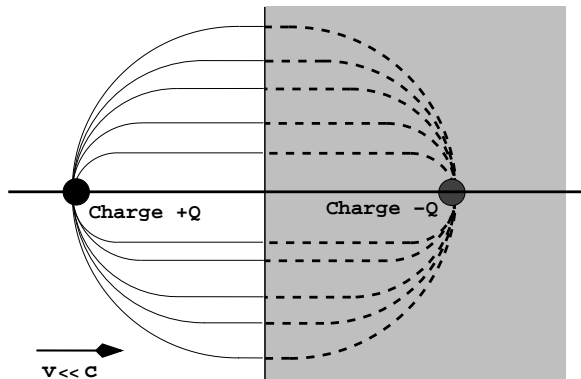


Figure 3.1: *Electric charge in front of a perfectly conducting surface forms an electric dipole. Continuous and dashed lines represent the electric field lines.*

From basic electrodynamics it is known that the charge's electromagnetic (elm.) field lines are perpendicular to the surface and the charge electrostatically induces a surface charge as if a mirror charge were present. An electric dipole is formed. If the particle now moves non-relativistically towards the surface, as indicated in figure 3.1, the dipole changes until it disappears when the particle enters the boundary. To fulfill the boundary conditions on the surface, an electric field (transition radiation) is emitted.

Using the highrelativistic limit, which is perfectly applicable for AMS' conditions, the radiation is boosted into the particle's forward direction. Its radiation cone opens with only a small angle¹ and the TR spectrum peaks in the x-ray region, at $E_{ph.} \sim 6 \text{ keV}$.

At such high equivalent photon frequencies² the medium can be considered as an electron gas with an electron density n_e and a plasma frequency $\omega_P = \sqrt{4\pi\alpha n_e/m_e}$, where m_e is the electron mass and α denotes the elm. fine structure constant. The medium's dielectric constant $\epsilon(\omega)$ is then given by

$$\epsilon(\omega) = 1 - \frac{\omega_P^2}{\omega^2} = 1 - \xi^2 \quad \text{for } \omega \gg \omega_P \quad (3.1)$$

Substituting this into the solution of the homogeneous Maxwell equation, such as transition radiation analytically is, together with the approximation of high γ and small angles θ , results in the intensity dW of the radiation emerging from an element of surface $d\Omega$:

$$\frac{\partial^2 W}{\partial \omega \partial \Omega} = \frac{\alpha}{\pi^2} \cdot \left| \left(\frac{\theta}{\gamma^{-2} + \xi_1^2 + \theta^2} \right) - \left(\frac{\theta}{\gamma^{-2} + \xi_2^2 + \theta^2} \right) \right|^2 \quad (3.2)$$

The intensity distribution has a sharp maximum at $\theta_{max} \approx \frac{1}{\gamma}$ and its twofold integration with respect to the solid angle Ω and the photon energy $\hbar\omega$, results in the total intensity W emitted from one boundary, with ω_{P_1, P_2} being the plasma frequencies of the two media.

$$W = \frac{\alpha}{3} \cdot \hbar \cdot \frac{(\omega_{P_1} - \omega_{P_2})^2}{\omega_{P_1} + \omega_{P_2}} \cdot \gamma \quad (3.3)$$

¹ $\theta_{max} \approx \frac{1}{\gamma}$
² $\nu = E_{ph.}/h$

$$\phi_m = \frac{\omega l_m}{v} - \vec{k}_m \vec{l}_m \quad (3.7)$$

Here \vec{k}_m denotes the wave vector of the photon radiated from the first boundary, \vec{l}_m is the layer thickness of the medium and v the particle's velocity. For small ϕ_m the two photons will interfere destructively. Therefore a minimal medium thickness is required, which should be of the order of the so called formation length

$$z_m = \frac{2 \cdot c}{\omega} \cdot \frac{1}{\gamma^{-2} + \theta^2 + \xi_m^2} \quad (3.8)$$

and with that ϕ_m can be expressed as

$$\phi_m = \frac{\omega l_m}{2 \cdot c} \cdot (\gamma^{-2} + \theta^2 + \xi_m^2) \quad (3.9)$$

Metaphorically speaking, the formation length can be regarded as the distance along the particle's trajectory in a given medium, after which the spatial separation between the primary particle and the emitted photon is of the order of the photon wavelength. Separated by such a distance, the elm. fields of the particle and the photon cannot effectively interact anymore.

3.1.2 The Radiation Yield

In the case of only one foil, placed in a gas, there are two boundaries with $\vec{e}^1 = -\vec{e}^2$. At first neglecting absorption and realizing that $\xi_1 = \xi_3$, the differential yield can be calculated from 3.2 and 3.5 as follows:

$$\left(\frac{\partial^2 W}{\partial \omega \cdot \partial \Omega} \right)_{single\ foil} = \left(\frac{\partial^2 W}{\partial \omega \cdot \partial \Omega} \right)_{single\ surface} \cdot 4 \sin^2(\phi_1/2). \quad (3.10)$$

The foil thickness l can be optimized such that the intensity is amplified, due to constructive interference, by up to a factor of 4, compared to the single surface. This is the case whenever the phase factor ϕ is an odd multiple of π . For most applications the assumption $\gamma \cdot \xi \gg 1$ holds and the maxima ω_{max} of the energy spectrum, as shown in figure 3.3b, can be determined as a function of the foil thickness l and the plasma frequency ω_P , only. Using $\theta \approx 1/\gamma$ in equation 3.9 together with the constructive interference condition, results in:

$$\hbar \omega_{max} = \frac{l \cdot \hbar \omega_P^2}{4\pi \cdot c \cdot (n + \frac{1}{2})}; \quad n = 0, 1, 2 \dots \quad (3.11)$$

The appropriate optimal foil thickness can be derived from angular integration of equation 3.10 as

$$l_f = 2\pi \cdot c \cdot \frac{\omega}{\omega_{P_1}^2 - \omega_{P_2}^2} \quad (3.12)$$

A consequence of the formation length is that in case of a fixed foil thickness the transition radiation yield comes to a saturation at $\gamma \geq \omega/\omega_{P_1}$. That is because the formation length exceeds the thickness of the foil, and if so, the high energetic part of the spectrum becomes suppressed. Figure 3.3a displays this yield as the average number of generated TR photons

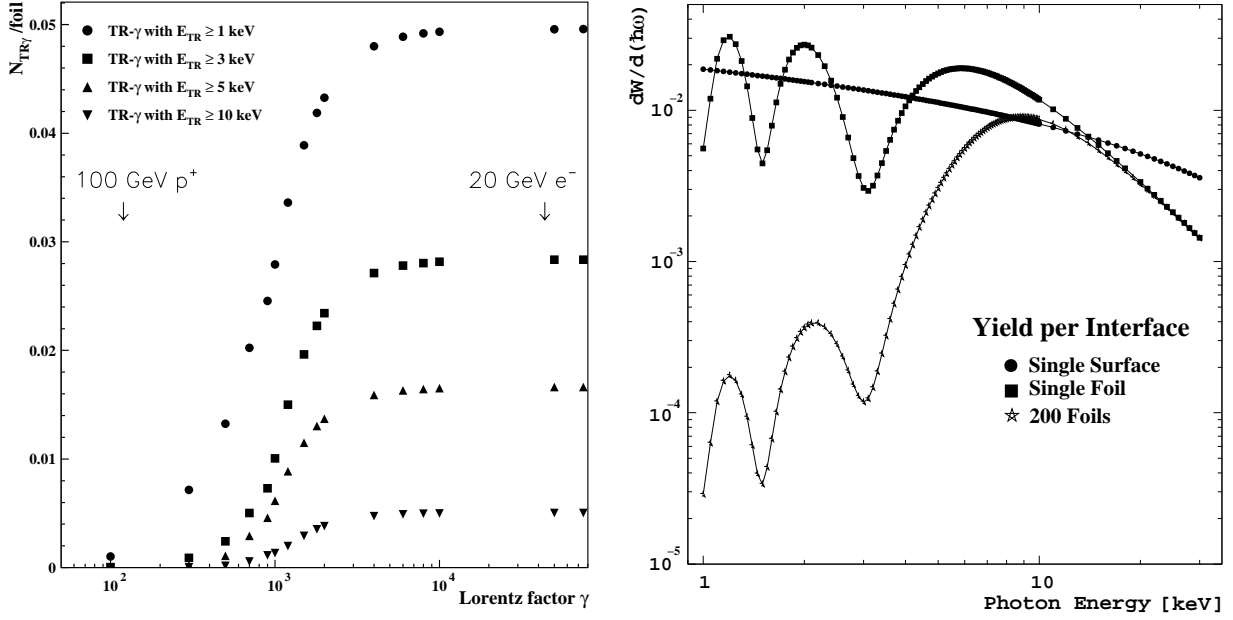


Figure 3.3: a) The increasing probability to generate a TR photon, from a single foil, up to the saturation at high γ factors; b) Calculated transition radiation yield normalised to one surface, from one surface, one foil and a stack of 200 foils, with $20 \mu\text{m}$ thickness and a $200 \mu\text{m}$ spacing. Transitions: air \Leftrightarrow Mylar and $\gamma = 8000$ [34].

per foil³, with photon energies E_{TR} above four different energy thresholds. Clearly visible is the substantially increasing TR yield as a function of the Lorentz Factor γ and the saturation at high γ values. It is this substantial rise in the TR yield, for protons above 100 GeV for example, that limits the e^+/p^+ separation power for TRDs.

3.1.3 Radiator

Regular Radiator A stack of foils, as displayed in figure 3.2, is called a regular radiator. It usually contains a large number N of evenly spaced foils. The intensity emitted from such a radiator is very similar to that of a single foil scaled by the "effective" number of foils, N_{eff} . $N_{eff}(\omega)$ denotes the number of foils that effectively contribute to the generation of transition radiation in a certain energy range. The total intensity after N foils is given by:

$$\left(\frac{\partial^2 W}{\partial \omega \cdot \partial \Omega} \right)_{N \text{ foils}} = \left(\frac{\partial^2 W}{\partial \omega \cdot \partial \Omega} \right)_{1 \text{ foil}} \cdot \frac{1 - e^{-N\sigma_m}}{1 - e^{-\sigma_m}} = \left(\frac{\partial^2 W}{\partial \omega \cdot \partial \Omega} \right)_{1 \text{ foil}} \cdot N_{eff}(\omega) \quad (3.13)$$

When N increases so does the absorption, and if $N > 1/\sigma_m$ this results in the saturation of the TR yield. For small photon energies only a limited number out of all foils contribute to the TR yield, regardless the real number of foils. Not until the photon energy increases to $\sim 20 \text{ keV}$ the absorption diminishes and N_{eff} increases up to almost the nominal value N . As a matter of that fact, the low energetic part of the TR spectrum is drastically reduced due to absorption. Figure 3.3b illustrates these facts. The displayed distributions exemplary show the radiation yield from one surface, one foil of $20 \mu\text{m}$ thickness and a radiator made out of $N = 200$ such foils with $200 \mu\text{m}$ spacing. In this example, the foils consist of Mylar⁴ material and the particle's γ factor is set to 8000.

³as used in the GEANT Monte Carlo simulations (see chapter 6 for details)

⁴plasma freq.: $\hbar\omega = 24.7 \text{ eV}$

For comparison reasons the total yield is normalised by the number of surfaces, $2N$. The interference effect is clearly visible for the single foil and the radiator case, as well as the suppression of the low energetic part of the radiator spectrum, as a result of the absorption.

Irregular Radiator In practice, such as for the AMS TRD, very often so called irregular radiators are used. Irregular radiators have varying foil thicknesses and distances between them. These variations follow distribution functions around a mean value. These functions can be very slight deviations from that mean value due to manufacturing imperfections only or highly irregular, as in the case of the radiator used for the AMS project. In all cases the radiation yield is reduced compared to the perfect regular radiator. In a highly irregular case the yield reduction can amount to 10 – 30 %. But part of this drawback is made up for, because in the same way as the yield reduces the TR energy spectrum softens. That decrease in mean photon energy leads to an increase in the absorption probability for the generated TR photons inside the detector [31].

As this summary of the TR effect shows, the right choice of the radiator parameters, such as the foil thickness, the distance between foils and their number can crucially influence the performance of a TRD. The second part of a TRD is the detector layer, in which the photon energy is deposited and transformed into an electrical signal. The underlying physics effects to absorb the TR photons as well as the technical realisation of such a detector will be described in the following section.

3.2 Transition Radiation Detection

Most of the TRDs in use employ gasfilled proportional chambers to detect the transition radiation. In order to do so, the atomic number of the proportional gas has to be chosen such, that the absorption length is small for the traversing x-ray photons. In addition to the energy deposition of TR photons inside the gas, the primary particle always contributes to this, due to its energy loss during interactions with the gas atoms. In order to keep this second contribution as small as possible, but still detect as many TR x-rays as possible, it is best to choose a noble gas with high atomic number Z , like Xe ($Z = 54$), at a low density. This next section will describe the origin of both contributions to the total energy spectrum, detected in a proportional chamber. Due to the fact that the primary particle's ionisation energy loss is present in any detector volume, that it passes through, this energy loss will be dealt with first. Whereas the TR photons only have a probability of about 60 % to be absorbed inside the next detector layer, made of 6 mm proportional tubes filled with Xe/CO_2 gas. This is one of the reason why all TRDs consist of several layers of combined radiator and detector.

3.2.1 dE/dx Energy Loss

The general mechanism of particle detection is based on the particle's interaction with the detector material. In the case of a charged particle the interaction is most commonly electromagnetic, rather than a scattering off the atomic nucleus. The particle's charge interacts with its counterpart of the detector material's shell electron. In each such interaction the traversing particle transfers energy to the shell electrons, which either get promoted to higher atomic or solid state energy levels or for gaseous materials, most likely, leave the atom ionised.

Electron/ion-pairs are produced inside the gas and are separated under the influence of an electric field to gain an electrical signal. Moderately relativistic charged particles lose energy primarily due to such ionisation. The mean rate of energy loss dE within a unit length dx is given by the Bethe-Bloch Equation [36],

$$-\frac{dE}{dx} = \frac{N_A e^4}{8\pi m_e c^2} \cdot \frac{Z \cdot z^2}{A} \cdot \frac{\rho}{\beta^2} \cdot \left[\ln \left(\frac{2m_e c^2 \beta^2 \gamma^2 T_{max}}{I^2} \right) - 2\beta^2 - \delta(\beta) \right] \quad (3.14)$$

where

e, m_e	: charge and mass of an electron;	N_A	: Avogadro's number
Z, A	: atomic and mass number o. t. material;	z	: charge of the ionising particle
β	: the particle's relative velocity ($\frac{v}{c}$);	ρ	: density of the absorber material
I	: mean ionisation potential;	T_{max}	: max. energy transfer / interaction
		$\delta(\beta)$: density correction

Figure 3.4 plots a typical distribution of energy loss as a function of the kinetic energy⁵ in Xe/CO_2 gas, separately for protons and electrons. Typical here is the steep declension ($\sim 1/\beta^2$) of the energy loss below the minimum at $\gamma \approx 3$. This special γ value refers to an electron energy of about 1.5 MeV. Although it is used for a large range of particle energies, the expression "minimum ionising particle (MIP)" is precisely valid solely for the particle energy referring to this Lorentz factor γ . As the energy increases, the electric field of the particle's charge flattens and extends due to relativistic effects. Because of this extended electric field the distant-collision contribution, $\delta(\beta)$ in Eq. 3.4, increases as $\ln(\beta\gamma)$. For even higher energies this effect saturates as a result of the polarisation of the medium. The polarised medium limits the field extension and effectively truncates this part of the logarithmic rise [36].

Occasionally, the energy transfer to one single shell electron can be that high, that it can ionise gas atoms itself, and even run out of the detector volume. Those electrons are referred to as δ -electrons, which are preferably emitted perpendicular to the primary particle's trajectory [35].

A second effect that contributes to the energy loss of a charged particle is the emission of bremsstrahlung. For that to happen the particle is deflected by the electric field of an atomic nucleus and because of the change in the particle's velocity vector a bremsstrahlung photon is radiated. Electrons in the GeV energy range lose most of their energy by bremsstrahlung. These bremsstrahlung photons mainly have energies of a few MeV or higher, and thus a very small probability to be absorbed in a detection gas. This last fact can be understood, in more detail, after reading the following section on photon detection.

3.2.2 Photon Detection

The detection of photons also depends on their interaction with the detector material. Generally speaking, the mechanism is to transfer the photon energy to a charged particle, most likely an electron, and then measure its total energy, via energy loss, inside the proportional gas.

⁵ $E_{kin} = m(\gamma - 1)$

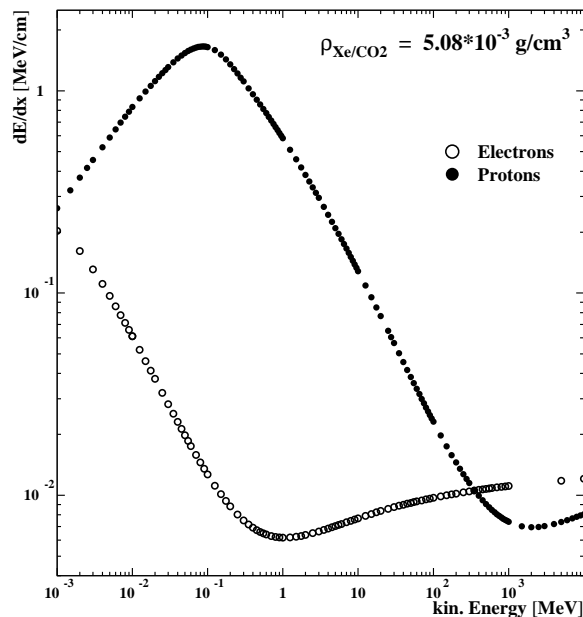


Figure 3.4: Calculated energy loss of electrons and protons in Xe/CO_2 , at standard conditions (NTP), as a function of their kinetic energy according to Bethe-Bloch [37].

There are three effects, the photoelectric effect, first correctly interpreted by Einstein⁶, the Compton effect and the pair production, that can transfer the photon energy to charged particles. The pair production, though, can be left out of consideration for the x-ray energy range of TR photons. This is because the photon necessarily has to have an energy⁷ greater than one MeV to produce an e^+e^- pair.

In general, the attenuation of a beam of photons is described by the Lambert-Beer law, which states that the original intensity I_0 of a photon beam is reduced on its passage of length x through an absorber material, according to [38]:

$$I(x) = I_0 \cdot \exp\left(-\frac{\mu(E)}{\rho} \cdot \rho \cdot x\right) \quad (3.15)$$

In this formula the term $\frac{\mu(E)}{\rho}$, where ρ signifies the density of the absorber material, is called the mass attenuation coefficient. The expression $\rho \cdot x$ is referred to as the mass thickness, which can be considered as a cross-sectional target for a photon, as it traverses the material. Both expressions are attributes of the absorber material, with the absorption coefficient $\mu(E)$ being dependent on the photon energy.

The mass attenuation coefficient denotes the mean number of interactions of the incident photon beam with the absorber material, within a density normalized unit length. The absorption processes occur independently and thus the total absorption coefficient is calculated as the sum over all process contributions:

$$\mu = \mu_{ph} + \mu_C + \mu_{pair} \quad (3.16)$$

⁶Nobel Price 1921

⁷ $E_{ph.} \geq 2 \times m_e$

Photoelectric Effect In the photoelectric effect the photon transfers all of its energy to an orbital electron of a gas atom. Figure 3.5 schematically shows such a photoelectric interaction. The energy is imparted to the orbital electron in the form of kinetic energy E_{kin} amounting to $E_{kin} = E_{\gamma} - E_b$, where E_b is the binding energy of the electron. The electron is knocked out of its orbit and the gap, that it leaves behind, is filled by cascading electrons from higher energy levels. The liberated binding energies from these de-excitations is radiated via fluorescence photons and usually absorbed within the same detector volume. The emitted photoelectron deposits its energy inside the gas, via ionisation energy loss.

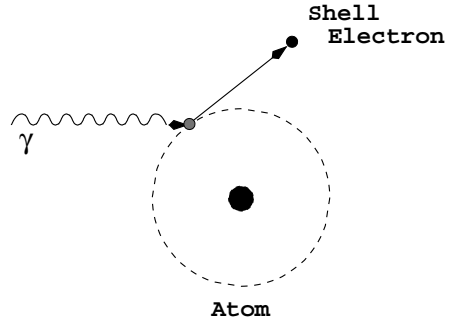


Figure 3.5: *Schematic illustration of the photoelectric effect.*

The photo-effect occurs, with maximum probability, when the energy of the photon is equal to the binding energy of the electron, see figure 3.6. The tighter the electron is bound to the nucleus, the higher the probability. That means most of the photo-electrons are inner-shell electrons, for x-ray photon energies. The energy range in which the photo-effect is dominant is on the order of the electron binding energy of the absorber material. Thus, it is the predominant effect for the x-ray energy range (1 – 40 keV) of transition radiation. Figure 3.6 shows the absorption coefficient due to photo-effect as a function of energy inside a $Xe/CO_2(80/20)$ gas mixture.

Element	Threshold energies [keV]				
	K	L_1	L_2	L_3	M_1
Xe	34.56	5.45	5.10	4.78	1.15

Table 3.1: *K-, L- and M- atomic shell energies for the element Xenon [39].*

Within the plotted course of the absorption coefficient, characteristic edges can be seen, where the absorption probability drastically rises. These edges represent those energy thresholds, where the photon energy exceeds the binding energy of an orbital electron from a lower shell level. In table 3.1 the dedicated energies of these absorption edges are summarised for the chemical element Xenon.

Compton Effect The underlying principle of the Compton effect can be described as a mechanical two body impact, similar to that of two billiard balls. A photon is scattered off an electron, bound to an atomic nucleus, as figure 3.7 schematically displays. This phenomenon is called Compton scattering if the photon's wavelength is much smaller compared to the atom's diameter, and Rayleigh scattering if the photon's wavelength is much larger. In case of Rayleigh scattering the

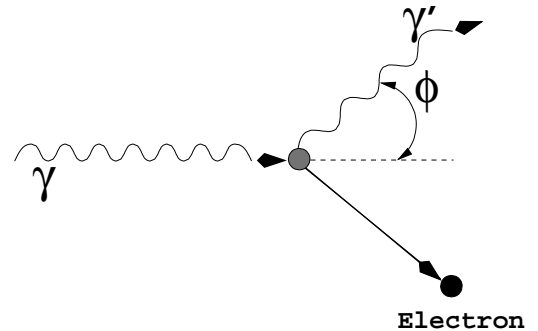


Figure 3.7: *Schematic illustration of the Compton effect.*

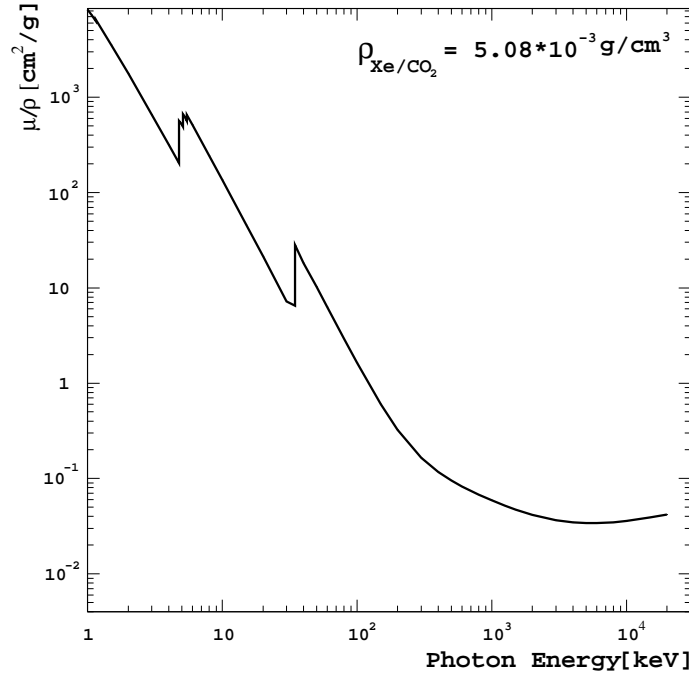


Figure 3.6: Absorption coefficient in a Xe/CO_2 gas as a function of γ energy [39].

collision is elastic and neither the photon's nor the electron's energy is changed, only the photon is deflected. As for the Compton scattering ($E_\gamma \geq 100 \text{ keV}$) the collision is inelastic, energy is transferred to the electron, which is thus knocked out of its atomic orbit, and the wavelength of the photon is increased. The final wavelength λ_f of the photon is greater than its initial λ_i by an amount of [1]

$$\Delta\lambda = \lambda_f - \lambda_i = \frac{h}{m_e c} \cdot (1 - \cos\phi) \quad (3.17)$$

Today, this change in wavelength is called the Compton Effect. Compton's experimental verification of this formula provided the convincing evidence that photons are indeed massless particles that nonetheless carry momentum⁸. Using this formula the scattered photon's energy $E_{\gamma'}$ can be calculated to

$$E_{\gamma'} = \frac{E_\gamma}{1 + \frac{E_\gamma}{m_e c^2} \cdot (1 - \cos\phi)} \quad (3.18)$$

where m_e is the mass of the electron, ϕ is the scattering angle and E_γ the initial photon energy. As can be seen from this formula, the maximum energy loss, at $\phi = \pi$, for the scattered photon is limited to the so called Compton energy, E_C . According to this, the energy spectrum of a monochromatic γ -emitter shows, additionally to the photopeak, a so called Compton continuum in the energy range between 0 and the energy $E = E_\gamma - E_C$. The resulting energy spectrum shows such a continuum in those cases when the scattered photons run out of the detector material and thereby only deposit part of their full energy in the proportional gas.

⁸according to $E_\gamma = hc/\lambda = pc$

3.2.3 The gasfilled Proportional Chamber

The basic configuration of a proportional chamber, as shown in figure 3.8, consists of a cylindrical container with conducting walls, filled with a noble gas like Xenon, as described above.

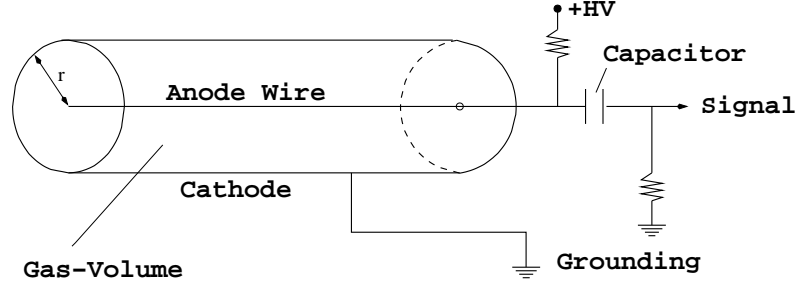


Figure 3.8: Schematic illustration of a proportional chamber [40].

Along the cylinder's axis a conducting wire, $\varnothing(20-50)\mu m$, is strung to which a positive voltage $+V_0$, $\sim 1.5 kV$, relative to the grounded walls is applied. The radial electric field E that is established inside this cylindrical capacitor can be calculated from [40]

$$E(r) = \frac{V_0}{\ln(b/a)} \cdot \frac{1}{r} \quad (3.19)$$

where r is the radial distance to the wire, a and b are the radii of the wire and the inner cylinder, respectively. All effects specified in the last section result in the production of primary electron-ion (e^-/i^+) pairs inside the Xenon, referred to as the proportional gas. The mean number of e^-/i^+ pairs is proportional to the energy deposited inside the gas.

Gas Amplification Under the force of the applied electric field the charges are separated. The negatively charged electrons are accelerated towards the anode wire, whilst the positively charged ions drift toward the cylinder wall (cathode). As the name already indicates, the chamber is used in the proportional mode, where the electric field is strong enough to accelerate the liberated electrons. The amount of energy transferred, enables these primary electrons to ionise gas atoms themselves. The electrons, liberated in these secondary ionisations, are accelerated to produce even more ionisation. This continues to form an ionisation avalanche or cascade. Since the electric field is highest near the wire, the avalanche occurs very quickly and almost entirely within a distance of a few radii around the wire. The proportional mode now stands for a voltage region, where the number of e^-/i^+ pairs in the avalanche is still proportional to the number of primary ionisations. Against the unanimous idea, the generated positive ions account for 99 % of the current induced in the wire, which is then read out via decoupling capacitor and preamplifier. The resulting gas amplification can amount to factors as high as 10^6 , without losing the proportionality to the primary energy deposition.

Wire Centering This gas amplification is highly dependent on the mechanical accuracy of the wire centering, as displayed in figure 3.9. In the example given in the figure, a $100 \mu m$ wire displacement off the center is additionally enhanced to $160 \mu m$ by the such created slight asymmetry of the electric field, which causes a change in the gas amplification by 1.5 %. It is this effect that makes a high mechanical accuracy in the wire centering necessary.

On the other hand, the known effect of gravitational sagging of wires is irrelevant for the low gravity environment on board the ISS. For that reason the wire tension (100 *g*) can be kept relatively low.

Quencher Gas In addition to the proportional gas, a small percentage of a so called quencher gas has to be admixed. This is necessary for two reasons. On the one hand the ions get neutralised at the cathode. The binding energy of the electron, gained back, is liberated by the emission of a UV⁹ photon. Additionally, excited Xenon atoms, formed in the avalanche, emit similar energetic photons during their de-excitation.

At the cathode, these photons can convert into an electron, using the photoelectric effect, and start a new avalanche. This effect can be remedied by the addition of a poly-atomic gas, such as CO_2 . The molecules of this gas act as a quencher absorbing the radiated photons and then dissipate this energy via dissociation or elastic collisions.

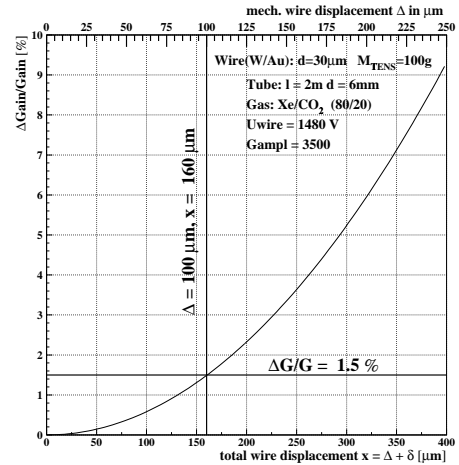


Figure 3.9: *The effect of mechanical wire displacement on the gas amplification [41].*

3.3 The AMS Transition Radiation Detector

The AMS Transition Radiation Detector (TRD) has 20 layers of gas filled tube detectors covered with 22 *mm* radiator. The uppermost 4 and lowermost 4 layers are oriented parallel to the field lines of the AMS magnet, whilst the central 12 layers are arranged perpendicular to it. This is to gain particle track information in X- and Y-directions, outside the central magnetic field. Each radiator consists

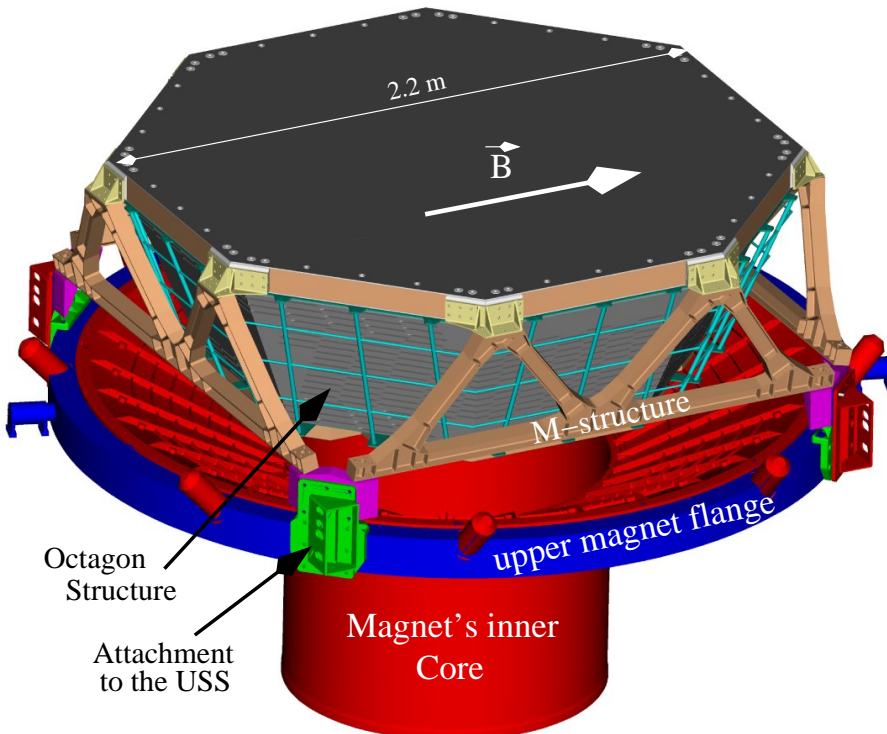


Figure 3.10: *AMS TRD mounted on the upper flange of the magnet.*

of a polypropylene fiber material. The detector layer is made out of single wire proportional tubes, filled with a Xe/CO_2 (80/20) gas mixture. The tubes have an inner diameter of 6 *mm* and a central gold plated (\varnothing 30 μm) tungsten wire. 16 such straw tubes, in combination with longitudinal and vertical carbon fiber stiffeners and two polycarbonate end-pieces, are glued together to build detector modules with lengths varying from 0.8 to 2.2 *m*. The total number of such modules will comprise 328, which will be arranged

⁹ultraviolet energy, ranging from (3.1 – 124)eV

in a conical octagon support structure for mechanical stability. The entrance and exit windows of this octagon structure will be closed by Carbon Fiber Composite (CFC) honeycomb plates. This full TRD will then be mounted onto the upper flange of the magnet and sandwich the upper time of flight (ToF) system in-between itself and the magnet. The TRD will have its own "M" shaped support structure with which it will be attached to the AMS-02 unique support framework (USS-02). Figure 3.10 shows the complete TRD placed on top of the upper magnet flange.

3.3.1 Radiator

The AMS Collaboration decided to use the same, highly irregular, radiator material, as will be used for the ATLAS Transition Radiation Tracker (TRT). Tests, performed by the ATLAS Collaboration, have shown that the chosen fiber radiator decreases the TR yield¹⁰ by only 10 – 15 %, compared to that of a regular foil stack [31, 42]. Radiator tests, carried out by the Aachen I¹¹, with two different fiber and one foam material, have shown the best TR performance for the ATLAS material [43].

This fleece material¹² consists of polyethylene/polypropylene fibers with a mean fiber diameter of $\sim 10 \mu m$, and an overall density of $0.06 g/cm^3$. The fleece is cut into sizes such that a straw module, as a whole, is covered by a 22 mm thick radiator. For the total TRD an accumulated area of $\sim 50 m^2$ has to be covered by such radiator material. In order to meet the NASA space qualification requirements concerning the outgasing and thus deposition rate on nearby attached payloads on the ISS, the fleece material is chemically cleaned¹³. The radiator tests, carried out with the 20-layer-prototype, have shown that this cleaning does not affect the TR performance (see section 5.2 for details).

3.3.2 Straw Module

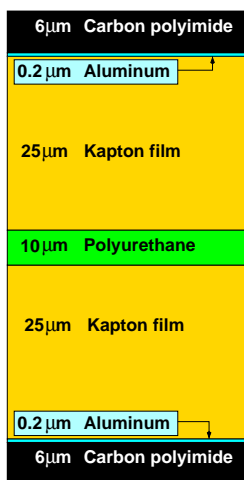


Figure 3.11: *Straw wall cross section.*

A straw module comprises 16 cylindrical proportional tubes with a diameter of 6 mm and a tube wall thickness of $72 \mu m$, each. The individual straws are fabricated from a multilayer foil predominantly made out of Kapton material. Figure 3.11 shows the cross section of such a straw wall. At the center, this straw wall consists of a $10 \mu m$ polyurethane layer, sandwiched in-between two $25 \mu m$ Kapton films. The outer surfaces of both Kapton layers are covered by a thin aluminium metalisation and a $6 \mu m$ carbon polyimide layer. Along the axis of each such cylindrical tube a gold plated tungsten wire, with $30 \mu m$ diameter, is strung. Together with 6 longitudinal carbon fiber stiffeners all 16 straws are glued together and, at both ends, glued into polycarbonate (PC) endpieces. Additionally to the longitudinal ones, transversal carbon stiffeners are glued onto the modules, perpendicular to the tubes and with a 10 cm spacing, to further improve the mechanical stability of each module. Figure 3.12 shows the cross section and a photo of such a straw module. The mentioned PC endpieces serve various purposes. They accommodate the wire fixations (*CuTe* pieces) [44], they are

¹⁰above an energy deposition threshold of 6 keV in their detector tubes

¹¹members of the 1. Physikalisches Institut of RWTH Aachen

¹²LRP 375 BK, manufactured by Freudenberg Vliesstoffe KG

¹³Organic Chemistry Institute of RWTH-Aachen; Soxhlett extraction method, using CH_2Cl_2 [46]

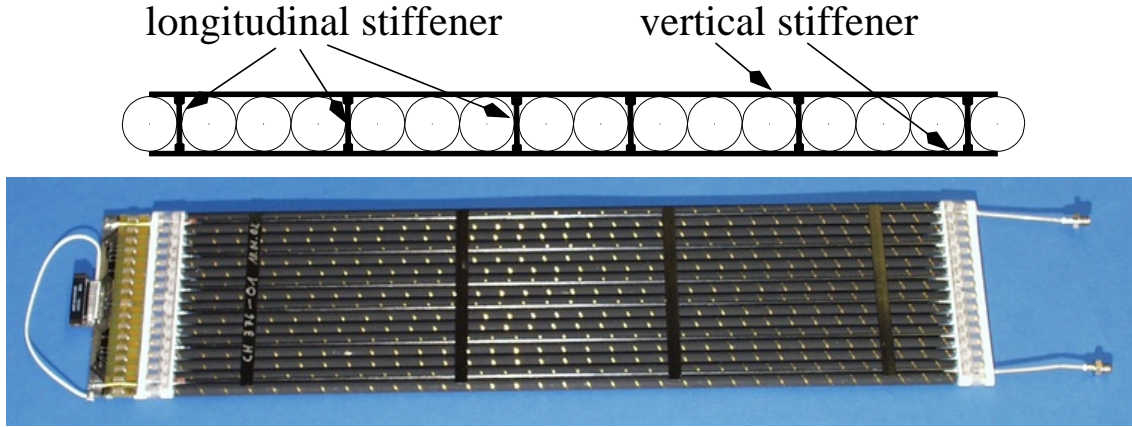


Figure 3.12: a) Cross section and b) photo of a straw module.

used as gas manifolds to the straws as well as guarantee the electrical insulation for each wire. At the module's gas supply side gas inlet and outlet tubes are fed into the endpiece, as figure 3.12b shows. The gas distribution channel inside this endpiece is disconnected in its center, which causes the gas to flow through the first 8 straws in one direction and reversed through the second half of the straws. This ensures a uniform gas distribution within the module.

On the opposite side of the module the $CuTe$ endpieces are soldered to the electronics Tube Endpiece (UTE) board. This UTE¹⁴ board connects each of the 16 wires, via a $2\text{ M}\Omega$ protection resistor, to the high voltage. It also decouples the wire signal from the high voltage, using a 150 pF high voltage capacitor, as displayed in figure 3.8. A flexible jumper cable connects all 16 signal wires with the further readout electronics, which will be described in the following section.

3.3.3 Electronics and DAQ

The TRD electronics, as figure 3.14 sketches, can be subdivided into "Front End" and "Crate" Electronics. The first named part is mounted directly onto the detector or closely to it onto the octagon support structure. The second part can be found gathered into two identical crates attached to the USS.

Front End Electronics The front end electronics consists of 3 main parts: the Tube Endpiece board (UTE), as part of the straw module described at the end of last section, the Front End readout board (UFE) and the High Voltage Distribution board (UHVD). The front end

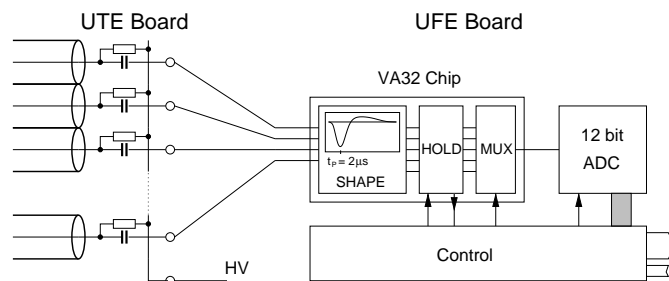


Figure 3.13: The front end electronics scheme.

readout schematic is visualised in figure 3.13. Each group of four straw modules is connected to one UFE board, performing pre-amplification, shaping and signal digitalisation for all 64 wires connected to it. The same groups of four modules are biased from one high voltage channel of the UHVG board (see below), distributed to each module via UHVD board. That means, to supply HV to and readout all 328 modules, 82 UFE and UHVD boards are necessary, which as a whole consume 18.5 W .

¹⁴the letter "U" is to identify the TRD-electronics, from the german word "Übergangsstrahlung" (TR).

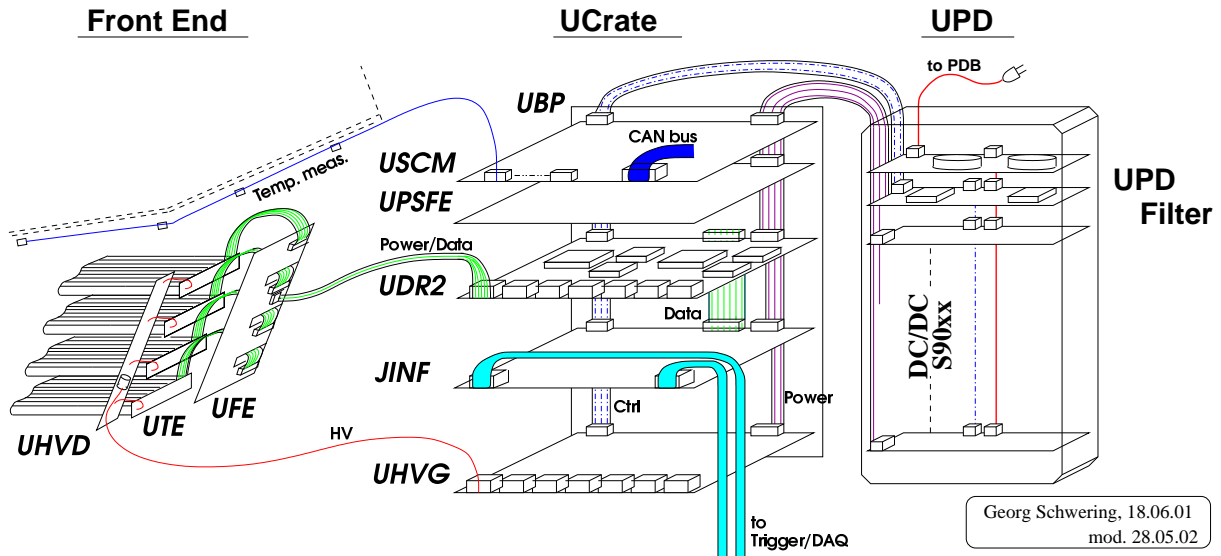


Figure 3.14: *TRD electronics design.*

To process the signals two VA32hdr12 chips¹⁵ are used on each UFE, which contain preamplifier, $CR-RC$ shaper, "sample and hold" as well as an output multiplexer for 32 channels each. The basic specifications of the chips are a dynamic range of $\pm 1500 fC$, at an equivalent noise charge (ENC) of only $0.56 fC$, and a peaking time of $2 \mu s$. These parameter settings enable measurements with the TRD modules in the range of 0.2 to 20 MIPs, at a high voltage set to $1.5 kV$ equivalent to a gas amplification of ~ 3000 . In each of the channels the amplified and shaped signal is stored, until it is sent, via multiplexer, to the single 12bit ADC, on board each UFE, to be digitised. Figure 3.15 shows a photo of such an UFE board. The VAs (not shown in the figure) are placed on the outer corners of this board. The open areas are feed throughs for the jumper cables connecting UTE and UFE. Using the socket placed in-between the two VAs the digitised data are serially transferred to one of the Data Reduction boards (UDR) with a transfer rate of $16.7 Mbits/s$. These UDRs are already part of the crate electronics.

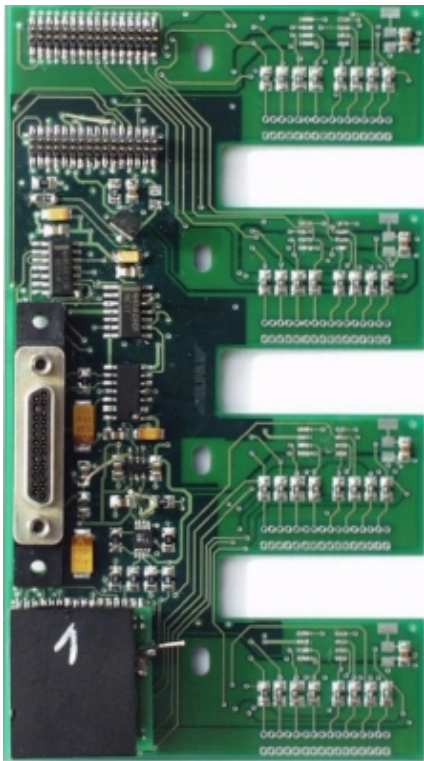


Figure 3.15: *Photo of an UFE board.*

various low voltages are generated using DC/DC converters. Via the crates Back Plane (UBP) these voltages are distributed to the different boards with the aid of UPSFE¹⁶ boards in the case of the front end electronics.

¹⁵manufactured by IDEAS (Integrated Detectors & Electronics AS)

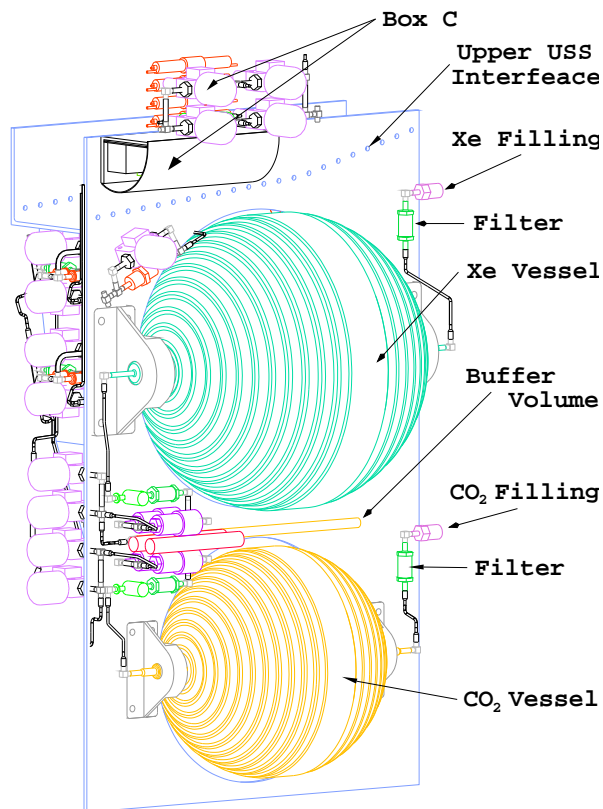
¹⁶Power Supply for Front End Electronics

The crate electronics as well contain the so called "Slow Control" which monitors and controls the power of all boards in the TRD crates as well as reads out the temperature sensors via Slow Control and Monitoring board (USCM) [45]. The main tasks on Data Acquisition (DAQ) inside the crates is done by the Data Reduction boards (UDR), which read out the digitised data from 7 UFE boards, each. The UDRs receive the level-1 trigger, generate the readout sequence for the UFE boards and read out 7 ADCs in parallel. On board each UDR a DSP¹⁷ compresses the data and sends them on request to the JINF board. This JINF board serves downstream as a command distributor and upstream as a data concentrator that transfers the data from UDR to the higher DAQ. For further details refer to [46] and the webpage [47].

3.3.4 Gas Supply System

The AMS TRD is making use of a recirculating gas supply system, as illustrated in figure 3.16 and referred to as "Box S", that is produced by a group from MIT¹⁸. The gas system consists of two individual vessels, to store the gas components, separately. The net weight of this gas system is 67 kg and will carry 50 kg of gas, corresponding to 8100 l Xe and 2000 l CO₂ gas, at 1 atm. About once a day, gas will be mixed inside the mixing vessel D (mounted to the back plane, and thus not shown in fig. 3.16), which releases small gas amounts into the circulation module, "Box C", several times per day. Each transfer, from the mixing vessel, is limited to less than 7 liters of gas at 1 atm.

The gas supply scheme foresees a sequential connection of 8 straw modules to build gas circuits of maximum 8 liters active volume. In that way, the gas runs sequentially through all modules of one circuit. All together 41 separate circuits will be built to supply gas to all 328 modules. Each gas circuit is individually attached to the input and output manifolds via pressure controlled isolation valves, and 3 mm steel tubing. These valves are part of the isolation system that is constantly measuring the pressure inside each gas chain. Controlled by a computer this system directly closes all valves, leading to one chain, in case of a sudden pressure drop. It is also capable of detecting an increase in gas consumption, solely for every single isolation segment, over longer periods of time. The input and output manifolds are located on the top rim of the TRD from where 6 mm stainless steel gas lines run back to "Box C" for the gas to be recirculated. For further details see [48].



R.Becker 03/05/02

AMS
Alpha
Magnetic
Spectrometer
Integration MIT

Figure 3.16: TRD gas supply system [22].

¹⁷Digital Signal Processor

¹⁸Massachusetts Institute of Technology

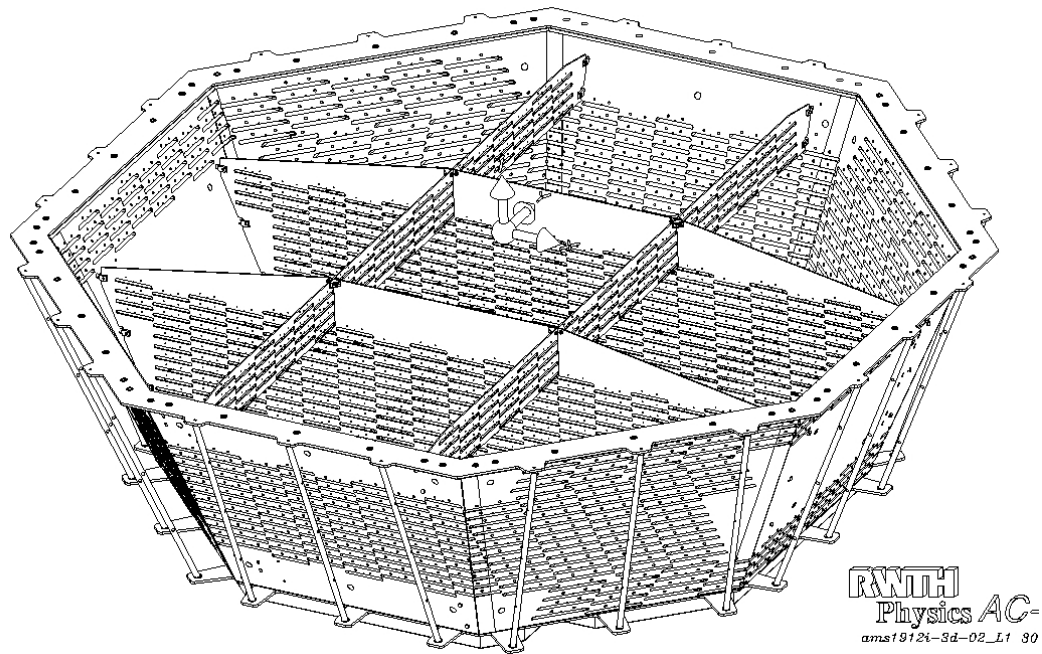


Figure 3.17: 3D view of the TRD octagon support structure [46, 49].

3.3.5 Mechanical Support Structure

The mechanical support structure comprises two main parts. On the one hand there is to name the octagon support structure that, together with its bulkheads, directly firm up the straw modules. On the other hand the so called M-structure is to mention, that supports the TRD as a whole.

The main purpose of the conical octagon structure, as figure 3.17 displays, is to hold the modules, and their associated radiators, and to keep them in position with reference to each other. In combination with the so called M-support framework it is responsible to provide the necessary mechanical stability for the modules to sustain the high acceleration forces during the shuttle launch and landing.

The octagon structure is built out of a carbon fiber and aluminium honeycomb sandwich material. The structure is machined to a $100\ \mu\text{m}$ precision, to avoid wire displacements or wall deformations of tubes, causing a change in the gas amplification, as explained earlier in this chapter (see page 32). The sidewalls are manufactured out of a $26\ \text{mm}$ thick aluminium honeycomb sandwiched in-between two $2\ \text{mm}$ thick carbon CFC skins. A reinforcement ring is mounted on top of the sidewalls, for further mechanical stability. A grid of carbon fiber tubes is joined to this ring, and the lower TRD collar, to support services, like the gas tubing or HV and signal cabling. The inlet and outlet windows of the octagon are closed for extra mechanical stability and shielding and thermal separation purposes by bodywork similar to that of the sidewalls. The lower plate has a material thickness of $41\ \text{mm}$, with $0.5\ \text{mm}$ CFC skins, whilst the upper one is $94\ \text{mm}$ thick, with $1\ \text{mm}$ CFCs. The upper closure is supported by the M-structure made out of aluminium beams with a "double T" shaped cross section. With the aid of this M-structure the TRD will be attached to the USS.

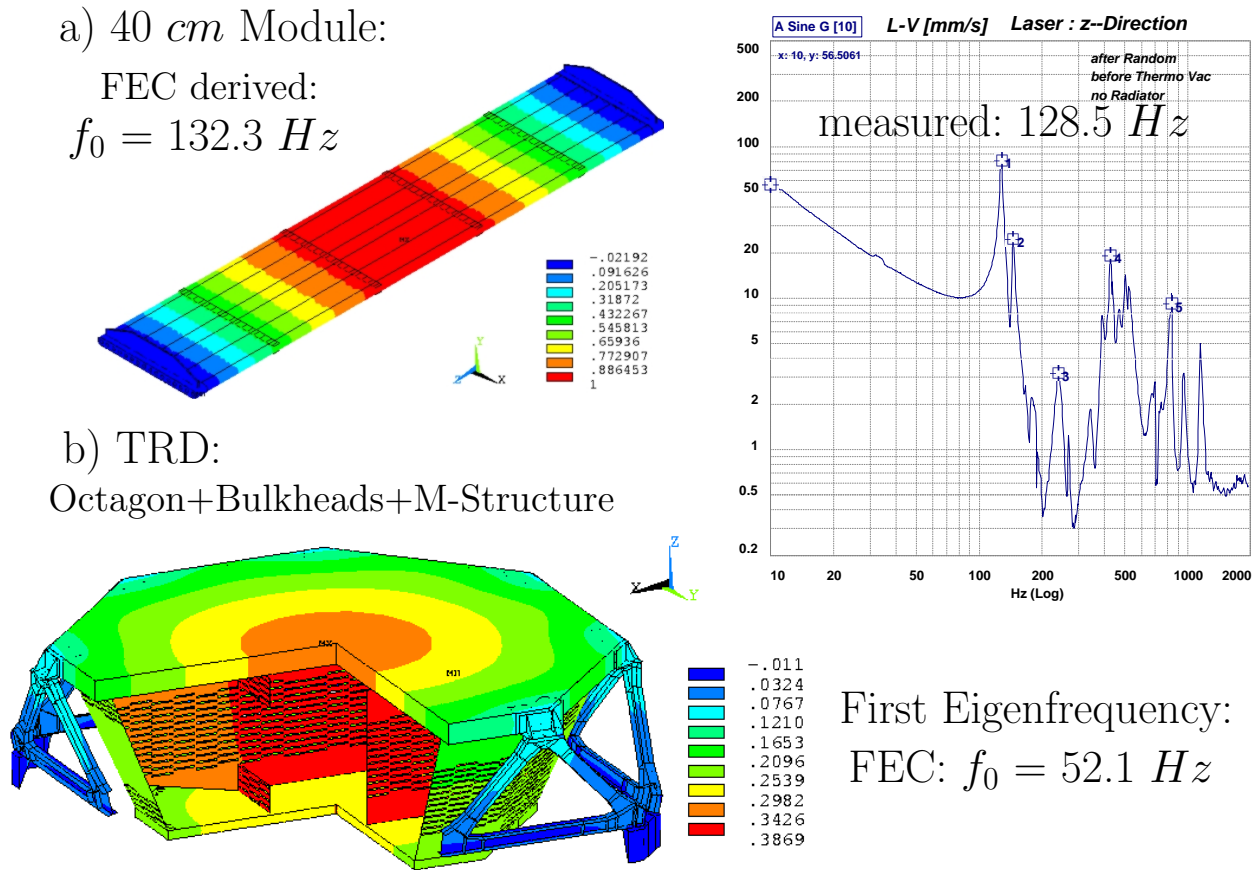


Figure 3.18: a) Z-displacement, derived from finite element calculations, for a 40 cm straw module and comparison of the calculated and measured first eigenfrequencies; b) Z-Displacement and eigenfrequency calculation for the TRD support structure (Octagon, Bulkheads and M-structure).

3.3.6 "Structural Verification"

Finite element calculations are performed, to test the described TRD subsystem, integrated into the M-structure, for the NASA requirements on "Structural Verification". The "Structural Verification Plan" [50] of NASA deals with the mechanical stability and durability of the detector and its components. Special concern is given to the detector's modal properties and the effect of the environmental conditions in space on the detector. For that reason all components have to undergo several vibration and thermo-vacuum tests to check the NASA requirements.

Vibration Tests Most of the testing on the vibration properties is carried out, using detailed Finite Element Calculations¹⁹ (FEC). A coupled load analysis of the entire TRD structure was performed, using such simulations. To verify those results the first eigenfrequency of vibrations perpendicular to the module plane, referred to as "z-displacement", for a single straw module is calculated from FEC and measured on a vibration table. As figure 3.18a shows, the measured and calculated results are in good agreement, with only 3 % relative difference between the two results. The colours indicate the magnitudes of deflection relative to the maximum.

¹⁹by I.S.A.tec Engineering, Aachen

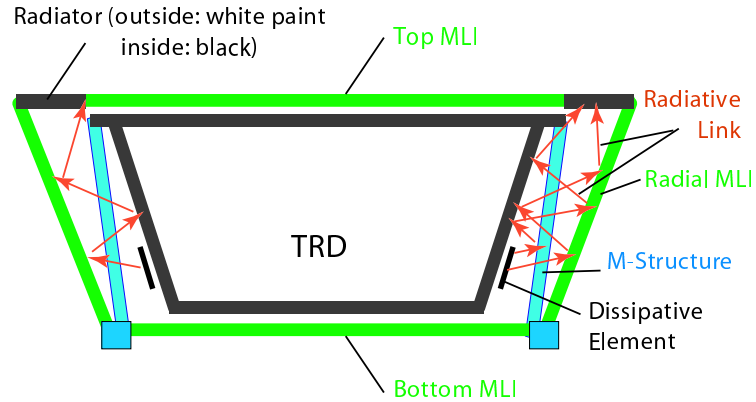


Figure 3.19: Thermal model of the TRD subsystem, wrapped in an Multi Layer Insulation.

In the same precise manner, the TRD support structure, including the Octagon together with its bulkheads as well as the M-structure, is implemented and the first eigenfrequency is calculated. The maximum displacement as indicated by the red areas in figure 3.18b, refers to $\sim 700 \mu\text{m}$ and the first eigenfrequency, calculated to 52.1 Hz , fulfills the NASA requirement to be above 50 Hz . For further information one may refer to [46].

Thermo-Vacuum Test The thermo-vacuum test is carried out to check the durability of each detector component in an environment similar to that on board the ISS. For that reason the test item is placed into a vacuum tank and the temperature is 8 times cycled in the range from $(-40 \text{ to } +60) \text{ }^\circ\text{C}$, as displayed in figure 3.20. The time for one full cycle is $\sim 6 \text{ hours}$, which is the minimum possible for the used experimental test set-up. After such a thermo-vacuum test the gas-tightness test for straw modules, and vibration tests, for all test items, have to be repeated.

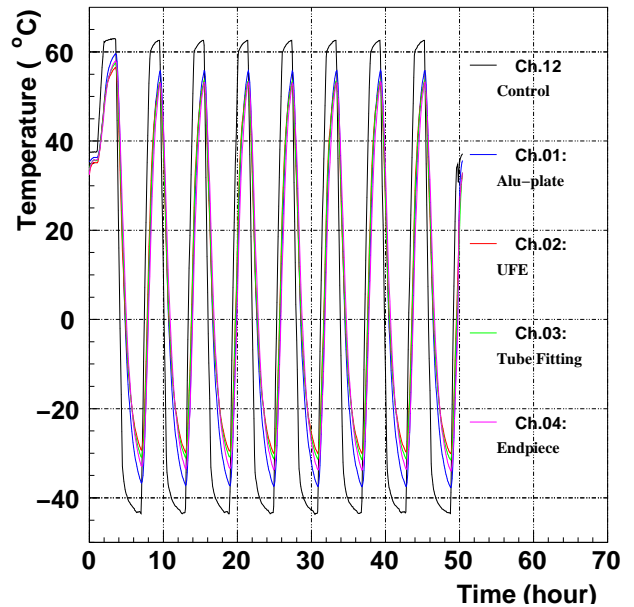


Figure 3.20: The 8 thermo-cycles of a thermo-vacuum test [51].

3.3.7 Thermal Model

To guarantee stable conditions for the operation of the TRD straw modules a thermal model of the detector is developed to optimise the isolation from the outside temperatures and to dissipate the energy, radiated by the Front End Electronics, to the environment. For the thermal shielding the TRD, together with its M-structure, will be wrapped in a Multi Layer Insulation (MLI)²⁰, as displayed in figure 3.19. Integrated into this insulation material, placed at the outermost edges of the upper TRD cover, radiator areas serve as "heat sinks" to dissipate the heat (infrared radiation) emitted by the electronics to the environmental space surrounding the AMS detector.

²⁰MLI stack: 19 perfor. Mylar foils, thickn.: $250 \mu\text{m}$ + PETP spacers, wrapped in $2(1) \text{ mm}$ perforated Mylar foil outside(inside).

A preliminary thermal analysis²¹ of a such defined model, for four different inclination angles of the ISS' orbit towards the sun, indicates the technical feasibility to keep the temperature gradient, ΔT , inside the TRD, below $1K$ [46]. In this simulation, the outer surface temperature of the MLI drastically changed during an ISS' orbit, while the inner surface temperature remained stable over the full orbit.

²¹carried out by OHB Systems

Chapter 4

The TRD Prototype

The AMS Transition Radiation Detector was designed to have best particle identification performance within the given limits of size, weight, mechanical stability and electrical power consumption. Simulation studies were performed to optimise the detector layout, using a GEANT 3.21 Monte Carlo software with additional features to generate and detect transition radiation. The details of this simulation "business" will be dealt with in a separate chapter. These Monte Carlo simulation studies varied the number of layers and the thickness of the radiator layer, but still kept the overall detector height below 60 *cm*. These studies finally resulted in the choice of a detector layout as presented at the end of the previous chapter.

In total, 4 steps of prototyping were performed to check the feasibility of this found TRD design. The first step dealt with a (6×10) *cm*² single layer prototype, with which, for the first time in this project, transition radiation was detected by the AMS TRD group. The special features of this first prototype were its tubes with squared cross sections and a read out cathode, segmented into strips, with a tracking resolution of about 100 μm [43]. The second and third prototype were already using straw modules with 40 *cm* length similar to those described in the previous chapter. The second prototype consisted again only of one single detector layer, while the third comprised three successive detector layers interleaved with radiator material. Both prototypes were subjected to short beamtests at CERN with only a few weeks intermission, at the end of 1999 [53]. After the successful completion of the tests with this third, 3-layer prototype, a 20-layer prototype was designed and built in Aachen. Finally, it was subjected to two high energy beam tests, in summer 2000 at CERN. The performance of this final 20-layer prototype is the subject of this thesis and for that reason this prototype, and the technical details of the beamtests, will be described in the scope of this chapter.

4.1 Laboratory Preparations

Besides the transition radiation performance and final radiator tests, the building stage for this prototype represented a technical feasibility study for the series production of straw modules. For that to be realistic, each of the modules passed through most preparation steps, as foreseen for the final TRD modules. The following section will briefly introduce the reader to this building sequence, as figure 4.1 illustrates, since it includes detailed information on the prototype. Additionally, it gives an overview of all the necessary tests for the final modules. For details on this module production scheme, one may refer to [23].

Mechanical Module Assembly The straws, together with longitudinal and vertical stiffeners, made of carbon fiber material, are glued together at FVT Faserverbundtechnik GmbH in Aachen. After their delivery to the 1. Physikalisches Institut of RWTH Aachen, the polycarbonate (PC) endpieces are glued to both ends of the straws. Next step is, to feed a wire through each of the straws and string them with a tension of 100 g [54]. On both sides, they are crimped into $CuTe$ pieces, held by the PC endpieces. With this method the wire can be placed in the center of the tube with an accuracy of better than $20 \mu m$ [44]. To check for electrical contact the resistance is measured, referred to as "Signal FeedThru Test", in the flow diagram.

Wire Tension Test The routine foresees a wire tensioning test as next step. To measure the wire's tensile stress the module is placed on top of a permanent magnet and an electric impulse is applied, one by one to the wires. The wire oscillates in the magnetic field and the eigenfrequency of this oscillation is obtained. This eigenfrequency is related to the wire tension. This test will be done for the final modules, but has not been performed for those of the prototype [55].

Preview Test The preview test represents the next testing stage, applied to the construction of each module. It is designed to measure the electric noise¹ of each wire, at a stage, where they still can be replaced. The modules are not gas tight at this stadium and for that reason they are integrated into a vacuum tank, which is filled² with Ar/CO_2 , used as protective gas. The test setup, as illustrated in figure 4.2, foresees a high voltage supply of 1.65 kV to the wires, via a non-permanently attached UTE board, and the signals from them read out, using a preamplifier and shaper. Signals, above an applied

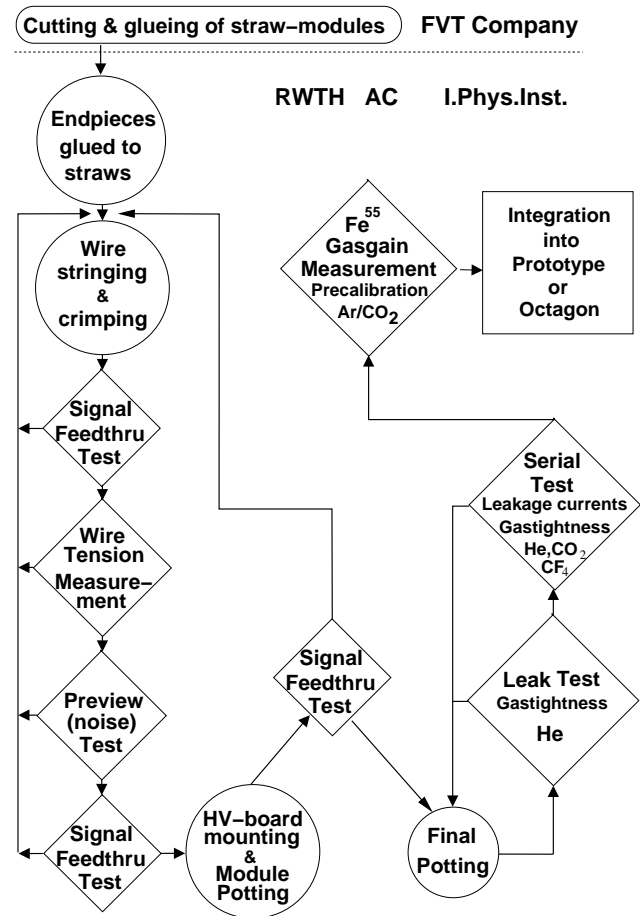


Figure 4.1: Building sequence for the straw modules.

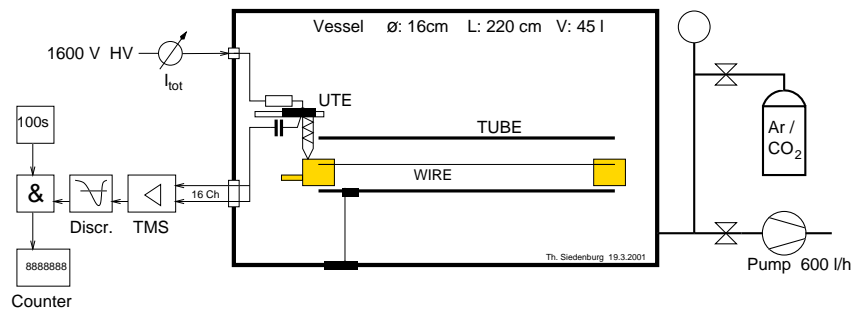


Figure 4.2: Schematic illustration of the Preview Test.

¹due to "dirt" induced discharges

²upto a pressure of 1 atm.

threshold of twice the pedestal width, are counted and wires that have a count rate³ exceeding 10 Hz , or 150% of the average measured count rate for this module, are replaced. For those modules, that passed the tests mentioned so far, the mounting of the permanent UTE board and the module's final potting follows. The latter named is to seal the modules gastight. Up to this final potting wires still can be replaced and for that reason a last "Signal FeedThru Test" is performed in advance.

Leak Test The leak test is a first test to check for macroscopic gas leaks, like punctures or cracks in the straw wall, done at surrounding atmospheric pressure. This test is done with Helium, for the "flight" modules, and served as the only gas tightness test for the prototype modules. In order to do so, the "flight" modules are filled with gas up to an overpressure of $\sim 1.7\text{ bar}$. Over a period of 6 hours, the pressure drop is measured, using a digital precision pressure gauge with an accuracy of $\pm 0.5\text{ mbar}$. To fulfill the NASA safety requirements all modules have to sustain overpressures of up to 2.5 bar , even. This can be checked additionally at the beginning or the end of such a leak test.

For the prototype modules, this leak test was part of the gas gain test (see below). For that reason, they were filled with Ar/CO_2 gas, at an applied overpressure of $\sim 250\text{ mbar}$. The pressure drop was measured for $\sim 30\text{ mins}$, and carried out with a simple analog pressure meter, with an operating accuracy of $\pm 5\text{ mbar}$.

Serial Test The serial test, as schematically illustrated in figure 4.3, is done for 5 straw modules at a time, serving various purposes. It is the second test only applicable for the final modules⁴. It is to measure the gas tightness of each module, under vacuum conditions, with an applied overpressure of 1.7 bar for two different gases, He and CO_2 . For that reason, gas can be supplied solely to each module and the pressure drop inside each module is monitored, using an equivalent absolute pressure meter, as for the leak

test. The measurements are usually carried out with He gas, because meaningful results can be obtained within 12 hours, which is a factor of 10 faster compared to equivalent tests with CO_2 . This is because, each gas first accumulates in the straw wall and the CO_2 gas has a far longer time constant for this process compared to the He

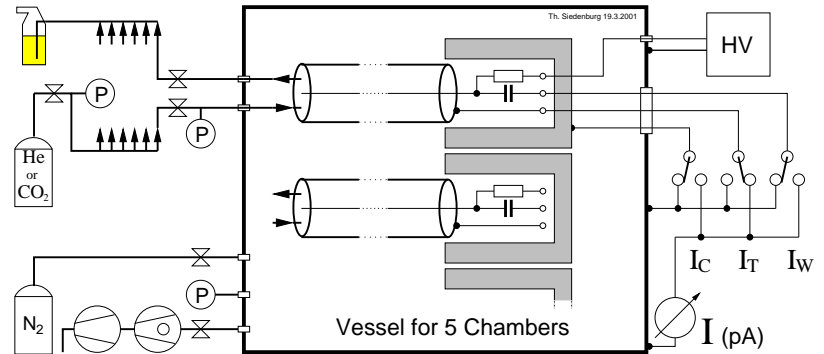


Figure 4.3: Schematic illustration of the Serial Test.

[53]. For a module to be accepted, it has to be gastight down to the diffusion level⁵, within a tolerance factor of 2, only. A second purpose for the serial test is to perform an electric check-up. By doing so, various dark currents, like that of the decoupling capacitor, with respect to the common ground, are measured. If one of these currents, measured as displayed in the figure, exceeds a value of 10 nA the module is discarded.

³referring to a chamber length of 2 m

⁴The serial test has still been at its planning stage, when the prototype was built

⁵ CO_2 gas: $5.1 \times 10^{-5} \frac{\text{L}\cdot\text{mbar}}{\text{s}}$ at 1 bar for a module of 1 m length [53].

4.1.1 Gas Gain Measurements

The used Radioactive Sources For all the measurements, to be described below, a variety of radioactive sources is used, which will be briefly introduced in this paragraph.

$^{54}_{25}\text{Mn}$ is a γ -emitter with a half-life of 314 *d*. It decays, via electron capture, into $^{54}_{24}\text{Cr}$, emitting high energetic 835 keV γ -rays and 5.4 keV Cr K-shell photons.

$^{55}_{26}\text{Fe}$ is a γ -emitter with a half-life of 2.73 *y*. It decays, via electron capture, into $^{55}_{25}\text{Mn}$, emitting 5.9 keV Mn K-shell photons. Figure 4.4a shows an ^{55}Fe energy spectrum, obtained in Xe/CO_2 , with an applied voltage of 1600 V.

$^{65}_{30}\text{Zn}$ is a γ -emitter with a half-life of 245 *d*. It decays, mainly via electron capture, into $^{65}_{29}\text{Cu}$, emitting high energetic 1114 keV γ -rays and 8.0 keV Cu K-shell photons.

$^{90}_{38}\text{Sr}$ is a β^- -emitter with a half-life of 28.1 *y*. It first β^- -decays into the intermediate nuclide $^{90}_{39}\text{Y}$, which itself suffers a β^- -decay into $^{90}_{40}\text{Zr}$, with a half-life of 64 *h*. From these two decays electrons with a maximum energy $E_{max} = 2.3 \text{ MeV}$ are emitted.

$^{241}_{95}\text{Am}$ is basically an α -emitter with a half-life of 458.1 *y*. It α -decays into $^{237}_{93}\text{Np}$, which, in the process of its de-excitation, emits several x- and γ -rays. The important spectral lines, employed during the laboratory activities, to be described below, are those from the 14.0 keV, 17.8 keV, 20.8 keV, 26.4 keV and 59.5 keV photon energies. Figure 4.4b displays a spectrum taken during one of the measurement campaigns in Xe/CO_2 gas, with an applied voltage of 1480 V.

Homogeneity Test As the final test in the production chain, the homogeneity of each module's signal output is measured. The measurement is carried out, using Ar/CO_2 gas, an applied high voltage of $\sim 1.5 \text{ kV}$ and the ^{55}Fe radioactive source, to generate a signal inside the proportional tubes. During these measurements, the modules are placed onto a granite block, with a surface flatness

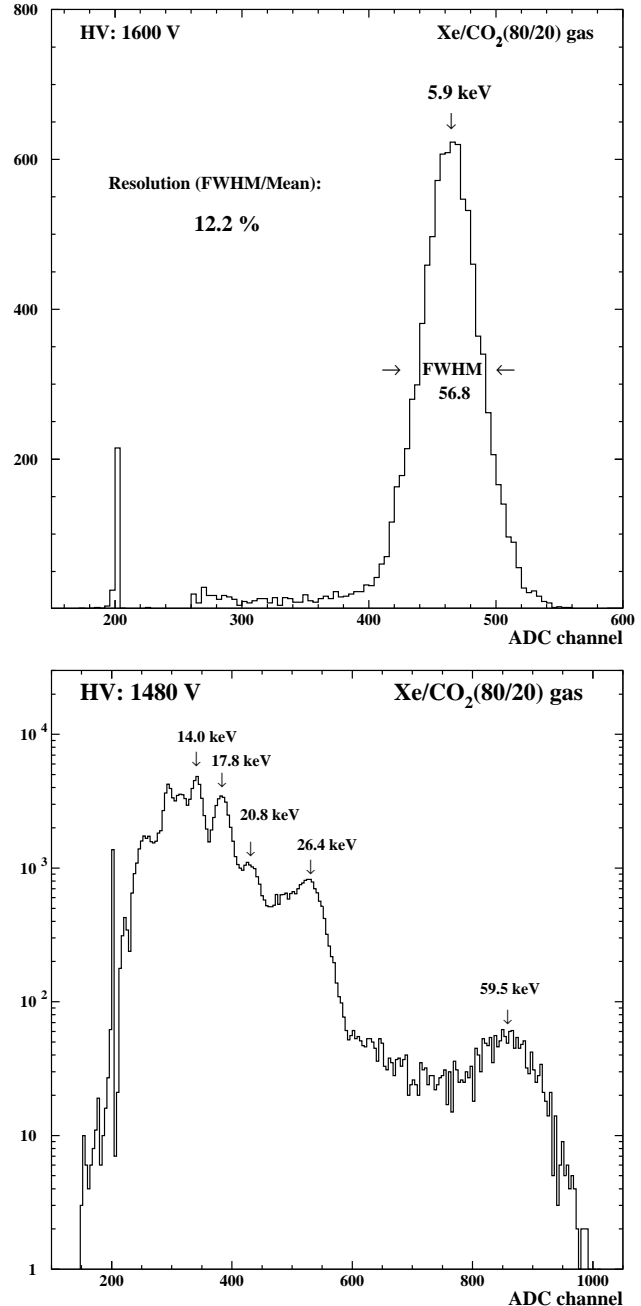


Figure 4.4: a) $^{55}_{26}\text{Fe}$ spectrum; b) $^{241}_{95}\text{Am}$ spectrum detected in Xe/CO_2 gas, at NTP and the indicated anode voltages.

of $5 \mu m$, to avoid any wire displacement off the center or deformation of the tube's circular cross section. Additionally, the temperature and pressure is monitored, in order to correct the measured gas gains for any change in gas density. As quality measure the gas gain homogeneity, for all 16 wires, within one module, has to be better than 2%. Measurements, carried out for the prototype modules already match this quality measure, as figure 4.5 shows. Part of the inhomogeneity, that this plot reveals, refers to impurities in the Ar/CO_2 gas mixture⁶ and another part to a $\sim 10\%$ manufacturing uncertainty in the testpuls capacitors, used for the calibration. All measurements with final modules, carried out with only one preamplifier, and high purity gas⁷, show a typical homogeneity of better than 1%, even.

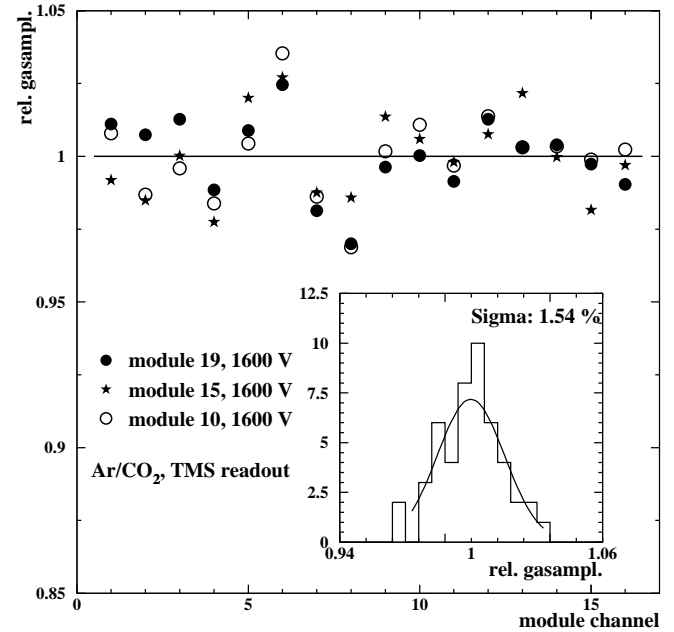


Figure 4.5: *Homogeneity distributions accumulated from 3 prototype modules.*

After the completion of all these tests, one prototype module was chosen to carry out several gas gain measurements. These measurements were investigations on the relative change in gas gain with increasing high voltage, enforced for three different gas mixtures, using one single radioactive source. Secondly, series to try out the change in gas gain as a function of Xe/CO_2 gas density were carried out and repeated for two different γ - and the β - emitter. In a third line of tests, the gas amplification as a function of photon energies was measured and repeated for three different high voltages to look for a possible space charge effect.

Gas Gain Dependency on the used Gas Mixtures At the building stage of the prototype, there was still no conclusive decision about the gas mixture, to be used in the final TRD, achieved. That's why three different gas mixtures, one at a time, were deployed to the same module and gas gain measurements were taken, using the ^{55}Fe radioactive source. The gas mixtures, that came into question, were Xe/CO_2 and Xe/CF_4 , both with percentages of 80/20. Additionally, used as a reference, the measurements were redone with the well known and frequently used Ar/CO_2 (82/18) gas mixture. As a first result of these measurements, like figure 4.6 illustrates, the comparison between the two series, carried out with Ar/CO_2 and Xe/CO_2 gas, is to name. The ratio of gas gains in these two gas mixtures is well known to be roughly a factor of 10 [43], which is nicely reproduced in these two measurement campaigns. The comparison between the results from the two gas mixtures in question, clearly favours the Xe/CO_2 gas, for two reasons. On the one hand, the steeper slope of the Xe/CF_4 distribution is to mention, which enhances small density fluctuations and thus causes the broadening of any energy spectrum.

⁶ Ar/CO_2 (4.6/4.5) purity

⁷ Ar/CO_2 (5.0/4.5) purity

The second disadvantage for the admixture of CF_4 quencher gas is the higher minimum voltage for the gas amplification to set in. Taking into account that the AMS TRD will be operated at an amplification factor of 3000, it would cause an increase in the applied high voltage by roughly 100 V, when choosing the Xe/CF_4 . The real advantage of this gas mixture is the, by a factor ~ 15 , lower diffusion level of the CF_4 quencher gas, in comparison to the CO_2 [53]. Due to the fact that the gas tightness of the modules is an important issue, for any gasfilled detector that is to be operated in space, it is under investigation again, while this thesis is composed.

Gas Gain as a Function of Gas Density These measurement series are carried out to gain a deeper insight into the dependency of the gas gain on the gas density. Especially, it was to check whether this dependency differs for photon absorption (γ -emitter) and continuous ionisation energy loss (β -emitter) measurements. Generally speaking, the gas gain can be described by the following formula

$$G = \left[\frac{U}{\ln\left(\frac{R}{r}\right) \cdot r \cdot E_{min}(\rho_0) \cdot \frac{\rho}{\rho_0}} \right]^{\frac{\ln 2 \cdot U}{\ln\left(\frac{R}{r}\right) \cdot \Delta V}} \quad (4.1)$$

where $U[kV]$ is the applied high voltage, $R[cm]$ is the inner diameter of the straws, $r[cm]$ is the wire diameter and $\rho_0[g/cm^3]$ the gas density at standard conditions. The parameters $E_{min}[kV/cm]$ and $\Delta V[V]$ denote the minimal electric field necessary to start the avalanche and the potential difference to ionize gas atoms, respectively. They are referred to as Diethorn parameters, and will be used as free parameters for the fit (see later).

The first expectation now is, that the γ -emitter measurements can be satisfactorily described by the above given formula. The second expectation is that the measurements, using the β -emitter, show a different behaviour. The expected difference lies in the different ways of energy deposition inside the gas, as described in the previous chapter. If the gas density increases, so does the photon absorption probability, but still the energy deposition from a single photon, and with that the average number of primary electrons, stays the same. The smaller gas gain factor originates from the reduced mean free path length of the secondary electrons on their way to the wire. Due to this, an increased number of electrons cannot gain enough energy, from the electric field acceleration, in-between two interactions with the gas atoms, to liberate more electrons. This results in a smaller number of electrons that create avalanches, and thus the gas gain factor is reduced.

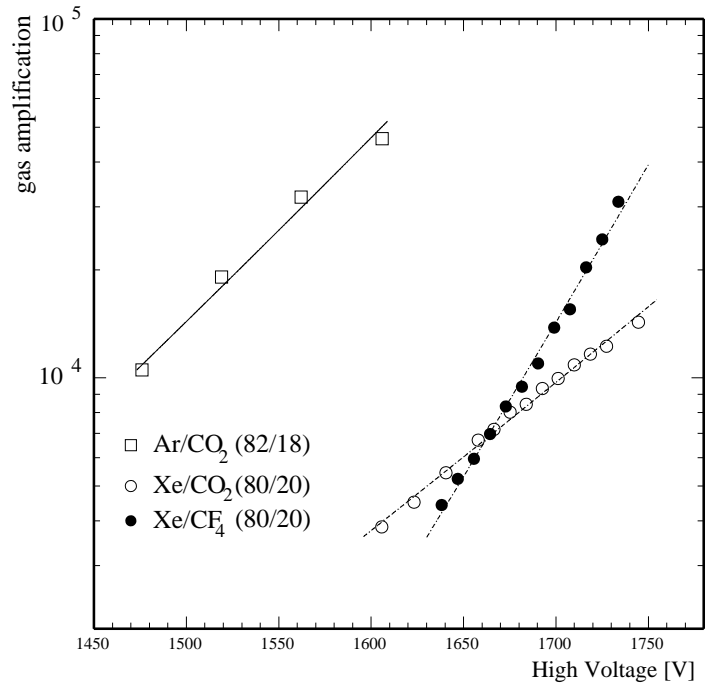


Figure 4.6: Gas gain distributions obtained with three different gas mixtures, using an ^{55}Fe radioactive source.

In the case of the measurement with the β -emitter, part of this reduction is compensated. The lower reduction lies in the fact that the primary particles suffer from a larger number of interactions with the detector gas, in the same way as described above, when the gas density increases. Thus the energy deposition rises and the number of liberated primary electrons increases. The gas gain distributions, as plotted in figure 4.7, show a behaviour according to the described expectations. Each of the plotted data points represents the averaged result from the 10 innermost straws, within the used module. As γ -emitter the ^{55}Fe and the ^{65}Zn sources have been used and the ^{90}Sr served as the β^- -emitter for these activities. As shown in the figure, formula 4.1 can be used, as a function of gas density ρ , to fit the γ series data. In case of the β data distribution, the gas gain values always lie well above the other two, and the attempt, to do a similar fit, fails. These results imply the theo-

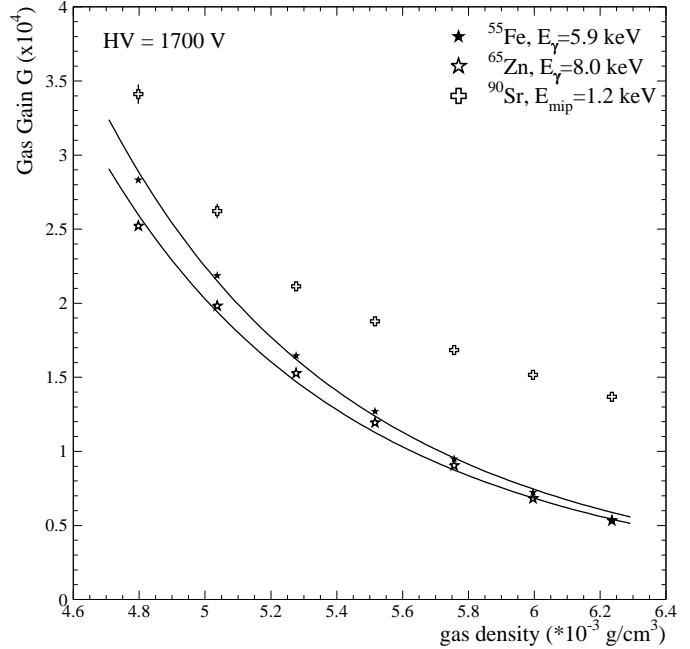


Figure 4.7: Gas gain as a function of gas density.

retical necessity for a separate gain correction of the dE/dx and the transition radiation part of the energy spectrum, as will be explained in detail in the following chapter. The problem for real taken data always is, though, that the dE/dx , from the traversing charged particle, and the energy deposit, from an absorbed TR photon, inside the same detector volume are added together before the signal is digitised by the ADC. This means that the two different energy depositions cannot be separately gas gain corrected, only the simulated data provide this opportunity. This gain correction will be addressed again in the next chapter on data analysis.

Gas Gain Measurements with various γ Energies This part of the laboratory activities was to investigate on the maximum photon energy, that can be fully detected in the 6 mm proportional tubes used for the AMS TRD. And to look for a potential space charge effect. As described in the previous chapter, the photons, absorbed in the proportional gas, are converted into photo-electrons. During this process, almost the full photon energy⁸ is transformed into the electron's kinetic energy, which is then dispersed inside the detector volume, via ionisation energy loss. However, this is only true for photon energies up to a certain maximum. For x-ray energies exceeding this maximum, the photo-electrons carry so much energy, that they can leave the detector volume and thus only deposit part of their energy inside the detector gas.

Space Charge Effect A second effect that can reduce the output signal height, above a certain energy threshold, is the so called "space charge" effect. Differential to the first named, the space charge effect is based on the shielding of the central electric field by the large number of secondary ions, produced in the avalanche.

⁸reduced by the binding energy of the shell electron

These positive ions form a space charge cloud that induces an electric field opposite to the one, originally applied. This effect reduces the net electric field, experienced by the electrons and ions. The avalanche is generated close to the wire and the corresponding electrons have a factor of ~ 1000 higher velocity and therefore reach the wire sooner, than the ions reach the straw wall. As a direct result they do not effectively contribute to the shielding. The weaker net electric field causes a decrease in the number of secondary electrons produced and, in the same way, the output signal height diminishes. The appearance of these effects in the prototype modules and their possible starting photon energy or number of secondary ions produced, respectively, was to be checked with this series of measurements. For that reason, the gas gain in Xe/CO_2 gas, was obtained from all above mentioned photon energies, and repeated for three different high voltages. In the case that there is neither of the two effects, the equivalent signal charge, $\frac{Q}{e}$, has to feature a linear behaviour when plotted against the photon energy, E_γ . Figure 4.8 plots the obtained equivalent signal charge, where again each data point represents the averaged result from the innermost 10 wires of the module. Each measurement is gas gain corrected to NTP⁹ conditions¹⁰.

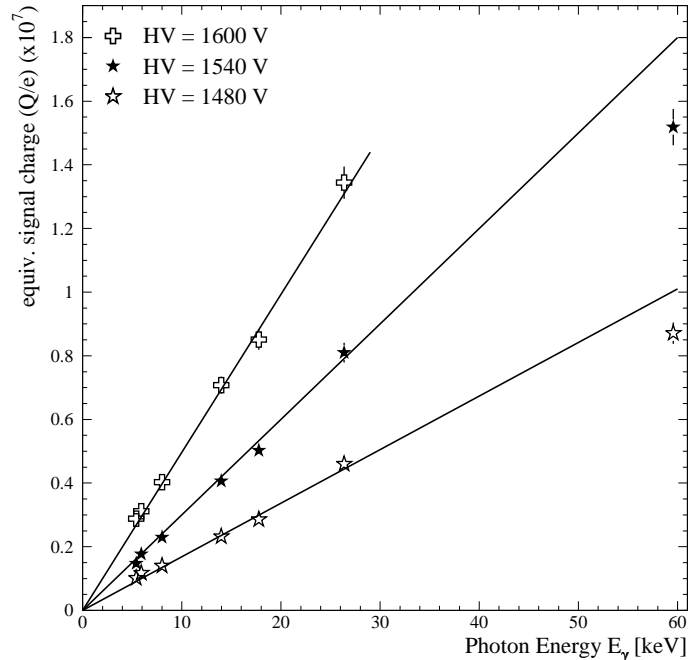


Figure 4.8: Gas gain as a function of E_γ .

Within the error bars, the displayed distributions show such a linear relation up to a photon energy of at least 26.4 keV . Only the two data points, referring to the 59.5 keV spectral line, are reduced by roughly 15 %, compared to the extended linearity, represented by the plotted straight lines. This implies a twofold information. First, at least one of the two effects seems to be present and second, this measurement outcome favours the incomplete energy deposition over the space charge effect. This is because, the space charge effect would grow bigger with an increasing gas gain factor, whilst the incomplete energy deposition percentally stays the same, for any high voltage applied. A second fact that rules out the space charge effect, is the appearance of the first deviation from the linear behaviour at an equivalent signal charge of 8.5×10^6 , within the first series. Contrary to that, the data point at 26.4 keV of the third series, equivalent to a signal charge of $\frac{Q}{e} = 13.5 \times 10^6$, still features a linear behaviour. Finally, this result lays bare a linear energy deposition up to energies of $35 - 40 \text{ keV}$, which makes no testbeam data correction necessary. The reason for that is the limitation of the maximum resolvable energy for all detector channels to below 40 keV by the used ADCs. This will become more clear, during the course of the next chapter.

⁹NTP: $T = 20 \text{ }^\circ\text{C}$, $p = 1013 \text{ mbar}$

¹⁰The third 59.5 keV data point is missing, because the signals exceeded the ADC range (overflow)

4.2 The 20-Layer Prototype

After the modules have been built and tested in the described way, they are integrated into the 20-layer prototype, which the reader will be introduced to, in the following section. But first, a brief explanatory statement on the Monte Carlo (MC) simulation studies that led to the chosen TRD parameter values, shall be given.

4.2.1 The TRD Parameter Choice

In the first place, the parameters to be chosen, were the diameter of the proportional tubes, the number of layers and the radiator thickness, which were to be optimised in MC studies. However, these parameters had to match several constraints for the overall TRD subsystem. First there is to name a technical reason, that fixed the choice on the proportional tube diameter to 6 *mm*. This choice, compared to the alternatively available 4 *mm* tubes, improves the inherent mechanical stability of the whole subsystem and reduces the number of readout channels and with that the weight of the TRD and its electrical power consumption. Secondly, the height has to be kept within 60 *cm* and the radiation length above the central tracker, should be as little as possible. As a result of that, the support framework was designed in a conical octagon shape, to provide mechanical stability and keep the support structure itself and any services, like electronics and gas supply, out of the central tracker acceptance.

Left over for optimisation remained the choice of the number of layers and the appropriate radiator thickness to have best TR performance within the 60 *cm* maximum height. In finding this optimum, the request of a large number of layers remains, which is necessary to gain tracking information from the TRD, above the central magnetic field. It is that wanted 3D-tracking information, that led to the two different module orientations inside the TRD. A second reason, for a large

number of layers is the electrical grouping of modules into towers of four. In the case that one of the modules fails, the high voltage for the entire tower has to be switched off. For a large number of layers a reduction by one tower affects the TR performance less. So it was part of the optimisation to find an ideal TR performance for the full TRD and still maintain the performance in the reduced layer case. The accomplished MC studies on these concerns were done with the extended GEANT 3.21 software, as briefly mentioned above and will be explained in detail in chapter 6. Preliminary studies were carried out with this GEANT3 software, optimised for the Hera-B TRD, that led to the prototype design.

No of Layers	Rad. Thickn. [<i>mm</i>]	TRD height [<i>cm</i>]	p+ Rej.
14	31	53.2	309
16	27	54.4	585
18	23	54.0	649
20	20	54.0	746
24	16	55.2	1163 [†]
30	12	57.0	1163 [‡]

Table 4.1: *Proton rejection as a function of number of layers and appropriate radiator thickness, derived for 100 GeV protons, referring to 90% e⁻ efficiency.*

[†]extrapolated from 20 layers interleaved with 16 *mm* radiator

[‡]extrapolated from 20 layers interleaved with 12 *mm* radiator

The deduced results have been approved in the scope of the MC studies that will be subject of chapter 6 of this thesis, where the full particulars on these MC simulations and optimisations will be presented. Only the mentioned approved results¹¹, as given in table 4.1, shall be anticipated here already. The reached decision is based on the proton rejection factor ($\frac{\text{total \#}p^+}{\text{selected \#}p^+}$) calculated as a function of the number of layers and the appropriate radiator thickness. The given rejection factors, derived from 100 GeV proton samples and referring to 90 % electron efficiency ($\frac{\text{accepted \#}e^-}{\text{total \#}e^-}$) favour a large number of layers with a thinner appropriate radiator layer. The proton rejection noticeably increases up to a value of 1163. That means the best performance, within the constraints, seems to be found with 24 layers covered by 16 mm radiator material. A further increased layer number leads to no improvement anymore. However, weight and electrical power consumption are very important issues for the AMS project. In the course of budgeting power and weight, it was figured out that the TRD cannot comprise more than 20 layers and the appendant radiator thickness. Based on these facts the configuration for the AMS TRD was chosen as described above. In such a TRD, a failure in one "4-module-tower" would reduce the proton rejection, in this detector segment, by roughly a factor of 3 down to a value of 259. This simulated scenario denotes the worst case, since the simulations were accomplished with perpendicular incident particles. With isotropic particle injection, as will be present during the measurements on board the ISS, particle trajectories on average do not strike all four dead layers of a possibly switched off tower.

4.2.2 Mechanical Layout

The overall layout of this prototype is very similar to that of the final TRD. It, alike, comprised 20 layers of straw modules covered with 20 mm radiator material. Each layer comprised 2 straw modules of 40 cm length, which were shifted against each other by half a layer thickness, as displayed in figure 4.9. Contrary to the final TRD layout, only the layers 3+4 and 17+18 were rotated by 90 degrees. This is due to an older layout version, applied to the construction of this prototype. All modules were held in a jig, made of aluminium, that served as the support framework for the modules themselves as well as the gas tubing and the electronics (readout boards and high voltage manifolds). The gas supply system was also attached to this jig. Inside the jig, the main number of modules were held in an upright position, whilst only the rotated ones were positioned horizontally. According to the outgoing beam axis definition (see fig. 4.10) the right hand side (upright) and upper half (seen in the lateral) of the prototype was referred to as the "P-Tower". The left hand side and lower half were called "N-Tower".

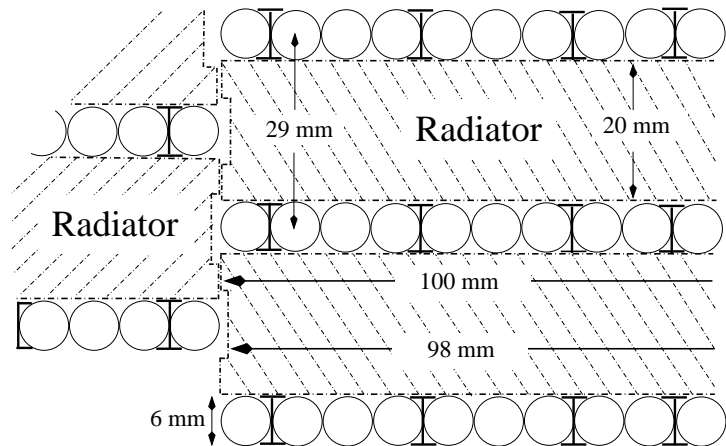


Figure 4.9: Zoom into the layer structure.

¹¹These results are based on the MC studies carried out for the prototype with only 20 mm radiator thickness. For that reason the layer variation was done relative to the prototype's height of 54 cm.

The upright modules of the P-Tower were integrated upside down into the jig. They had the gas supplied from the top and their electronics connected from the bottom. The prototype was mounted onto a turntable, provided with a degree scale, with which the prototype, as a whole, could have been rotated perpendicular to the beam axis. Beam inlet and outlet windows of $(20 \times 20) \text{ cm}^2$ area, were cut out of the front and back side of the jig. These windows were closed by 5 mm acrylic glass panes (not shown in the picture) corresponding to a similar amount of material in front of the detector, as the honeycomb plates of the final TRD. In front of these windows, trigger scintillation counters were placed, upheld by support bars, additionally attached to this jig (not shown).

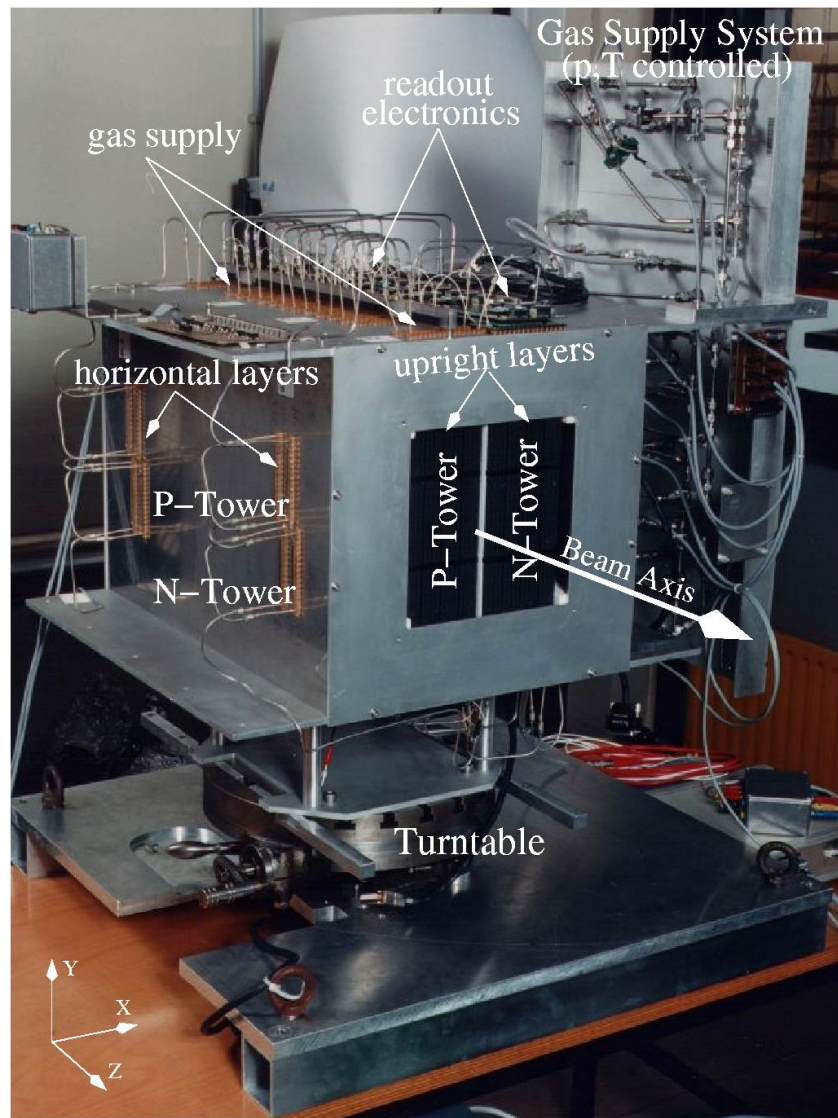


Figure 4.10: Photo of the 20-layer TRD prototype.

Radiator The "P-Tower" was used for final radiator tests. For that reason, the central 3 sets of 4 successive layers were equipped with a different radiator material, each. For the whole "N-Tower" the ATLAS fleece material, as described in the previous chapter, was used. This final radiator test arose from the outgassing rate of the fleece material, that exceeded the space qualification requirements by NASA. For that reason the ATLAS material had to be chemically cleaned, not knowing though, whether this cleaning affects the TR performance. As an alternative, a new radiator material was proposed, with an outgassing rate, known to be within the NASA limits, but with unknown TR performance. This newly proposed material, Separet 405, is made of Polyacryl and consists of similar fibers, with an average fiber diameter of $14 \mu\text{m}$ and an overall density of 0.08 g/cm^3 . The test results, which will be briefly presented in the next chapter (see page 66), show that the TR performance of the ATLAS fleece is not affected by the cleaning and that the polyacryl material, compared to this, has a reduced radiation yield.

Gas Supply System The 40 prototype modules were divided into groups of 6 or 8, to build a total of 6 gas chains. In the same way as for the final TRD, the gas was flushed sequentially through the modules of each gas chain, with a constant gas flux of 1.2 l/h . At that stage of the project, no recirculating gas system was available, so an open one had to be used, which gathered the gas at the end of each chain and "wasted" it through a bubbler out of the exhaust. The gas supply was controlled by flow-meters, solely for each chain, and the gas dispersed to each module through 3 mm aluminium tubing. The gas system was equipped with 7 pressure and two temperature sensors. One of the 7 sensors measured the absolute pressure inside the exhaust pipe close to the bubbler, whilst the remaining 6 monitored the differential pressure between the gas inlet and outlet of each gas chain. The temperature sensors were located inside the jig, attached to the aluminium walls, to measure the overall temperature inside the prototype.

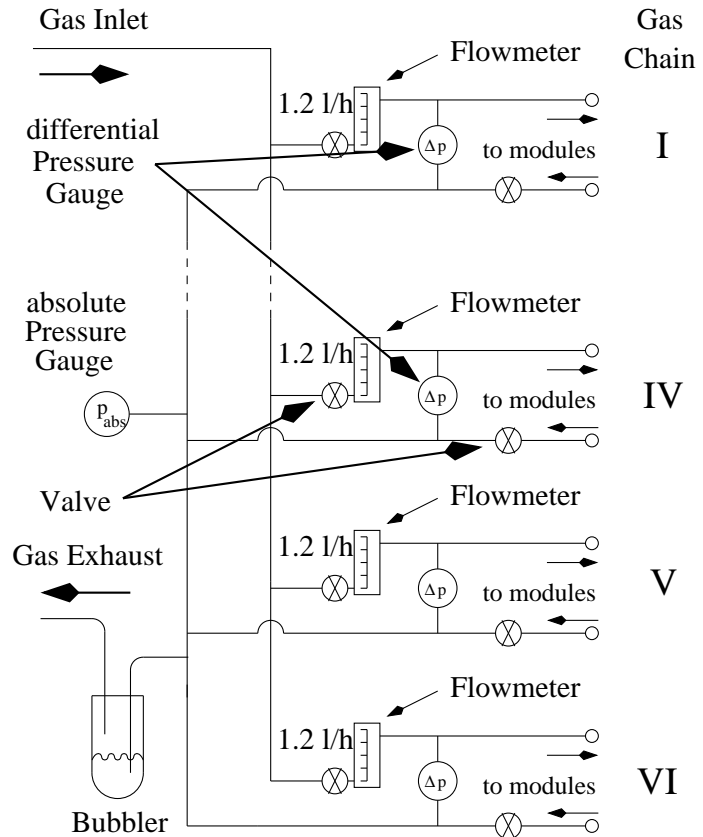


Figure 4.11: Principle of the prototype's gas supply system.

Electronics The only major difference in the prototype electronics compared to that of the final TRD, as explained in the previous chapter, lies in the digitalisation. For the prototype, 3 12bit ADCs were used, accommodated on a separated board, to which the analog signals from all VAs were serially transferred. Besides that the prototype electronics differed only in details from that, foreseen for the final TRD. The mechanical orientation of the tube endpiece board towards the straw module was perpendicular, compared to a parallel mounting now. The UFE equivalent was a board that accommodated 8 VA chips and organised the readout for all upright modules of one tower. In total, there were two of these boards, plus 2 smaller boards equipped with 3 VAs each, that governed the readout for all 8 horizontal modules and the used trigger scintillation and Čerenkov counters. The signals from these counters were integrated into this readout chain, using a handmade "attenuation" board to reduce the signal heights by roughly a factor of 100 for them to be suitable for a VA readout.

VA Linearity Off-the-shelf VA chips, VA32-HDR2, manufactured by IDEAS¹², were used. The VA chips had a dynamic range of about 1100 fC , at an ENC¹³ of 0.2 fC , and a peaking time of $2\text{ }\mu\text{s}$. These VAs featured a gain linearity, as figure 4.12a shows, up

¹²Integrated Detectors & Electronics AS

¹³equivalent noise charge

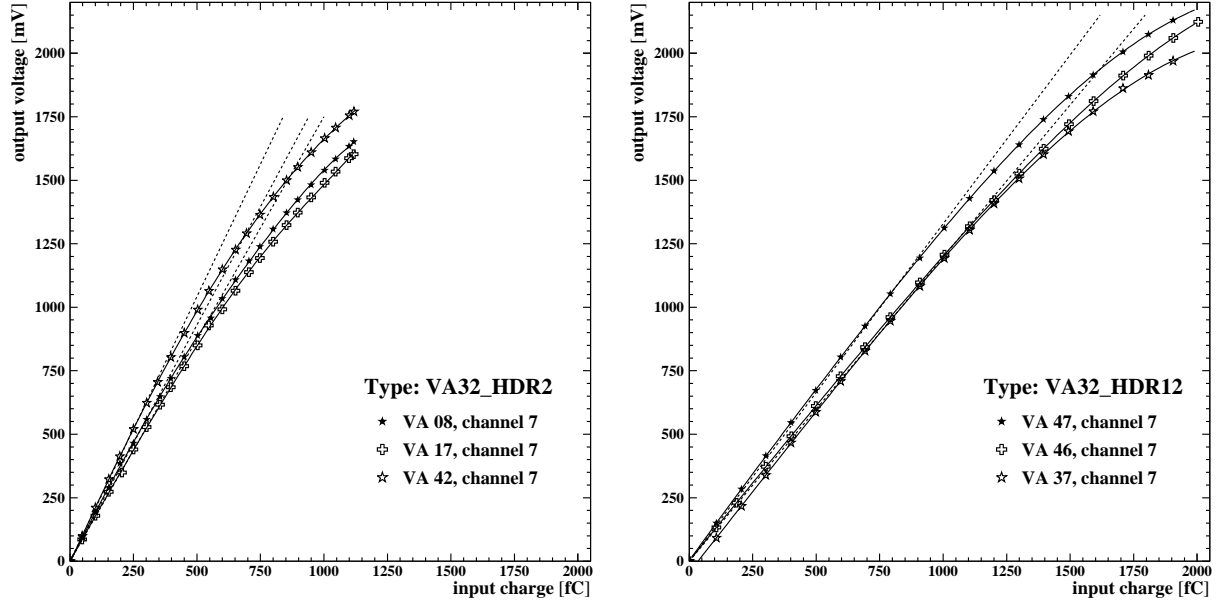


Figure 4.12: a) Gain linearity of the VA32_HDR2 chips, used for the prototype; b) Gain linearity of the VA32_HDR12 chips, proposed for the final TRD.

to equivalent signal charges of only ~ 450 fC, equivalent to an energy deposition of 5 keV or ~ 4 MIPs. The plotted gain distributions are used to correct the data, obtained during the test beams. The VA chips, VA32_HDR12, proposed for the final TRD, will be custom-made for the AMS collaboration and have an improved linearity as one of the revised features. The gain distributions of these final VAs, as exemplary illustrated in figure 4.12b for three different chips, show a linear behaviour up to equivalent signal charges of ~ 1100 fC. This means an improvement by roughly a factor of three, compared to the VAs used for the prototype. For that to be realised the VA amplification factor is reduced from ~ 1.8 down to ~ 1.3 . For further details on the electronics of the final TRD see the previous chapter and [46, 47].

4.3 Beamtests of the TRD Prototype

The such built and tested 20-layer prototype was then subjected to two high energy beamtest at CERN in summer 2000. These beamtests were accomplished at two beamlines of the Super Proton Synchrotron (SPS) at CERN. Namely, during a period of 12 days at the X7-beamline, and a period of 5 days at the H6-beamline. During the first beamtest e^- , μ^- , π^- and p^+ data, at energies ranging from 5 to 250 GeV, were taken. The H6 beamtest was used to confirm the proton data, using a CEDAR¹⁴, which guarantees a pure proton beam. An overview of the recorded data is given in table 4.2.

4.3.1 General Set-up

During these beamtests, the prototype was mounted onto an external moving table, with which it could be horizontally and vertically shifted, perpendicular to the beam axis. In such a way supplemented, the prototype was placed in the beamline, sandwiched in between two sets of plastic trigger scintillation counters, as figure 4.13 illustrates exemplary for the X7-beamtest. The inner pair of counters (S2,S3), are directly attached to the jig.

¹⁴Cerenkov Differential counter with Achromatic Ring focus

E_{beam}	X7				E_{beam}	X7	H6
[GeV]	$\#e^-$	$\#\mu^-$	$\#\pi^-$	$\#p^+$	[GeV]	$\#p^+$	$\#p^+$
5.0	120k				120.0	30k	215k
10.0	160k		20k		140.0	30k	
15.0				45k	160.0	40k	290k
20.0	150k		20k	30k	180.0	40k	
40.0	160k		20k	60k	200.0	80k	155k
60.0	180k	190k	20k	20k	250.0	65k	
80.0	120k	170k	20k	20k			
100.0	200k	110k	50k	150k			

Table 4.2: Event numbers recorded at various beam energies. Suffix "k" denotes $\times 1000$.

They were made such, that they cover the full width of one tower with total sizes of $(10 \times 15 \times 1) \text{ cm}^3$ and $(18 \times 10 \times 1) \text{ cm}^3$, respectively. They are mounted that way, that they can be shifted to a central position or either be placed in front of the N- or P-tower. A second pair (S1,S4), with sizes of $(30 \times 30 \times 2) \text{ cm}^3$, was placed at a distance of roughly 2 m in front and behind the jig. Additionally, the beamlines were equipped with two threshold Čerenkov counters, in the X7 case, and a differential one, integrated into the H6-beamline. During the X7-beamtest, a fifth scintillation counter (S5), of the same size than the outer pair (S1,S4), was placed behind a 2 m long beam dump, made of concrete and steel. This fifth counter was used to trigger on, or reject, μ^- particles.

Trigger logic The trigger logic foresees a commonly used sequence of coincidences, as is illustrated in figure 4.13. The two Čerenkov counters in beamline X7 were used only for the proton runs, rejecting all particles but protons. So in any case of a signal from only one of these counters, the trigger was discarded. The H6 test beam benefited from a differential Čerenkov counter, which provided the opportunity to directly trigger on protons. This somewhat simplified the trigger logic. Secondly, the usage of, in total, three integrated "deadtimes", need to be explained. The first downtime, in the diagram referred to as "Silence", was to guarantee that no particle traversed the set-up during a time period of 100 μs before the trigger, to avoid pile-up¹⁵. Both other deadtimes were referring to the 10 ms time consumed to read out all 640 readout channels. On the one hand, the readout board itself provided a "busy" signal, which, however, took on the order of 1 μs to be produced. During this 1 μs time gap, a second trigger could have been generated, that would have caused a distorted recording of the first accepted event. In order to prevent such distortion, an inhibit signal of 10 ms length, was produced from the final trigger within nanoseconds. This inhibit signal was sent back into the trigger logic, to "destroy" any possible further trigger. For these "deadtimes" gate generators were used, that can be retrigged from any second signal, arriving during the open gate.

¹⁵The full signal length, including the overshoot, from the used proportional tubes is roughly 100 μs .

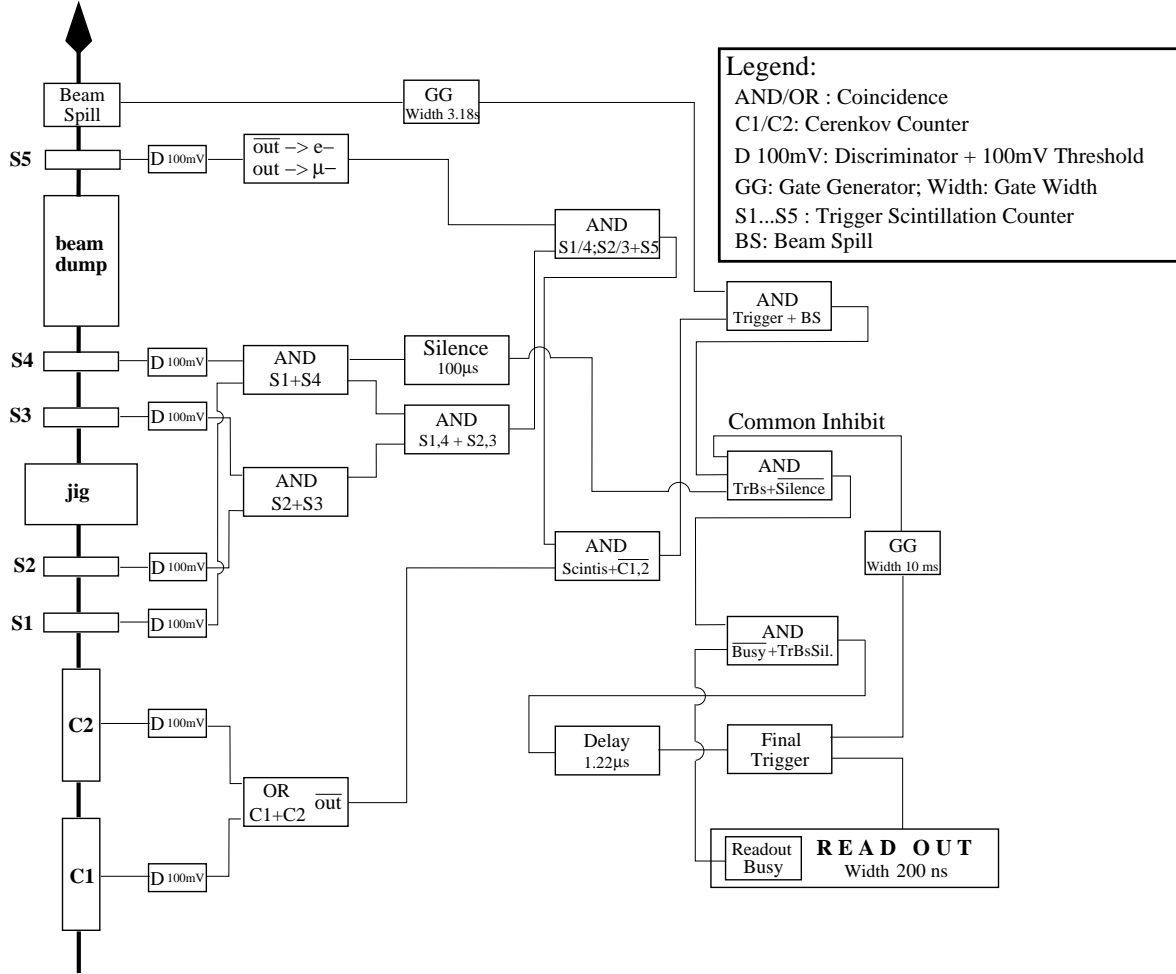


Figure 4.13: General beamtest set-up and trigger logic, as used for the X7-beamtest.

Primary protons of momentum up to 450 GeV/c are slow-extracted from the CERN SPS to two experimental zones, the North Area in Prévessin (France), where the H6-beamline is accommodated, and the West Area test beam complex on the Meyrin site which the X7-beamline is part of.

4.3.2 The X7-Beamline

The X7 beam is a secondary or tertiary particle beam that provides hadrons, electrons and muons of energies between 5 and 250 GeV. The X7 beam is produced with SPS protons directed onto primary, secondary and eventually tertiary targets, which produces various kinds of particles. In either case, particle beams with a precisely defined momentum (intrinsic momentum resolution of $\Delta p/p = \pm 0.8\%$) can be generated, using deflection and focusing magnets as well as a set of collimators. A detailed description of the beam characteristics can be found in reference [56]. For means of particle identification the beamline is equipped with two threshold Čerenkov counters, filled with He and N₂ gas, respectively. As briefly mentioned above, these counters have been operated to indirectly trigger on protons. That means, the pressures of both devices have been chosen such, that all particles but protons produce Čerenkov light, inside the detector gas. The problem with this method is, that the ID uncertainty relies very much on the efficiencies of the single photomultipliers (PMs) per counter, that read out the produced Čerenkov light.

Any such PM inefficiency causes a contamination of the proton data samples with lighter particles, and thus worsens the experimentally derived TR rejection power. For the pressures to be chosen right, the particle identification efficiency as a function of gas pressure is measured. This is done exemplary for both detectors at +15 GeV beam energy, to check the threshold pressure settings, provided for every available particle energy by CERN personnel.

The measured distributions for both counters are plotted in figure 4.14. Both distributions show a reasonable agreement between the pressure thresholds, obtained from the measured distributions, and those provided. For that reason, the pressures in both detectors have been chosen according to the given threshold values, during all proton measurements. It remains worth mentioning that the gap between the plotted distributions and the 100 % detector efficiency is caused by the $\sim 10\%$ proton contribution to the beam. According to this pressure curve the pressures were chosen to 3.0 bar for both counters. A second pressure curve measured with a pure pion beam resulted in inefficiencies for the two counters of 2.5 % (C1) and 4.6 % (C2) at the maximum gas pressure of 3 bars inside the detectors. That leads to a possible detection inefficiency, combining the two counters, of 1.15 %. Table 4.3 contains the chosen pressure settings for all used beam energies.

4.3.3 The H6-beamline

The H6-beamline can provide energies ranging from 5 to 205 GeV/c, while being operated as secondary or tertiary beam. During the prototype test beam it was solely used as secondary beam with three different proton energies (see table 4.2), only. The momentum resolution for this beamline is $\Delta p/p = \pm 0.3\%$, governed by

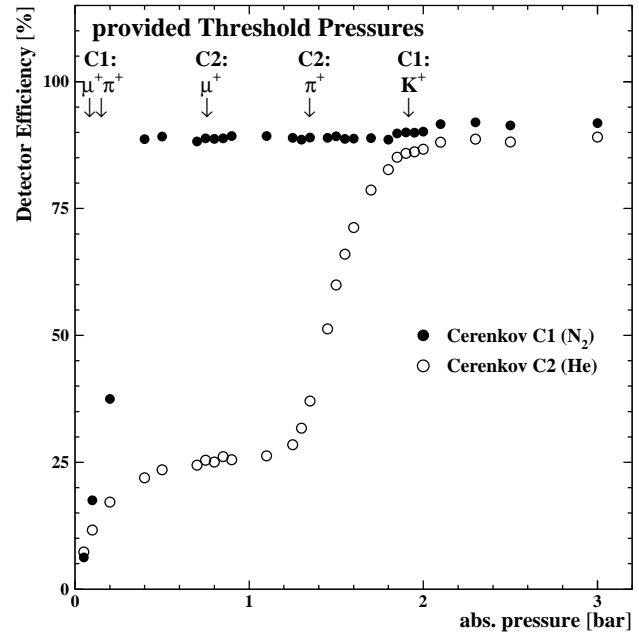


Figure 4.14: Threshold Čerenkov detector efficiencies as functions of gas pressure, for the two counters, filled with He or N₂ gas, respectively, obtained for $E_{beam} = +15$ GeV.

E_{beam}	threshold Čerenkov counters (X7)	
[GeV]	C1 press. [bar]	C2 press. [bar]
20.0	3.0	3.0
40.0	1.0	3.0
60.0	0.48	2.50
80.0	0.32	2.35
100.0	0.22	1.50
120.0	0.14	1.10
140.0	0.17	0.90
160.0	0.17	0.90
180.0	0.15	0.80
200.0	0.15	0.70
250.0	0.14	0.60

Table 4.3: Threshold Čerenkov counter settings dependent on the beam energy E_{beam} for the X7 beamtests.

two sets of collimators. For a detailed description of the beam characteristics, one may refer to [57]. For means of particle identification, the beamline was equipped with a differential Čerenkov counter (CEDAR), providing the opportunity to trigger on protons directly. That drastically reduced the uncertainty on the contamination of the proton data samples with lighter particles, as present in the X7 case. Inside such a CEDAR, particles generate Čerenkov light at the "front side" of the detector, expanding as a light cone into the gas volume. The opening angle of each cone depends on the particle velocity. The light is detected in the form of a ring by a set of 8 photomultipliers (PMs), arranged in a circle. The trigger signal can be generated from a 6fold, 7fold or 8fold coincidence from the single PM signals. To separate between particles of different types, part of these rings can be blinded out by an iris. The possible radial openings of this iris range from 0 to 20 mm with an accuracy in the diameter of 10 μm . The CEDAR efficiency to detect a specific particle type, depends on this iris opening, and the gas pressure inside the counter [58].

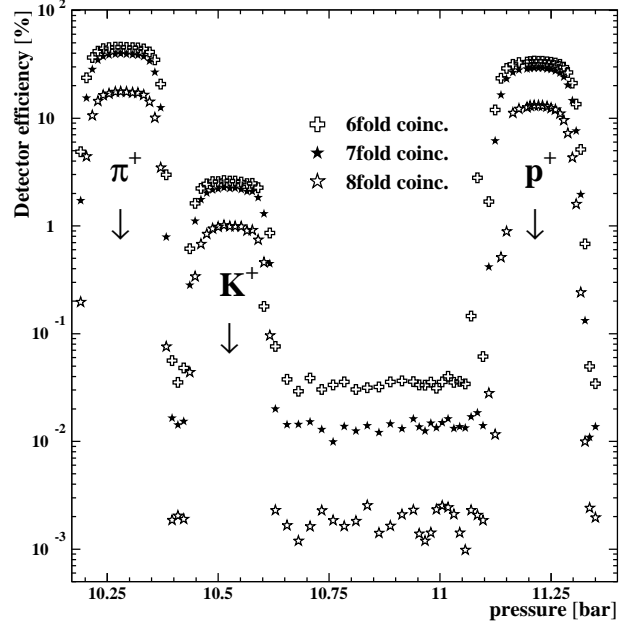


Figure 4.15: CEDAR efficiency as a function of gas pressure. The 6fold, 7fold and 8fold coincidence distributions are plotted for 120 GeV p^+ energy, and an iris opening of 1 mm.

The right CEDAR operating values to trigger on protons was found by measuring the counter efficiency as a function of gas pressure. This procedure was carried out for the three beam energies used and repeated for different iris openings. Figure 4.15 compares the pressure curves taken with 6fold, 7fold and 8fold PM signal coincidences, a beam energy of 120 GeV and a 1 mm iris opening. All three displayed pressure curves

depict three well disjoined pressure regions, where the detection efficiency is drastically increased. The first two regions can be identified as those, where pions and kaons, respectively, generate a predominant fraction of their Čerenkov light rings, inside the iris opening. At a pressure, about 0.5 bar above the second region, a third high efficiency region can be seen, which is due to signals from protons. The difference of the three curves lies in the absolute efficiencies, where, in any case, the 6fold coincidence has the best efficiency, and the 8fold the highest identification power. The chosen parameter values for this 120 GeV beam, were a pressure of 11.21 bar, an iris opening of 1 mm and the 8fold coincidence. Table 4.4 contains the CEDAR settings used for the H6 beamtest.

E_{beam}	differential Čerenkov Counter (H6)	
[GeV]	pressure	rad. iris opening
120.0	11.21 bar	1.0 mm
160.0	10.79 bar	1.2 mm
200.0	10.63 bar	0.58 mm

Table 4.4: CEDAR settings applied for the 3 beam energies E_{beam} of the H6 beamtests.

The chosen parameter values for this 120 GeV beam, were a pressure of 11.21 bar, an iris opening of 1 mm and the 8fold coincidence. Table 4.4 contains the CEDAR settings used for the H6 beamtest.

The main subject of this thesis is the analysis of the data, taken during these both beamtests, and to reproduce the measured results in Monte Carlo simulations. The following two chapters will circumstantially deal with this analysis and all the concerns of the MC simulation studies, respectively.

Chapter 5

Data Analysis

The intention to build the prototype and subject it to high energy beamtests at CERN, was to check whether the chosen TRD design suits the demands on its particle identification power. That is why the analysis, to be described below, is mainly focused on the determination of this identification power as a function of particle energy. However, some further aspects were to be investigated about. There are to name, for example, the final radiator test, as briefly addressed in chapter 4, and the effect on the gas gain from the in-chain gas operation of straw modules. The tube-to-tube inter-calibration was derived from the recorded muon runs and to energy calibrate the prototype, ^{55}Fe measurements have been taken throughout the X7 and H6 beamtests. After inter- and energy calibration a linear fit is performed for each event to reconstruct the particle track. Based on this straight line fit, several cut variables are defined to select straight, single track events. Energy spectra are accumulated from all tubes that the fitted track intersects and the e^-/p^+ -separation power is derived from counting the hits above a certain energy threshold. As an improved, second stage, the likelihood is calculated using the normalised full energy spectra for protons and electrons as probability distributions. The resulting proton rejection factors from this likelihood method, referring to 90 % electron efficiency, do not fall below a value of (143 ± 12) up to 250 GeV proton energy, which is well above the lower limit of 100, required for precision positron spectroscopy.

5.1 Data Preparation

As a preparation for the proton rejection analysis, the raw data have to be corrected channel by channel, for interfering effects, like the pedestal position and the common baseline shift for all detector channels, referred to as common mode. Furthermore, permanent differences in the gas amplification, due to finite mechanical accuracy (e.g. wire displacement, shape deformation) and VA gain variations and non-linearities, as mentioned in the previous chapter, need to be corrected for. The VA gain correction is accounted for as part of the inter-calibration, and the VA non-linearity is corrected according to the VA gain distributions, as shown in figure 4.12 and discussed in chapter 4 (see page 53). In addition, the data have to be adjusted to a common gas density, to compensate for environmental changes in temperature and pressure, leading to a changed gas amplification. The absolute energy calibration of the prototype is derived from the taken ^{55}Fe measurements.

5.1.1 Track Reconstruction and Event Selection

Pedestals and Common Mode Correction

As the first preparation step, the data are corrected for the pedestal position. In order to do so, the pedestal positions and widths are calculated from each data sample itself. The resulting pedestals range from roughly 800 to 1400 ADC channels with a mean at 1050 channels. With respect to the used 12bit ADC, with a total of 4096 channels, this default pedestal setting reduces the ADC's dynamic range by roughly 25 %. Regarding this, the default mean pedestal positions of the VAs, foreseen for the final TRD, are set to an equivalent of ~ 500 ADC channels.

The determined pedestal widths, as plotted in figure 5.1 for all 640 prototype readout channels, range from 2 to 6 ADC channels. Thereby noticeable is that, in principle, pedestal widths as low as 2.5 ADC channels¹, are possible with such a setup. However, this is true only for the readout of the vertical P-tower modules, whereas the pedestal widths are increased for both other readout chains², due to pick-up noise. On the one hand, the vertical P-tower layers were read out by that board attached to the bottom of the jig, which provided a better electrical shielding of the readout electronics by the jig's aluminium casing. On the other hand, the broader pedestals from the N-tower layers probably originate from badly isolated cables used to transfer the analog signals to the digitalisation board and a timing problem for the multiplexed readout of those 8 VAs recording the signals from this vertical N-tower. Whereas a different board design, and the direct exposure of the electronics to the particle beam, give the reason for the higher ENC of the horizontal layers. The data are already corrected for common mode during the data taking itself, by the VAs' built-in common mode correction. An off-line check has confirmed that this correction has been working as expected.

Linear Regression As the first selection criteria, a straight line fit is performed for each event. This is done separately for the vertical (Y-) and horizontal (X-) layers, using a double linear regression. In a first step, every single tube with an energy deposition above 3 pedestal widths plus 50 ADC channels, in the following referred to as "hit", weighted by the maximum distance of hits in one layer, is used for the first linear regression. With respect to this first line fit, the residuals are calculated for each of the hits in the event. For the second linear regression only those 6 (X-direction) and 15 (Y-direction) hits with the smallest residuals are used. The principle of the particle track reconstruction is illustrated in figure 5.2, in which the hits on the primary track are coloured black and red, depending on their energy. This reconstructed track and the definition of the "outer road", a corridor of ± 3 tube diameters around the track (green coloured tubes), serve as the basis for the event selection.

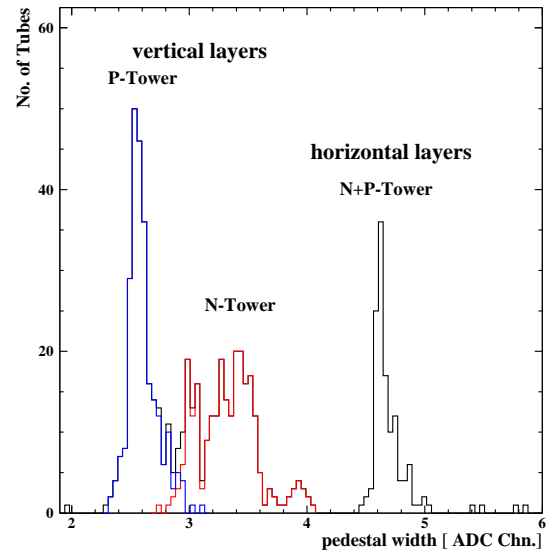


Figure 5.1: Pedestal width distribution for all 640 channels.

¹equal to an equivalent noise charge (ENC) of 0.5 fC

²vertical N-tower and N+P horizontal layers

Event Selection In principle, there are three types of events. First, and most important for this analysis, there are to name those events with only one straight, single track inside the detector. The entire analysis is solely based on such single track events. Events comprising multiple or secondary tracks need to be excluded. Mainly, multiple track events emerge from primary particle interactions with the material in front of the detector, like the plastic scintillators. Whilst secondary tracks, in figure 5.2 referred to as "Off-Track Hits", split up from the main track due to interactions, and with that secondary particle production, inside the prototype itself.

In order to sort out these latter two types of events, further selection criteria are applied to all those events, where the linear regression successfully reconstructed a single track. According to this track and outer road definition, several cut parameters are defined, as specified in table 5.1. The given limit values are optimised from proton rejection variations (see page 71). Two of the cuts need special explanation. On the one hand there is to name the "xspan" cut, which is introduced to guarantee a reasonable track

reconstruction for the X-layers. This is the case only when the track is reconstructed from hits in the front (3,4) and back (17,18) horizontal layers. The minimum case in here is a, from wire to wire, "X-hit-Z-distance"³ of 14 tube diameters. On the other hand, there is to mention the cuts on the Čerenkov counter spectra, which are used only for the proton data analysis. Due to the threshold settings of the counters, generating signals for all particles lighter than protons, these two cuts guarantee only proton events in each sample, to be analysed. Using these cuts the original sample sizes are reduced by 25-40 %, depending on the beam energy. The same cuts, applied to Monte Carlo generated samples, select ~80 % of proton and electron events as "single track". Details about this selection cut efficiency can be found in chapter 6 on MC simulations (page 94).

[†]hits above 6.5 keV

³min. case: 1 hit in lay.4 and 17 \rightarrow (17-4)+1 = 14.

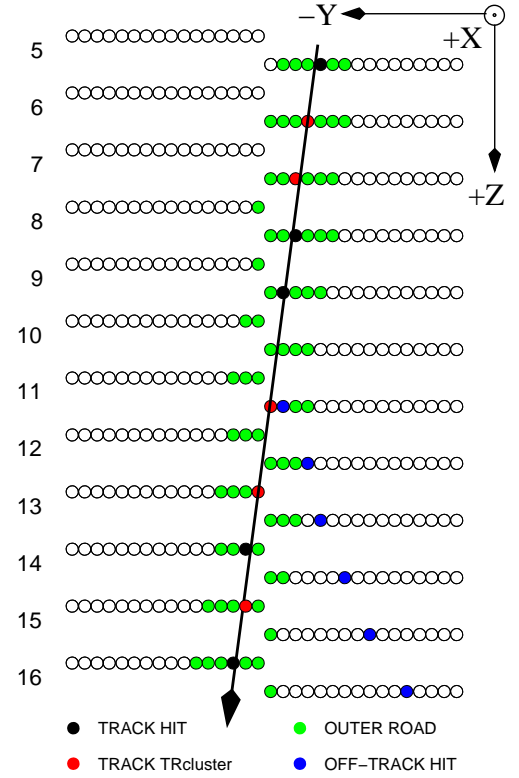


Figure 5.2: Principle of the track reconstruction in the vertical layers.

Cut Parameter	limit
No. of hits on XY-track	≥ 15
No. of hits on "outer road"	≤ 4
No. of hits off "outer road"	≤ 4
No. of "TR clusters" [†] off the track	≤ 1
No. of layers with more than one hit	≤ 5
$(E_{onTr.})/(E_{tot})$ [%]	≥ 75
No. of Y-layers with hit on track	≥ 12
min. Z-dist. of X-hits o.Tr. ("xspan")	≥ 14
Čerenkov counters with no signal [ADC ch.]	≤ 500
	≤ 250

Table 5.1: Cut parameters to select single track events.

Table 5.1: Cut parameters to select single track events. Details about this selection cut efficiency can be found in chapter 6 on MC simulations (page 94).

5.1.2 Channel-by-Channel Inter-Calibration

Single Tube Spectra The channel-by-channel inter-calibration is used to correct the data for tube to tube differences in the average signal heights. These differences find their origin in various mechanical and electrical aspects of the prototype, like the different VA pre-amplification and gas gain factors, for each channel. The finite mechanical accuracy in the module production, for example, causes permanent subtle differences in the gas gain factor, from tube to tube (also see page 32). In order to be independent from the proton and electron data, used in the proton rejection analysis (see section 5.3), the inter-calibration is done using the muon data runs.

Each available muon data sample is corrected and single track events are chosen, in the described way. For each run and readout channel, histograms of the signal heights, from hits on the track, are filled. One of the arising single tube spectra⁴ is shown in figure 5.3, together with its pedestal, shifted to zero ADC bins.

The Moyal parameterisation [59] for the Landau distribution is used to determine the most probable (MOP) values of these spectra⁵, in the following referred to as Landau fit.

Inter-Calibration Table From these determined MOP positions, the inter-calibration factor for each readout channel is derived as the ratio of the single tube spectrum's MOP position and the weighted average⁶ from all spectra. The such obtained inter-calibration tables, from single runs, stay incomplete, because in each measurement data were taken only in part of the modules, either in the full N- or P-tower or in a central position between the two. For that reason, this procedure had to be repeated for all available runs and, in a first step, the obtained inter-calibration values are averaged, separately, for all N-, P-tower and central runs. In a final step these three tables are combined, after being leveled out to the same average, making use of the overlapping tubes. The final inter-calibration table is displayed in figure 5.4a. To inter-calibrate the detector, the energy deposition from each readout channel has to be divided by the appropriate number from this table.

At first sight noticeable is that still part of the readout channels (white areas) remain without inter-calibration factor. Especially for the horizontal layers (3,4 and 17,18) of the N-tower and layer 19 of the P-tower the inter-calibration factors are set to zero. This is because no muon samples from the horizontal N-tower have been taken. During the whole two beamtests, in general, only very few runs were taken, using these horizontal N-tower layers. As for layer 19, the high voltage supply had to be cut due to a front end electronics failure. This module couldn't be used throughout both beamtests. The proton background analysis, to be described below, for that reason disregards all runs with the beam traversing these parts of the detector.

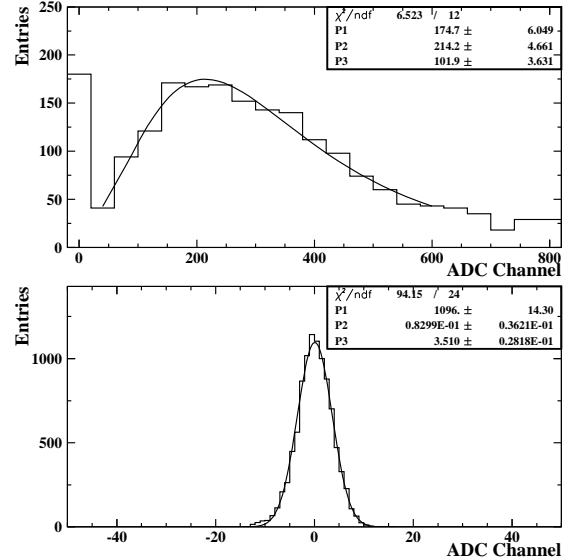


Figure 5.3: a) Landau fit to a single tube spectrum; b) Pedestal position after correction.

⁴it is rebinned as a matter of the small statistics

⁵ those having at least 50 entries

⁶weighted by the fit error

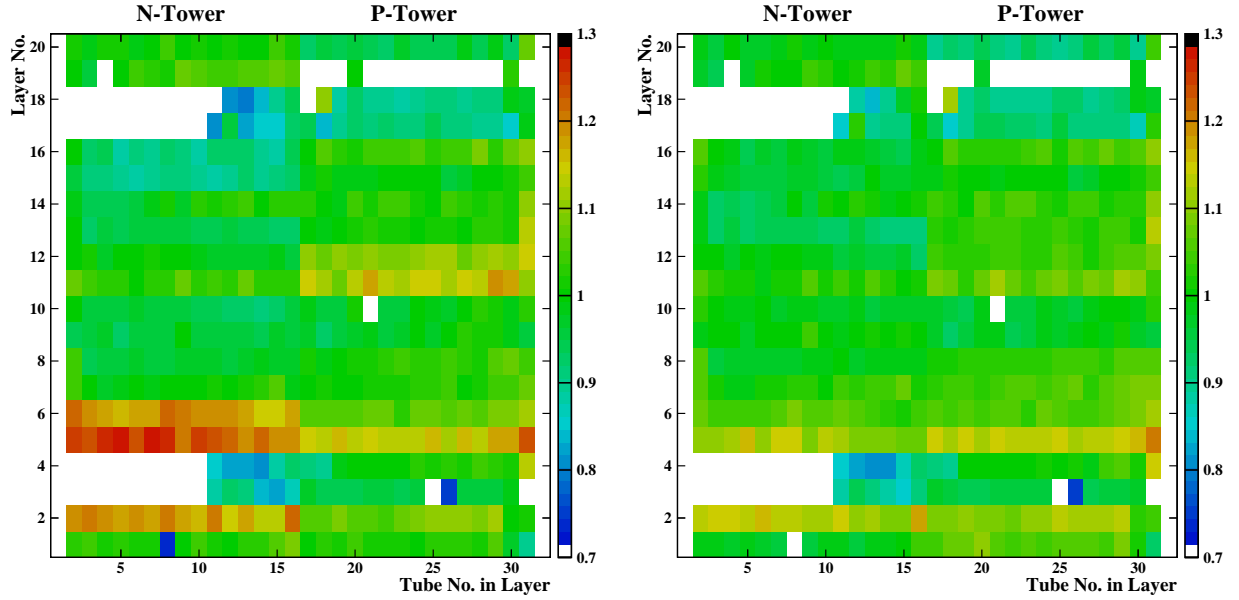


Figure 5.4: a) *Inter-Calibration table from muon runs*; b) *VA gains corrected*.

Besides that, some regions of the table attract attention, where extremely high or low values gather, like in layers 5,6 of the N-tower. This is mainly dominated by the higher mean pre-amplification factor of the specific VA, reading out these two modules. Figure 5.4b shows the same inter-calibration table corrected for the differences in VA gain, which narrows the values closer to "1". A closer look at this second table reveals decreasing inter-calibration factors, as a result from a reduced gas amplification, from the first module in each gas chain to the last (e.g. see layers 5 upto 10 of the P-tower). Contrary to an expected slight increase in the mean inter-calibration factors⁷, a detailed analysis results in a reduction by $(10.7 \pm 1.8)\%$ from the first module in each chain down to the sixth module⁸. This decrease is thought to be a result of an oxygen contamination inside the proportional gas, caused by gas leaks either in the chamber bodies themselves or the tubing and connectors, joining the modules together. Oxygen is well known to bind electrons due to its high electro-negativity, and in that way to reduce the gas amplification.

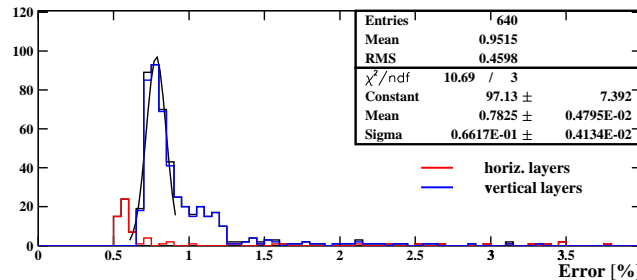


Figure 5.5: *Errors on the inter-calibration factors*.

Inter-calibration Accuracy The errors on the Landau fits, used to determine the MOP values of every single tube spectrum, are a meaningful measure for the accuracy of the derived inter-calibration table. As can be seen from figure 5.5, these errors mainly keep within the 1 % level, for the horizontal and the vertical layers. The reason for those few channels with larger fit errors lies in the smaller statistics for the appropriate spectra.

⁷as a result from a decrease in gas density

⁸including modules 7+8 of gas chains 1+6 changes this to $(11.4 \pm 3.2)\%$

5.1.3 Gas Gain Correction

The measurements in both beamtest have been taken over a period of several days and with that at changing temperatures and pressures. In order to correct the measured data for the accompanied differences in gas gain, the weighted MOP average is calculated for each inter-calibrated muon run. The derived values are then plotted, as the relative change of the average gas gain, versus the appropriate gas density, normalised to the mean gas density $\rho_0 = 4.46 \times 10^{-3} \frac{g}{cm^3}$. Figure 5.6 shows the evaluated distribution, to which a straight line is fitted. Using the slope, derived from this fit, the gas gain correction factor, $ggcf$, for each run, can be calculated from the associated density, according to the formula:

$$ggfc = 1. + \left[\left(\frac{\rho}{\rho_0} - 1 \right) * |slope| \right] \quad (5.1)$$

where the expression $|slope|$ refers to the modulus of "P2" from the displayed straight line fit. Increasing the gas density by 1%, leads, according to this fit result, to a decrease in the gas amplification by 5.24 %. The Gaussian distribution of the fit's residuals, as additionally shown in figure 5.6, has a relative width of 1.5 %. This width gives an error estimate for the derived correction factor.

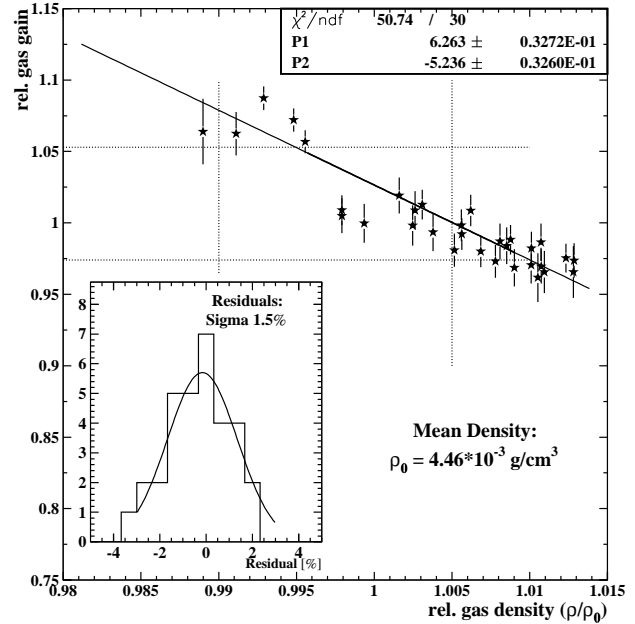


Figure 5.6: *The relative change of the average gas gain factor, derived from MOP position of muon spectra, as a function of rel. gas density. A straight line is fitted to the distribution.*

5.1.4 Energy Calibration

The final data preparation step is the detector's energy calibration. For that reason, ^{55}Fe spectra were measured in the layers⁹ 1 and 20, for both N- and P-tower, throughout both beamtests. As a significant difference to the γ spectra, presented in last chapter (see fig. 4.4), these γ measurements were taken with a random trigger. This is because, the used VA readout did not provide a self-triggered mode, as used for all laboratory measurements. Spectra taken with such a random trigger, as displayed in figure 5.7a, do not feature a clearly identifiable photo-peak, but a continuum in the range below the nominal photon energy. The energy calibration factor, in this case, is derived from the spectrum by fitting a Fermi function, as additionally shown in 5.7a, to its upper edge. It can be shown, that the dedicated photo-peak position can be calculated from the obtained fit parameters [60]. Inter-calibrated, the error weighted, average peak position from every run is determined. In the same way as before, the gas gain, calculated from each average peak position, is plotted as a function of gas density. A straight line fit to this distribution, as displayed in figure 5.7b, results in a slope of -5.76 % per percent change in gas density.

⁹restricted by the range of the photons inside the detector

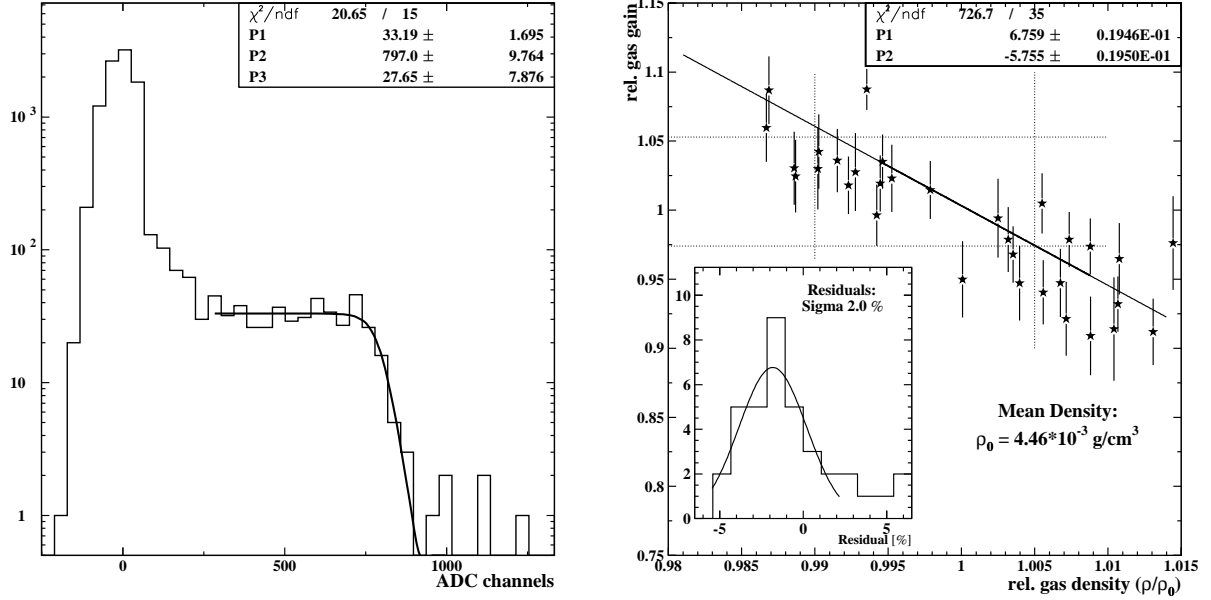


Figure 5.7: a) ^{55}Fe spectrum recorded with a random trigger. The Fermi function is fitted to the upper edge to determine the photo-peak position [60]; b) Average gas gain value, derived from ^{55}Fe spectra, as a function of gas density. A straight line fit is performed.

This greater slope, compared to that derived from the muon runs, can be explained by the different gas gain dependence on the gas density of ionisation energy loss and photon absorption, as described in the previous chapter (see page 47). Using this determined slope in equation 5.1, the average peak positions from all ^{55}Fe runs are gas gain corrected. The overall energy calibration factor, "ecf", is then derived to

$$(649.4 \pm 3.4) \text{ ADCbins} \hat{=} 5.9 \text{ keV} \quad (5.2)$$

$$\Rightarrow \text{ecf} = (9.09 \pm 0.05) \text{ eV/ADCbin}$$

from a Gaussian fit to the distribution of these peak positions, as displayed in figure 5.8. A reasonable measure for the error on this energy calibration factor seems to be the uncertainty in the peak value from the fit.

The such derived corrections and calibration factors are applied to proton runs at all available energies. Solely for every beam energy, histograms are filled from every energy deposition on the track of all selected, single track events, and the MOP values are determined from a Landau fit. Figure 5.9a shows the energy spectrum, for 100 GeV protons. The displayed spectrum features the typical characteristics of a Landau distributions, with a MOP value at 1.49 keV and an exponential declension to higher energies. The superlevation above 20 keV, and the sudden cut-off above 30 keV, is a result of the ADC's limited dynamic range, smeared by the changing pedestal positions of the different readout channels.

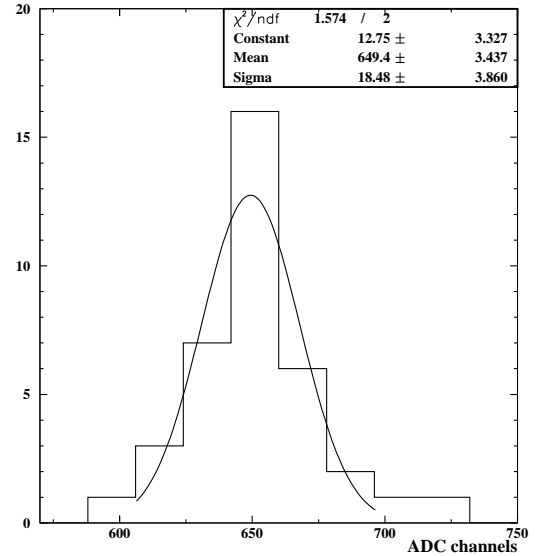


Figure 5.8: Gaussian distribution of energy calibration factors, derived from ^{55}Fe measurements, taken throughout the X7 beamtest.

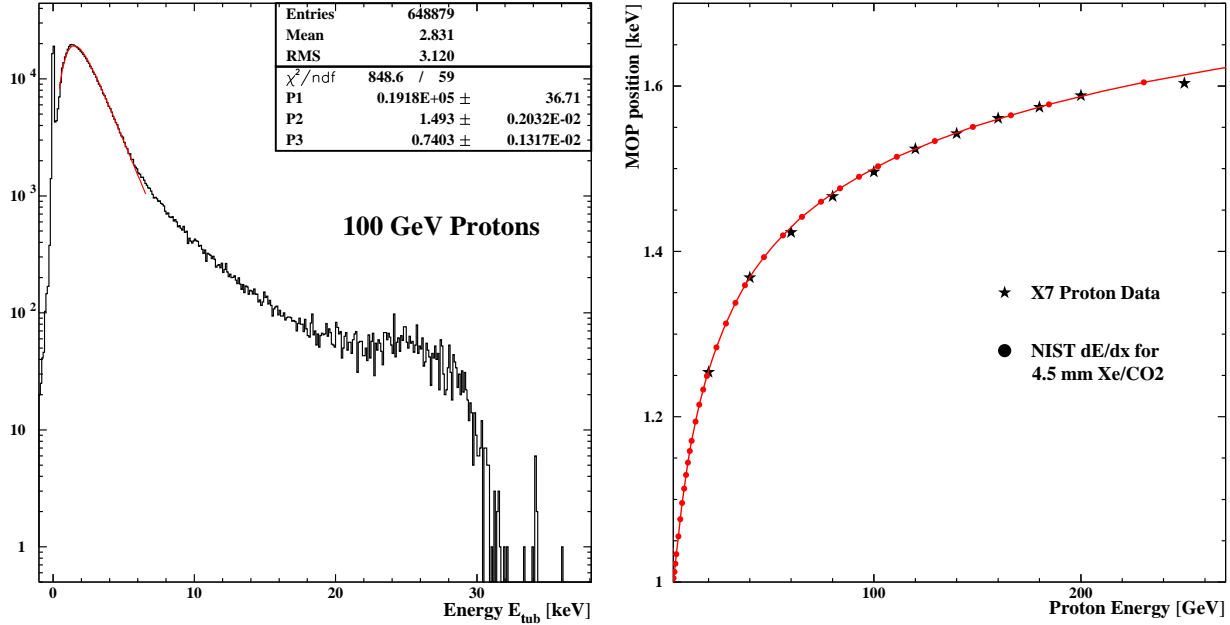


Figure 5.9: a) 100 GeV proton spectrum, containing the hits on the track of all selected single track events, measured during the X7 beamtest; b) Spectra's MOP position as a function of particle energy, compared to a calculated distribution from NIST.

The fitted MOP values, plotted as a function of beam energy, show the typical relativistic rise, as figure 5.9b illustrates. This figure, as well, displays a good agreement between the data distribution and one provided by the "National Institute of Standards and Technology (NIST)". This second distribution is calculated from theoretical predictions and empirically derived corrections at standard conditions¹⁰ [37]. For the displayed match between data and NIST predictions, the latter are adjusted to the appropriate average Xe/CO_2 gas density and the particle's varying track-lengths with an average of 4.5 mm inside the detector tubes. The track-length variation is a result of the detector tubes' circular cross section. Besides the mentioned corrections, the predicted distribution had to be scaled by a factor of 0.9. This scale factor can be justified by taking into account the higher statistical fluctuations of the ionisation energy loss within short track lengths in low density gases as used during the beamtests. Whereas the NIST distribution is calculated for track-lengths of several centimeters inside the detection gas, where the statistical fluctuation balance out.

5.2 Radiator Test

In the same way as for the protons, electron spectra from single track events are accumulated, after the data being corrected and calibrated. One such energy spectrum is shown in figure 5.10a. In this spectrum, the effect of transition radiation(TR) is clearly visible. Compared to the discussed proton spectrum, the MOP peak is shifted to higher energies and it features a drastically increased number of entries in the energy range above 6 keV, forming a second, TR peak at 7.8 keV. In the same way, as for the protons, the superelevation seen at energies above 20 keV and the sudden cut-off above 30 keV are due to the limited ADC energy range and the variation of pedestal positions, as mentioned above.

¹⁰1013 mbar, 20°C

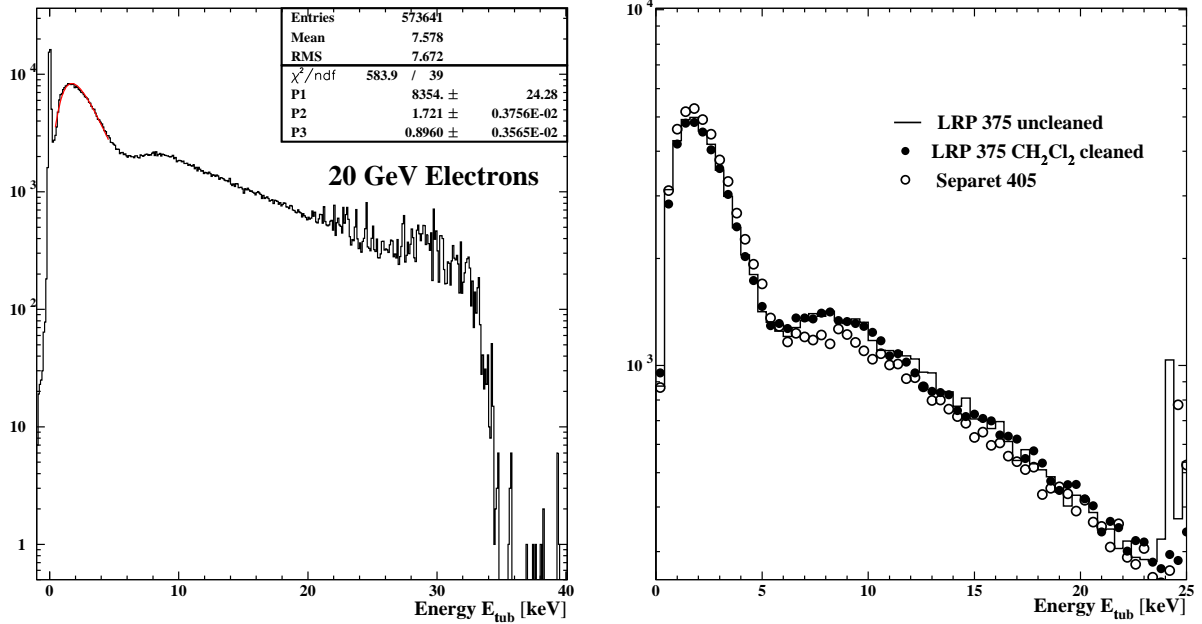


Figure 5.10: a) 20 GeV electron spectrum, containing the hits on the track of all selected single track events, recorded during the X7 beamtest; b) comparison of e^- spectra from, at each case, 3 successive layers with the same radiator material in front.

This shown spectrum was recorded inside the N-Tower of the prototype, which was uniformly equipped with the uncleaned ATLAS radiator material, referred to as "LRP 375", as introduced to in the previous chapter. For the radiator test, to be discussed in this section, part of the P-Tower was equipped with cleaned ATLAS fleece and another with the "Separet 405" material (see as well chapter 4). Figure 5.10b contains the energy spectra from only those 3 layers with the specific radiator material in front. All three histograms are normalised to the same number of entries and as a result of the lower statistics, the number of bins are reduced by a factor of 4. Clearly visible, in this figure, is the qualitative good agreement between the spectra recorded with the uncleaned (histogram) and cleaned (filled circles) ATLAS fleece and the reduced height of the TR peak of the third, Separet 405, spectrum (open circles). A more quantitative measure to compare such spectra with TR contributions from different radiator materials is to look at the height ratios of the TR and MOP peak. For the first named spectrum, this ratio is determined to 28.3 % and within the errors reproduced for the second. As for the third material, this ratio is calculated to 23.6 %, which is a relative reduction by 16.5 %. This result can be reproduced from the ratio of entries above and below the energy threshold of 6 keV, mentioned above, used to divide between spectrum's MOP and TR region. That means, energy depositions above this threshold, referred to as "TR clusters", have a high probability to have a TR photon absorbed. For that reason, this threshold, and variations of it, plays an important role in the so called "Cluster Counting" method, used to determine the e^-/p^+ -separation power of the prototype, which will be explained in the next section.

5.3 Proton Rejection Analysis

The main purpose of this 20 layer prototype was to measure the proton rejection as a function of proton energy. The proton rejection is defined as the ratio of the numbers of incident protons to those selected, whereas the total number of electron events are not reduced below 90 % by applying the same cuts.

In the following the expression "electron efficiency" denotes the fraction of accepted to the total number of incident electrons¹¹. The design goal for the prototype on the proton rejection¹¹, at 90 % electron efficiency, was set to 100 up to 250 *GeV*, the maximum available proton energy during the beamtests. In a first step, the number of hits on the track above a certain energy threshold, is counted for every selected event, referred to as Cluster Counting method. This method results in a proton rejection of (76 ± 3) at 250 *GeV* proton energy. In a second step the normalised energy spectra of electrons and protons are used as probability distributions. For each single track event, the likelihood for an event to be "electron-like", from all hits on the track, is calculated from the appropriate probabilities. This is done for three different likelihood definitions and results in a minimum proton rejection of (143 ± 12) at 250 *GeV* proton energy.

Electron Reference Sample For the analysis, to be described below, the 20 *GeV* electron data, recorded in the prototype's N-Tower, served as reference sample. This electron energy was chosen, because on the one hand for particles with γ -factors above 10^4 neither the ionisation energy loss nor the generation of TR still change when the particle energy is further increased. Figure 5.11 compares the energy spectra of 20 and 80 *GeV* electrons, normalised to the same number of entries. For a detailed comparison, the difference of the two spectra's bin entries, normalised by the squared sum of the statistical errors, is plotted for each energy bin. The only significant difference between the two spectra lies in the energy range below the MOP peak, but still its position, the ratio of entry numbers above and below 6 *keV*, as well as the overall shape of the two spectra, are in good agreement.

On the other hand, with increasing electron energy, the percentage of single track events in a raw data sample decreases, and for that reason, that electron energy was chosen, that provided the maximum number of single track events. No matter that in principal the electron spectra, measured in the mentioned electron energy range, do not significantly differ, the data samples are not added together to increase the event statistics. This is because, the electron beams have a small remaining contamination uncertainty¹² with for instance pions. A possible pion contamination of a few per mil cannot be identified in the energy spectrum, but can affect the calculated rejection factors. Additionally to that, the electron runs are taken at changing gas densities, which can only overall be corrected for. But this change in gas density has the additional

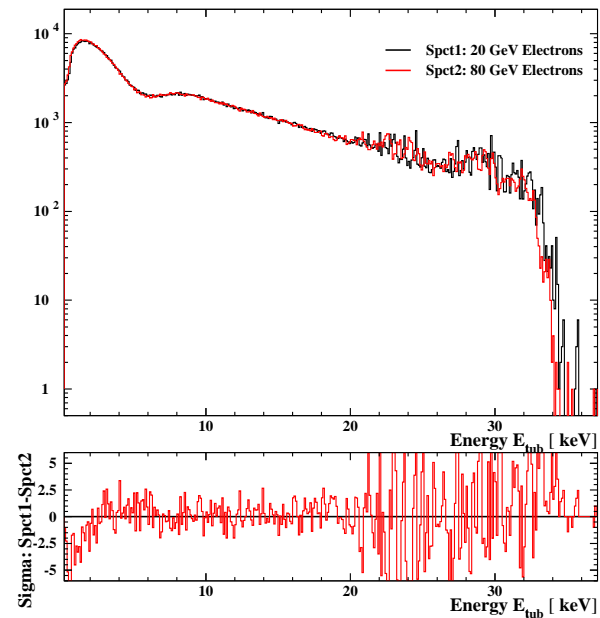


Figure 5.11: *Comparison of 20 and 80 GeV electron spectra. Additionally plotted, is the difference of the two spectra's bin entries, normalised by the squared sum of the statistical errors.*

¹¹ e^- efficiency: $\frac{\text{accepted } \#e^-}{\text{total } \#e^-}$; p^+ rejection: $\frac{\text{total } \#p^+}{\text{selected } \#p^+}$

¹²The purity of the X7 electron beam is specified as $\gtrsim 99\%$ [61].

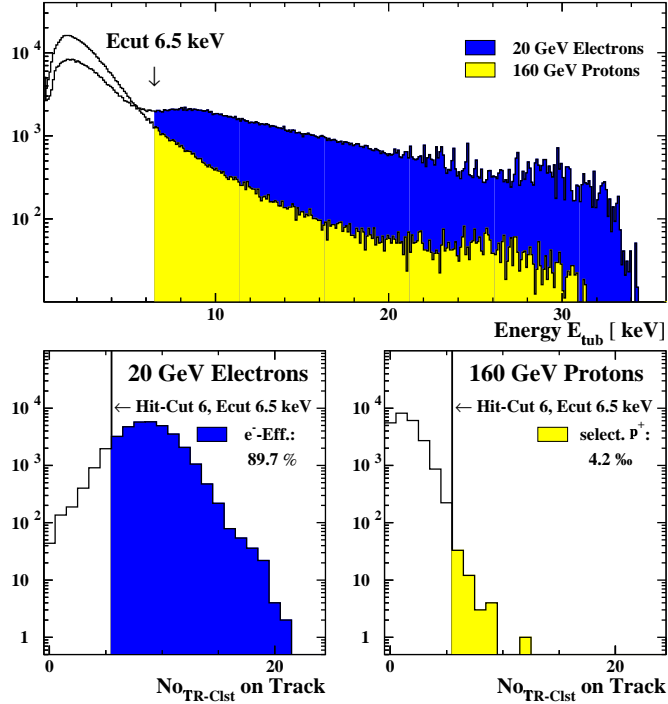


Figure 5.12: *The Cluster Counting method. a) Energy-cut(E_{cut}) definition; b,c) The Hit – Cut is chosen such that the electron efficiency is 90 %.*

effect that the TR and MOP peaks are shifted against each other. This is, on the one hand, a result from the different gas gain dependence on the density, as discussed earlier in this and the previous chapter (see page 47), but as well because of subtle changes in the absorption probabilities for the TR photons due to the change in density. As a matter of these facts, the number of event samples that were added together were kept relatively small and restricted to only one electron energy. In order to check for possible effects on the rejection factors, the analysis was redone with the total 40 GeV electron data sample.

5.3.1 Cluster Counting Method

The Cluster Counting method is based on the counting of those hits on the track, in each event, that are above a certain energy threshold (E_{cut}), as defined in figure 5.12a. The application of this method to all 20 GeV electron and 160 GeV proton events, results in distributions as displayed in the figures 5.12b and 5.12c, respectively. These displayed distributions state, that a minimum number of hits above the defined E_{cut} , referred to as *Hit-Cut*, is required, for an event to be selected as "electron-like". In the given example (see fig. 5.12), all hits above an E_{cut} of 6.5 keV are counted and a *Hit-Cut* of 6 still selects almost 90 % of the electron events. The same cut reduces the number of protons down to 4.2 %, which is equivalent to a proton rejection of 238. Additionally to this example, the requested 90 % electron efficiency can be achieved from several other E_{cut} and *Hit-Cut* combinations. For a fixed *Hit-Cut* the E_{cut} can be varied and the derived proton rejection factor can be plotted as a function of electron efficiency. In figure 5.13a this is done for the *Hit-Cuts* 5 and 6 and the E_{cut} is varied from 5 up to 10 keV. The numbers, attached to the markers, indicate the applied E_{cut} (in keV). The distribution shows an exponential behaviour, out of which the rejection factor, referring to exact 90 % efficiency, is derived from linear interpolation.

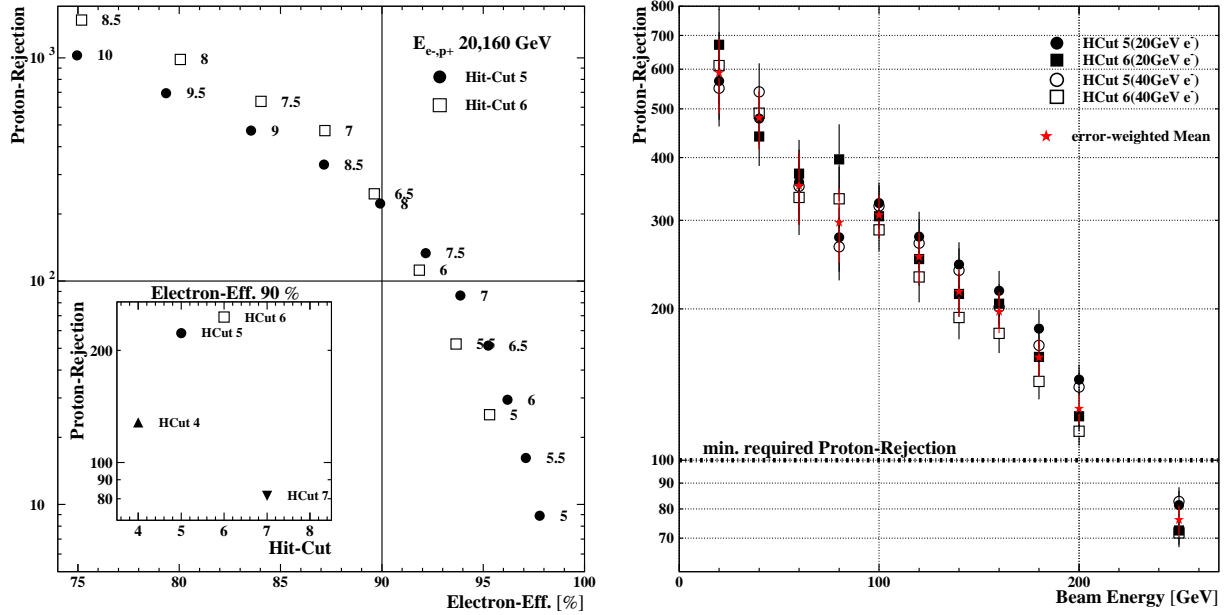


Figure 5.13: a) p^+ -rejection as a function of e^- -efficiency. Attached numbers indicate the applied E_{cut} [keV]. Embedded; Dependence of the p^+ -rejection on the Hit - Cut, at 90 % efficiency; b) Proton rejection as a function of beam energy. Exponential declension down to an average rejection of (76 ± 5) at 250 GeV proton energy.

A requested 95 % electron efficiency would reduce the proton rejection power by at least a factor of 4, whilst accepting a 20 % loss of electrons decreases the uncertainty of a proton contamination in the remaining electron sample by roughly a factor of 4. This figure also shows the rejection factor, in this example, to be more than a factor of 2 better than the requested lower limit of 100.

The embedded second figure plots the relation of the proton rejection to the used *Hit-Cut*, in each case referring to 90 % efficiency. This second chart points out, that the chosen *Hit-Cuts* (5 and 6), as displayed in the big plot, already relate to the best possible rejection factors. The choice of a lower or higher *Hit-Cut* value would worsen the maximal achievable e^-/p^+ separation power.

Proton Rejection versus Beam Energy The described procedure is carried out separately for all available proton energy samples, applying the *Hit-Cuts* 5 and 6 and using the mentioned 20 and 40 GeV electron samples as reference. The resulting proton rejection, as well as their error weighted means, are plotted as functions of beam energy, like displayed in figure 5.13b. The displayed distributions are, within the statistical errors, well consistent with each other. The distributions show an exponential declension down to an average proton rejection of (76 ± 5) at 250 GeV proton energy. The conclusion for this first analysis step is, that even this simple method results in a proton rejection above the requested limit up to an energy of 200 GeV. A more sophisticated, second method is making use of the full energy deposition of each hit on the track. Instead of the binary counting of hits, it calculates the likelihood of each event to be proton- or electron-like. This method reduces the remaining proton background by roughly a factor of 2, as will be shown later in this chapter.

Comparison with Binomial Statistics The ionisation energy loss of charged particles is a statistical process. The high energetic tails of the recorded energy spectra are the result of statistical fluctuations in the actual energy loss. That means it is a matter of pure chance, with a certain probability, to get an energy deposition from ionisation, above the current energy threshold (E_{cut}). As a matter of that fact, the derived proton *Hit-Cut* distributions can be described by binomial statistics (see [36]) with parameters $n = 20$, according to the 20 detector layers, and the appropriate probability, p . This probability is derived from the total energy spectrum, as the fraction of entries¹³ above the applied energy threshold. Figure 5.14 compares the *Hit-Cut* distributions for 160 and 250 GeV proton energies and the appropriate binomial distributions, normalised to the same integral number of entries. This comparison points out a good agreement between the data and the statistics distribution for the 160 GeV protons, with only additional 10 % selected data events, compared to the statistical expectation. Whilst these numbers of entries differ by more than a factor of 2, in the case of the 250 GeV proton sample. A detailed scan of these events above the applied *Hit-Cut* reveal a noticeable number of events with 5 and more successive high energetic hits on the track. This being statistically very unlikely ($\lesssim 5 \times 10^{-7}$), gives rise to the assumption that a second particle has passed through the same set of detector tubes. This second particle could be a collinear second primary proton or a secondary particle, produced in an interaction in front of or inside the detector volume, that is emitted

in the particle's forward direction. Such events worsen the derived proton rejection, but still cannot be extracted from the sample, as all other multiple or secondary track events. A comparable GEANT simulated 250 GeV proton sample, generated with only one primary proton per event, shows a similar agreement with the binomial statistics as the 160 GeV proton distribution, as will be shown and further discussed in chapter 6 (s. page 95).

Selection Cut Adjustment

This *Hit-Cut* method provides the chance to adjust the selection cuts for single track events, to gain best proton rejection results. In order to do so, histograms are filled which display the distribution of one single selection cut variable, with all, but the plotted, cuts applied. Supplementary to these, so called, " $n-1$ " histograms, equal histograms with an additionally applied *Hit-Cut* are filled. Figure 5.15 shows two of these " $n-1$ " histograms, derived from the 160 GeV proton sample, in comparison with their " $(n-1)+H_{cut}$ " histograms, for the spectrum of the second threshold Čerenkov Counter¹⁴ and the "hiton"¹⁴ selection cut.

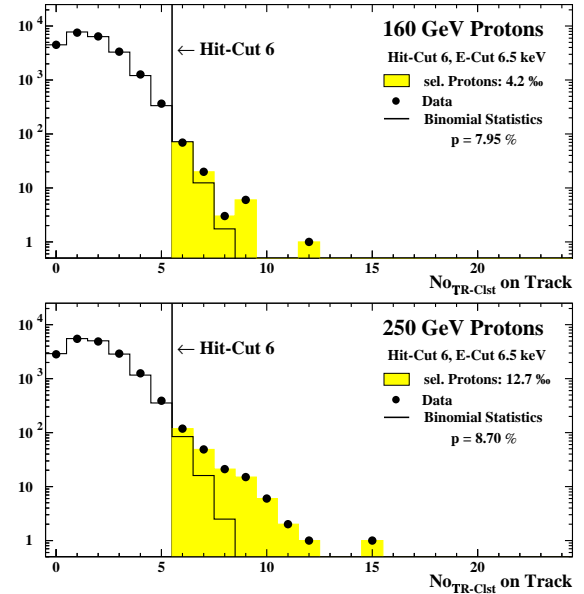


Figure 5.14: *Hit-Cut* distributions in comparison to the appropriate binomial distributions, with parameters $n=20$ and p , the fraction of entries, above the applied E_{cut} , here 6.5 keV, of the total energy spectrum.

¹³disregarding the pedestal entries

¹⁴Čerenkov Counter 2 from the X7 beamtest, filled with He gas; "hiton" = Number of hits on XY-track

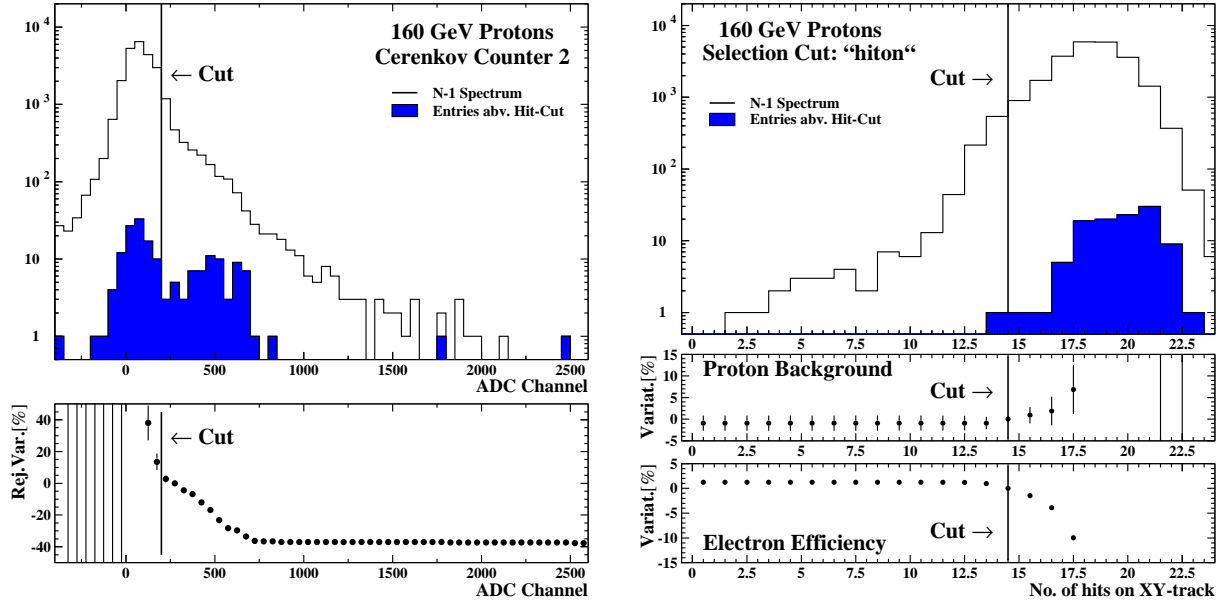


Figure 5.15: " $n-1$ " distribution and variation of selected proton number for a) the second Čerenkov counter; b) the "hiton" selection cut. In this second case, the electron efficiency variation is additionally plotted.

The first displayed comparison (fig. 5.15a) reveals two clusters of events in the " $(n-1) + Hcut$ " histogram, where only the first type is consistent with the pedestal. Due to the fact, that the Čerenkov Counters were used to trigger on everything but the protons, the spectrum should contain pedestal events only and for that reason it is self-evident to exclude the second cluster of events. In principle, the proton rejection, in each case, can be calculated as the number ratio of entries in the two displayed histograms above (or below¹⁵) the selection cut.

Cut Variation A variation of the applied cut results in changed proton rejection and electron efficiency values. The resulting distributions, as additionally displayed in the lower half of figure 5.15, show the percental deviation of the proton rejection (electron efficiency) from the nominal value¹⁶, as a function of the selection cut. In the first example, only the variation of rejection power is plotted, because the Čerenkov Counters were used for the proton measurements, only. As expected from the above discussion, the rejection power noticeably increases by 37.7 %, while the total proton sample is reduced by 12 % in number, when excluding the second cluster of events. The second displayed example shows the variation of the number of hits on the XY-track ("hiton"). These variations show less drastic dependencies of the rejections and efficiencies from the chosen selection cut. Both distributions feature only minor changes up to the nominal cut and steep deviations above.

5.3.2 Likelihood Method

The likelihood method is making use of the full information that the particle energy spectra contain. These spectra (see figure 5.12a) are normalised to an integral of one and then used as probability density distributions (segmented into 0.1 keV bins) for each hit.

¹⁵depending on the cut "orientation"

¹⁶rejection (efficiency) value at the nominal selection cut (see table 5.1), in each case, corrected for the change in total number of entries

The probabilities for each hit on the track are then accumulated via summation, multiplication or a combination of both. From that the likelihood, for an event to be electron-like, is calculated, according to three different definitions. As can be seen from figure 5.15b, the number of hits on the track changes from event to event. For that reason the derived likelihood values are normalised by the appendant number of hits in the event.

Likelihood Definition Three likelihood definitions have been utilized for this analysis and the detailed general description of this method will be given for that definition which resulted in the best e^-/p^+ -separation. In each case, the probability $P_{e,p}(E_{dep})$ for an energy deposition E_{dep} to be electron- or proton-like, respectively, is derived from the probability distributions. The expression "hit" in the following always refers to hits on the track.

Definition I The best performance likelihood definition foresees the multiplication of probabilities for all hits, in each single event. Such products are evaluated, separately, for the electron and proton probabilities and the geometric means

$$P_{e,p}^{mean} = \sqrt[n]{\prod_{k=1}^n P_{e,p}^k(E_{dep})} \quad (5.3)$$

, where n is the number of hits, are calculated. The likelihood L_e for an event to be electron-like, is then derived from the probability ratio:

$$L_e = \frac{P_e^{mean}}{P_e^{mean} + P_p^{mean}} \quad (5.4)$$

This can be done for a full electron and proton sample and the $-\ln(L_e)$ values are filled into separate histograms, as figure 5.16 shows for 20 GeV electron and 160 GeV proton single track events.

In the displayed distributions low $-\ln(L_e)$ values are an indicator for electron-like events. As for that reason expected, the electron sample peaks at 0.44, a factor of 2 lower, compared to the peak position of the proton distribution. The likelihood cut (*LH-Cut*), as indicated in the figure, is chosen such, that a 90 % electron efficiency can be sustained. The proton rejection is now calculated as the inverted percentage of proton events selected as electron-like, using the same *LH-Cut*, to the total number of proton events in the sample. The errors on the derived proton rejection values are calculated from the statistical errors of the number of hits below the applied *LH-Cut*. The relative error of each rejection factor is on the order of 10 %. For the example given in figure 5.16 the relative number of selected proton events is deduced to $(2.3 \pm 0.3) \%$, which relates to a proton rejection factor of (435 ± 57) .

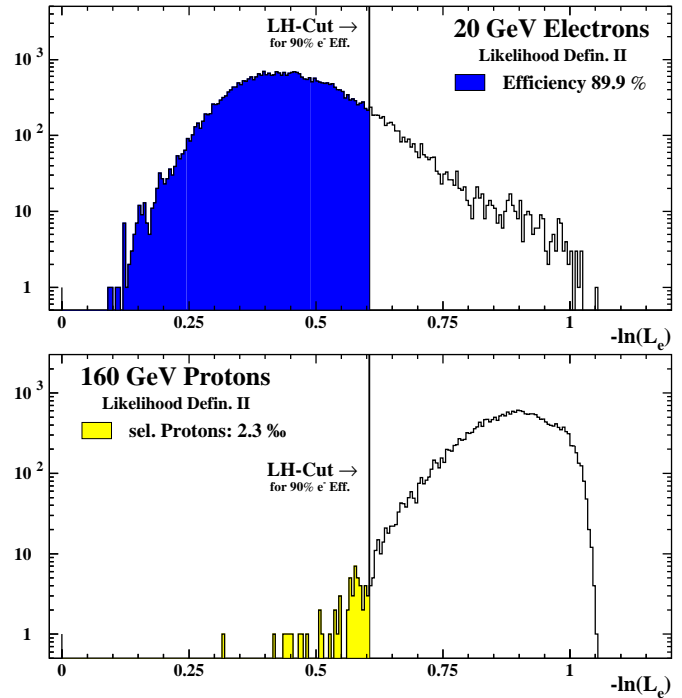


Figure 5.16: Likelihood distributions, on logarithmic scale, for the 20 GeV electron and the 160 GeV proton samples. The likelihood for events to be "electron-like" is plotted.

This states an improvement by more than a factor of 2, compared to the Cluster Counting result and with respect to the requested lower limit of 100, this value denotes more than a factor of 4 better e^-/p^+ separation. The variation of the electron efficiency causes, in a similar way as for the Cluster Counting method, a drastic change in the proton rejection, as figure 5.17 shows for all three likelihood definitions. Out of these distributions the rejection factors for exact 90 % electron efficiency are derived from linear interpolation.

Referring to the first definition, represented by the filled squares, a demand for 95 % electron efficiency would worsen the proton rejection by roughly a factor of 4 and accepting a 20 % loss of electron events improves the separation power by more than a factor of 3, up to 1400.

Definition II The second likelihood definition calculates the probability ratios

$$P_e^{hit} = \frac{P_e(E_{dep})}{P_e(E_{dep}) + P_p(E_{dep})} \quad (5.5)$$

for each hit. The likelihood L_e for an event to be electron-like is then defined as the arithmetic mean of all P_e^{hit} probability values in an event

$$L_e = \frac{1}{n} \cdot \left(\sum_{k=1}^n P_e^k \right) \quad (5.6)$$

where n is the number of hits. The such derived rejection factor as a function of electron efficiency is as well plotted in figure 5.17, represented by the filled circles. It denotes a rejection factor of (385 ± 49) , at 90 % electron efficiency. The comparison to the distribution, derived from definition I, states systematically lower rejections from this second definition, but an agreement of these two within the statistical errors¹⁷.

Definition III For completeness the application of a third definition shall be briefly mentioned, because it represents a standard likelihood definition [62]. This definition was tested, because it corrects for changing numbers of hits in an event without the necessity of direct averaging. It combines summation and multiplication of integral probabilities $P_{e,p}^*$, that are defined according to

$$P_p^*(E_k) = \int_{E_k}^{\infty} P_p(E) dE \quad \text{whereas} \quad P_e^*(E_k) = \int_0^{E_k} P_e(E) dE$$

where the $P_{e,p}(E)$ denote the probabilities as used for the other two likelihood definitions. Since proton events are expected to have mainly lower energetic hits compared to those from electron events¹⁸, the $P_{e,p}^*$ probabilities are defined such that they range from 0 to 1 with increasing (P_e^*) or decreasing (P_p^*) energy depositions E_k , respectively.

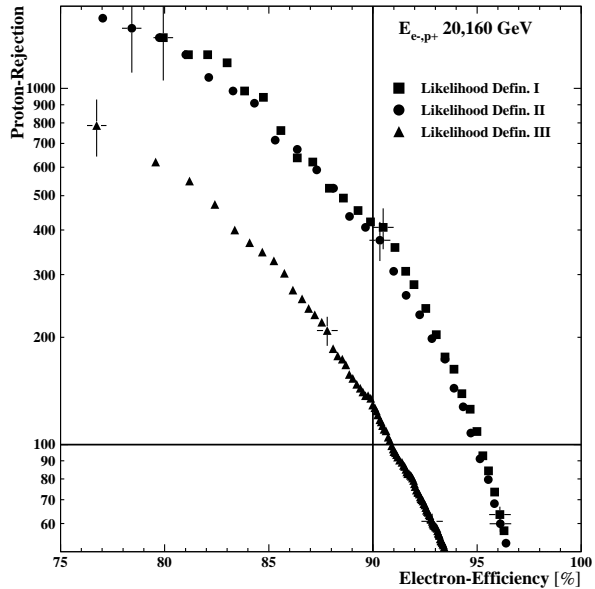


Figure 5.17: *Proton rejections, derived from the three different likelihood definitions, as functions of electron efficiency. Error bars are only exemplary plotted to keep the distributions comparable.*

¹⁷rel. stat. errors: $\sim 10\%$ (rej.) and $\sim 0.5\%$ (eff.), error bars are only exemplary plotted

¹⁸in the energy ranges of the prototype measurements

Out of these single hit probabilities the event probabilities $P_{e,p}^{ev}$ for the proton and electron hypothesis can be calculated according to

$$P_{e,p}^{ev} = \prod_{i=1}^n P_{e,p}^{*i} \cdot \left\{ \sum_{j=0}^{n-1} \left(-\ln \prod_{k=1}^n P_{e,p}^{*k} \right)^j / j! \right\} \quad (5.7)$$

where n is the number of hits. The likelihood L_e for an event to be "electron-like" is then derived from the ratio of event probabilities according to equation 5.4. The reference proton rejection at 90 % electron efficiency, in this case, is calculated to (136 ± 10) for the example of 160 GeV protons. This denotes a reduced rejection by more than a factor of 3 compared to the definition I value. The full deduced "rejection-versus-efficiency" distribution, in figure 5.17 represented by the triangles, confirms this worsened definition III proton rejection over the full range of electron efficiencies.

This drastically reduced separation power compared to the other two methods reproduces over the full range of proton energies. For that reason this third likelihood definition will be disregarded for the remainder of this analysis.

Proton Rejection versus Beam Energy In the same way as described for the 160 GeV proton sample, the proton samples of all other energies are analysed, for both electron references. The deduced proton rejections as functions of beam energy are plotted in figure 5.18 for the first two likelihood definitions. From this figure it can be clearly seen, that the deduced proton rejection factors are well above the requested lower limit of 100 up to 250 GeV proton energy. The definition I rejection value for this highest measured proton energy is calculated to (143 ± 13) . In each case, the results derived from the 20 and 40 GeV electron reference analyses are in good agreement within the statistical errors. The comparison of the distributions from the two different likelihood definitions show similar relations as in the above discussed example. The likelihood definition I always results in the best rejection factors and the average relative difference to those from definition II is 11.2 %.

For comparison the Cluster Counting average distribution is additionally plotted. This distribution features rejection factors, on average reduced by more than a factor of 2 compared to those derived from definition I likelihood.

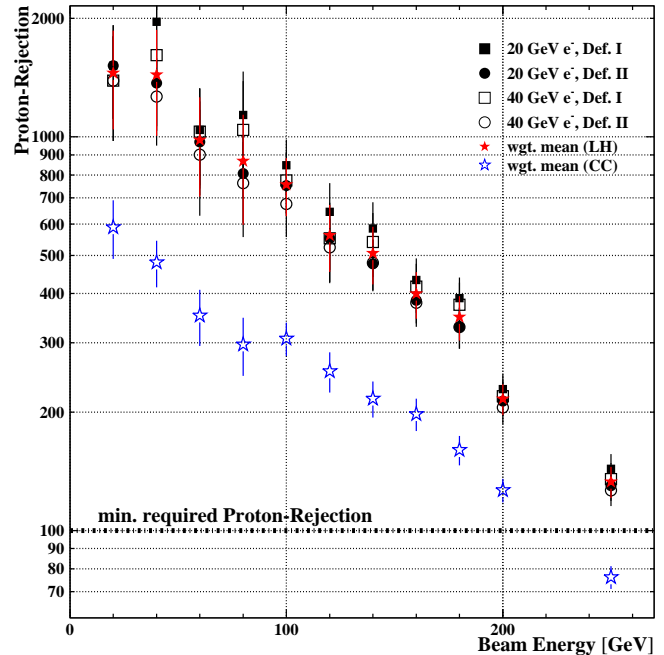


Figure 5.18: *Proton rejection as a function of beam energy. Exponential declension down to a rejection (def.I) of (143 ± 13) at 250 GeV proton energy. Additionally plotted is the average Cluster Counting distribution.*

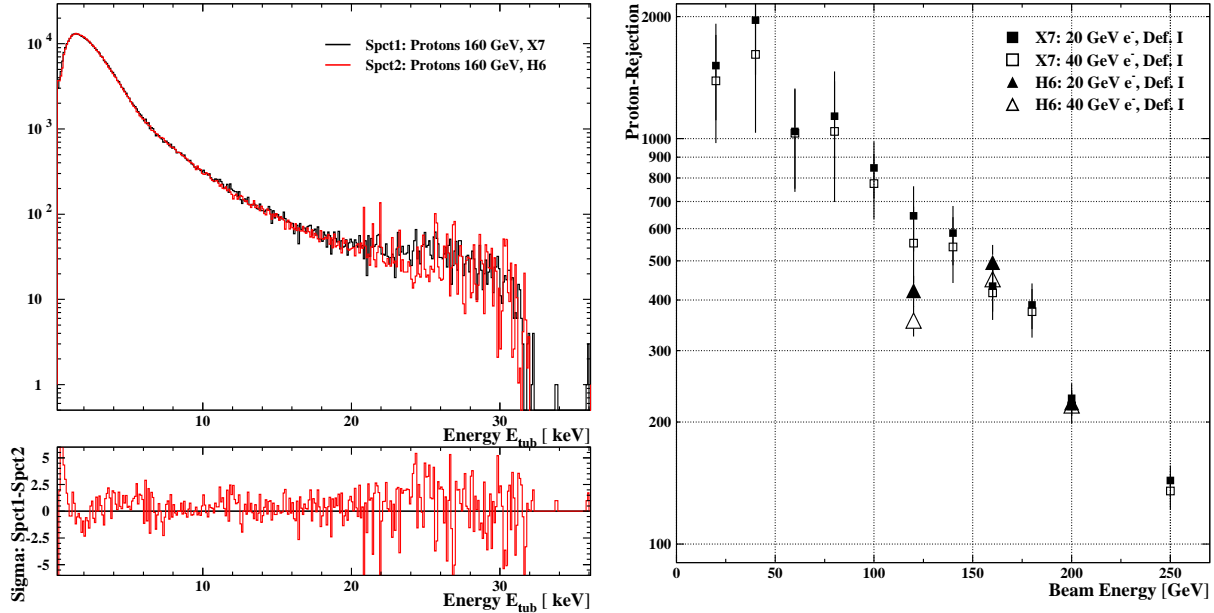


Figure 5.19: a) Comparison of the 160 GeV proton spectra recorded during the X7 and H6 beamtests; b) Proton rejection for the H6 beamtest data, derived from definition I, as a function of beam energy. Additionally plotted, is the equivalent proton rejection distribution from the X7 beamtest.

Results from the H6 beamtest During this short second beamtest, proton data with only three different energies, namely 120, 160 and 200 GeV were recorded. These measurements were carried out to check the X7 beamtest results. The special feature of this second beamtest was a differential Čerenkov counter, that is used to directly trigger on proton particles. Its usage drastically reduces any possible contamination of the gathered proton samples with lighter particles, such as pions, like discussed in chapter 4. As the first test, the energy spectra recorded during the X7 and H6 beamtests are compared.

Comparison of the Spectra Figure 5.19a shows this comparison of the two spectra, normalised to the same number of entries, for the example of 160 GeV proton energy. In a similar way as for the comparison of the electron spectra (see fig.5.11), for each energy bin, the difference of the two spectra's bin entries, normalised by the squared sum of the statistical errors, is plotted. The two displayed spectra are in good general agreement. The MOP peak positions show a relative difference of only 1.2 %, which is well within the error on the gas gain correction. The rejection analysis is carried out in the same way as for the X7 beamtest.

Comparison of the Rejections The Cluster Counting analysis reproduces, within the statistical errors, the appropriate rejection factors, presented for the X7 beamtest. The likelihood definition I analysis for both electron references reveal consistent rejection factors, from X7 and H6 beamtests, for the 160 and 200 GeV proton energies (see fig. 5.19b). This confirmation of the X7 beamtest results resolves all doubt about a possible pion contamination in the proton samples, which would have artificially worsened the derived e^-/p^+ separation powers.

Despite the good agreement of the last two, the 120 GeV data point depict a clear discrepancy, which, however, can be easily resolved. The profile of the H6 beam has a width of only 8 mm, which is roughly a factor of 10 smaller compared to that of the X7 beamline.

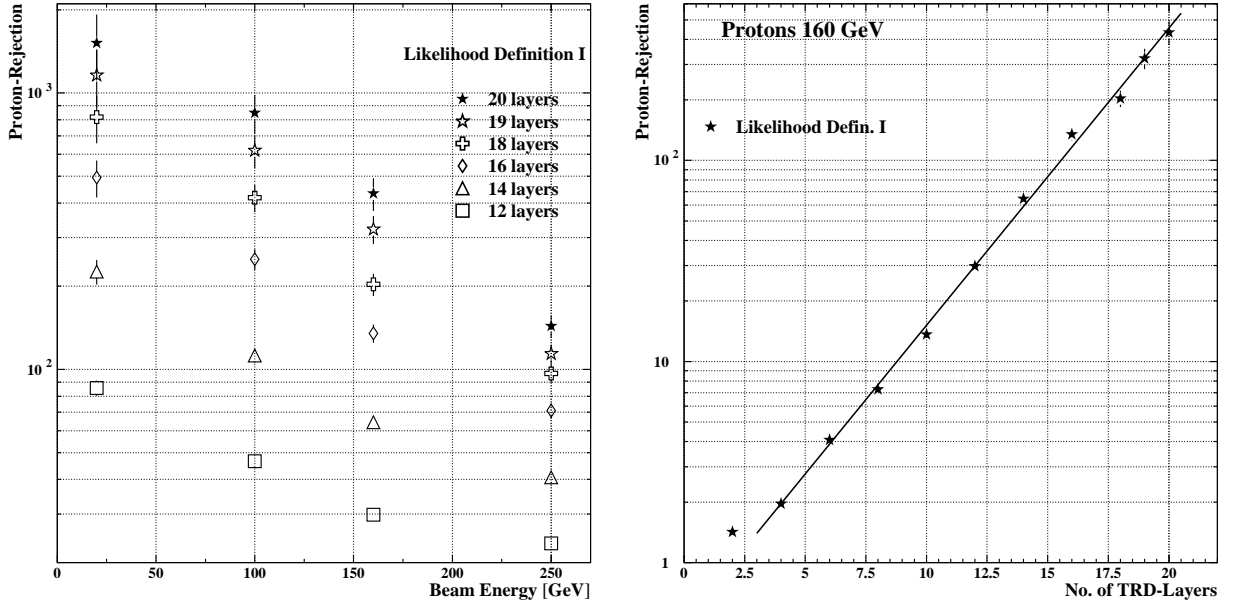


Figure 5.20: Proton rejection as a function of active layer number. Rejections are calculated from Likelihood definition I. a) Layer variation from 20 down to 12 active layers for 4 different proton energies; b) Layer variation from 20 down to 2 active layers, performed for 160 GeV proton energy.

Due to this fact, more than 60 % of the beam traverses one and the same tube, in each layer, for all the recorded events. The set-up, for those two proton runs, accounting for the full 120 GeV proton sample, was accidentally chosen such, that the maximum number of particles passed through an unrecognized dead channel in layer 3 (tube No. 25, see i-cal table 5.4). On the one hand, this reduces the number of "active" layers from 20 to 19, for more than half of all events in that sample. On the other hand, layer 3 is one of the horizontal layers, and a missing fourth hit on the X-track increases the probability for a failed track reconstruction, which leads to discarding all remaining hits from the rotated layers, a reduction by 4 "active" layers, even. A permanent loss of only one of the 20 layers already reduces the rejection power by roughly 35 %, as will be explained in the subsequent section. The displayed relative difference between the two sets of data points is 43.5 %.

Proton Rejection versus Number of Layers As explained in chapter 4, the modules in the AMS TRD will be electrically grouped into towers of 4. In the case of a failure¹⁹ of only one channel out of these four modules, the entire group has to be disconnected from the high voltage supply. That means a loss of four successive layers in this detector segment. In order to gain information on the effect of such a failure on the e^-/p^+ -separation, the analysis has been repeated with varying numbers of active layers. In order to keep the comparability of all deduced results, the layer number is reduced not until the single track event selection is done. This ensures the analysis of the same single track events, in all cases.

This part of the analysis was carried out for 12 up to 20 active layers and repeated for four different proton energies, ranging from 20 up to 250 GeV. The proton rejection factors are derived from likelihood definition I and the 20 GeV electron reference.

¹⁹e.g. due to an HV short cut; a gas leak would mean a loss of 2 neighbouring towers even.

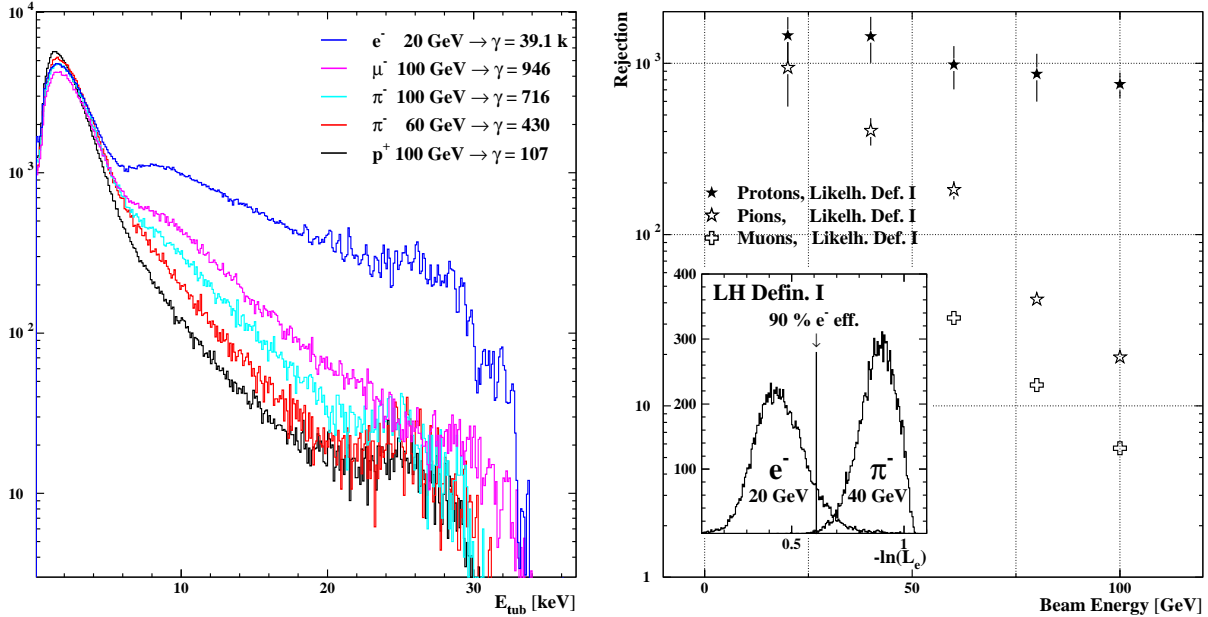


Figure 5.21: a) Energy spectra recorded with particles at various different Lorentz factors; b) Pion & muon rejection factor as a function of beam energy. Exponential declension down to $(19.2 \pm 0.7)[(5.7 \pm 0.1)]$ at 100 GeV pion [muon] energy. For comparison the average likelihood distribution from the proton analysis is additionally plotted. Embedded; Likelihood distributions for 40 GeV pions compared to that of 20 GeV electrons.

Figure 5.20a displays these layer variations. Each of the distributions show a similar exponential decrease in the rejection as a function of proton energy, compared to the 20 active layer case. As can be seen in the figure, a failure of one tower would worsen the e^-/p^+ separation power by an average factor of ~ 3 for the the first three energies, only the results from the 250 GeV proton sample show a somewhat smaller reduction factor. In the same way as before, these results denote the worst case scenario, because of the perpendicular incidence of the testbeam particles (see also page 49 of chapter 4).

For the 160 GeV proton energy the reduction procedure was continued down to a number of only 2 remaining active layers. This was to check the exponential dependence of the proton rejection factors from the number of layers. Figure 5.20b clearly features this expected behaviour for the plotted set of data points. On a logarithmic scale, they agree well with the additionally displayed straight line fit.

5.4 Pion & Muon Rejection Analysis

With respect to the flux rates of muons and pions in the primary cosmic rays, these particles are of little importance for the AMS experiment, but TRDs in general are very often used especially for the separation between electrons and pions. For that reason, and to possibly gain additional information on the proton rejection at higher γ factors, the rejection analysis, as described above, is applied to the recorded pion and muon runs as well and the e^-/π^- and e^-/μ^- separation powers are calculated.

A brief glance at the energy spectra of protons, pions, muons and electrons, as figure 5.21a displays, clearly shows the instanting effect of transition radiation and the dependence of TR on the Lorentz factor γ . This comparison clearly lowers the expectation on the e^-/π^- and e^-/μ^- separation powers, compared to those deduced from the proton samples.

The rejection analysis is carried out, using the definition I likelihood method and the 20 GeV electron reference sample²⁰. The available pion energies range from 20 to 100 GeV and the recorded muons have 60, 80 and 100 GeV energy. Figure 5.21b shows the results from the muon and pion analyses and compares them with the averaged proton results. Displayed in the embedded plot is the likelihood distribution of the 40 GeV pion sample compared to that of the 20 GeV electrons. These distributions are normalised to the same number of entries. The derived pion rejection factors range from (909 ± 331) up to (19.2 ± 0.7) , in each case referring to 90 % electron efficiency.

The analysis for the muons derived a factor of ~ 3 lower rejection factors compared to the appropriate pion values.

5.4.1 Rejection versus Lorentz Factor

As the final step of this analysis the derived rejection factors from all analysed particle types can be summarised in one diagram, plotting these results as functions of the Lorentz factor γ . The idea is to gain some information on the proton rejection at energies above 250 GeV , since transition radiation is known to depend only on the γ -factor. Figure 5.22 shows this summary diagram. This summary reveals a clear discrepancy between the combined distributions of muons and pions with that of the protons. Both distributions show the typical exponential dependence on the γ -factor. On the displayed logarithmic scale they follow straight lines, but for the proton distribution with a significantly steeper slope. This discrepancy is believed to be a matter of the difference in the cross section for interactions of protons and pions with the detector material. As a result from that an increased number of proton events suffer from interactions with the detector, producing secondary particles, as already addressed earlier in this chapter (see page 70 and the discussion on binomial statistics). A detailed scan of all 250 GeV proton events below the likelihood cut, revealed 40 % of these events with a clear structure of at least 4 successive hits above 6.5 keV on the track. This, being statistically very unlikely to originate from pure ionisation fluctuations²¹, gives rise to the assumption that the difference between the two distributions is not due to a difference in the generation of transition radiation.

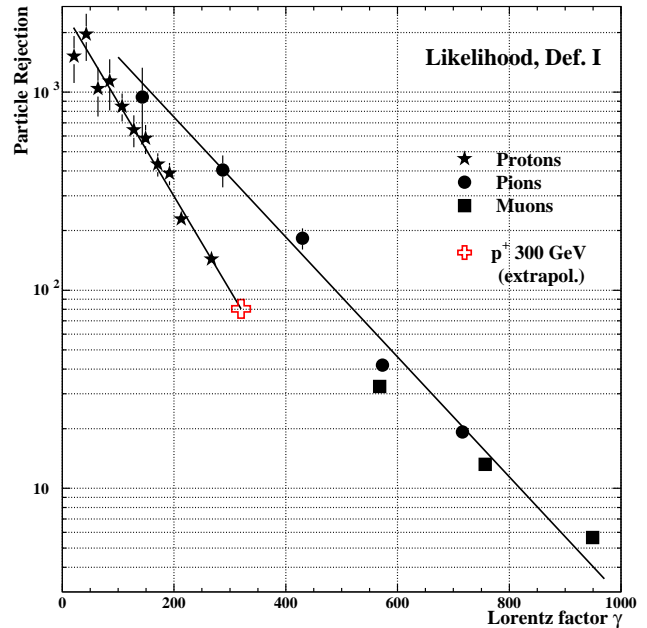


Figure 5.22: Particle rejections as a functions of the Lorentz factor, γ . Distributions show the expected exponential dependence on γ , where, on the logarithmic scale, the Proton distribution seems to have a significantly steeper slope compared to those from Pions and Muons.

²⁰Similar to the protons, the pion Cluster Counting analysis deduces a factor of ~ 2 lower rejections.

²¹the fraction of entries above 6.5 keV , in the 250 GeV proton spectrum, amounts to only 8.7 %.

It is more likely caused by additionally deposited energy from generated secondary particles, emitted in the forward direction of the primary incident particle. These extra energy depositions are mainly due to ionisation energy loss, but can as well be accompanied by an increased number of absorbed transition radiation photons, emitted from high energetic secondary particles. The such increased number of hits, with energies well above the most probable ionisation energy loss for protons, increases the probability for these events to be selected as "electron-like".

As an immediate result from that, a direct statement on the proton rejection at energies above 250 GeV cannot be deduced from the presented pion results. Nevertheless, the proton distribution is in such well agreement with the straight line fit that an extrapolation to a proton energy of 300 GeV can be justified. This is done because the lower limit on the proton rejection of 100 originally referred to this proton energy. From such a linear extrapolation a value of (80 ± 10) is calculated (as indicated in the figure). This extrapolated rejection factor still agrees with the required design goal within 2 standard deviations.

Chapter 6

Monte Carlo Simulations

The second major purpose of this work was to improve the Monte Carlo (MC) simulations for the AMS-02 transition radiation detector (TRD). The GEANT software package [63] and additional supplements to recalculate the ionisation energy loss and to generate and detect TR, first implemented by members of the HERA-B Collaboration [52], were used to reproduce the beamtest results, as presented in the previous chapter. In these MC simulations two types of parameters were used and optimised such, that a best agreement to the beamtest data was achieved. The first parameter type was used to adapt the measurement conditions and to precisely introduce the prototype detector into the GEANT simulation. Whereas the second type directly affected the generation and detection of transition radiation. The overall number of produced TR-photons and their absorption probability, as well as the overall shape of the TR energy spectrum, were tuned in this adjustment process. In that way, these simulations provided the opportunity to test the beamtest results and generate a more detailed understanding of the processes inside the TRD. Monte Carlo simulations, carried out with the final set of parameters, well reproduce the measured energy spectra for protons and electrons in the full energy range of the measurements. The rejection factors deduced from data and these MC simulations are, as well, in good agreement up to a proton energy of 160 GeV .

A brief description of the GEANT software package and its supplements is subject of this chapter. A second part introduces the used parameters and explains the adjustment process. This chapter concludes in a comparison of the MC simulated energy spectra and derived rejection factors with those from the beamtest data.

6.1 The GEANT Software and its Supplements

The GEANT software package simulates the passage of particles through matter. It allows the definition of an experimental setup as a structure of geometrical volumes and the assignment of material properties, such as the nuclear composition and the density, to these volumes. The particles are tracked through the defined detector setup, until they are absorbed or leave the setup. The energy depositions in each volume are calculated. In this process, the software takes into account the volume boundaries and physical effects according to the nature of the particles themselves and their interactions with matter. Any secondary particle, produced in such interactions, is tracked through the setup, in the same way. A particle is stopped (absorbed) if its kinetic energy drops below the energy threshold, set for this specific type of particle. This threshold can be set to any particle energy value above 10 keV , which is the minimal energy GEANT can "handle". The such generated events are recorded in the form of "n-tuples".

The simulations, to be described below, are carried out with a GEANT 3.21 version, improved in the simulation of ionisation energy loss (dE/dx) in low density gases. As a supplement to the customary GEANT 3, it was programmed to generate transition radiation and account for its re-absorption inside the radiator material, as well as inside the detection gas. In the simulation of the photon absorption in the detection gas, the escape photon production from the different atomic shell levels is accounted for. These improved and additional features have been introduced into the GEANT software by V. Saveliev [52], a member of the HERA-B Collaboration. The GEANT 3 successor, GEANT 4, provides all the named features as standard processes, but had not yet left the testing stage, when these simulation activities started.

6.1.1 Simulation of dE/dx in low Density Gases

The standard GEANT simulation of ionisation energy loss in low density gases fails to properly reproduce measured spectra. For that reason, the present GEANT version is programmed to recalculate this dE/dx energy loss, based on the work of V. Ermilova [64]. This approach simulates the energy loss in a more realistic way, namely as a large number of independent interactions of a fast charged particle with the shell electrons of the gaseous matter it traverses. The simulation first calculates a Poisson distributed number of interactions within the current GEANT step. The mean value of this Poisson distribution is calculated from the current step length and the interaction probability. In the second step, an energy loss is assigned to each encounter from calculated integral energy transfer distributions, as figure 6.1 displays for the used Xe/CO_2 gas and 4 different Lorentz factors. These distributions contain the integral number of interactions per unit path length, $(dN/dx)|_{\epsilon > \epsilon_0}$, as a function of the threshold energy transfer ϵ_0 . The structure in these distributions are due to absorption edges of the various atomic shells. These integral energy transfer spectra exist separately for 21 γ -factors tabulated in the additional GEANT code, ranging from 1.5 to 2×10^5 in logarithmic steps.

Supplementary to this, single energy transfers above the minimum GEANT energy threshold of 10 keV (see above) are transformed into knock-on electrons (δ -rays), that are added to GEANT's stack of secondary particles. All other single energy losses are summed up to the full energy deposition in the current GEANT step, which is then subtracted from the primary particle's energy.

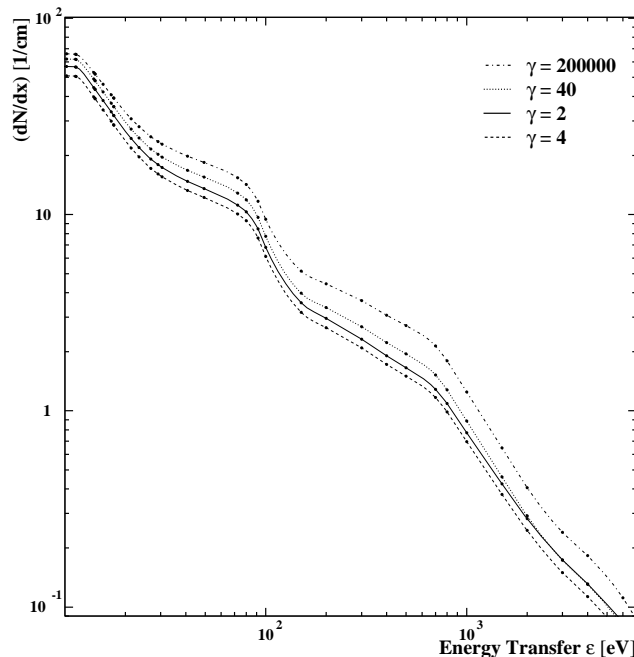


Figure 6.1: *Ionisation energy loss simulation. Energy transfer distributions in Xe/CO_2 gas for 4 different γ factors and stand. cond. (STP).*

6.1.2 The Simulation of TR

The simulation of transition radiation is based on theoretically calculated and empirically corrected probability tables, separately for 20 Lorentz factors ranging from 100 to 2×10^5 in logarithmic steps. These tables contain the integral probability to generate a TR photon from a single radiator foil, above a certain energy threshold. They are calculated for regular foil radiators according to the theoretical work of M. Cherry and G. Garibian [65, 66]. The comparisons between data and MC energy spectra¹ are then used to determine the corrections for the number of generated TR photons as well as the overall shape of the TR spectrum. For this adaptation process, members of the HERA-B Collaboration performed measurements with a regular foil stack as well as an irregular fiber radiator, similar to that used for the AMS Experiment. The such derived tables, used for the GEANT

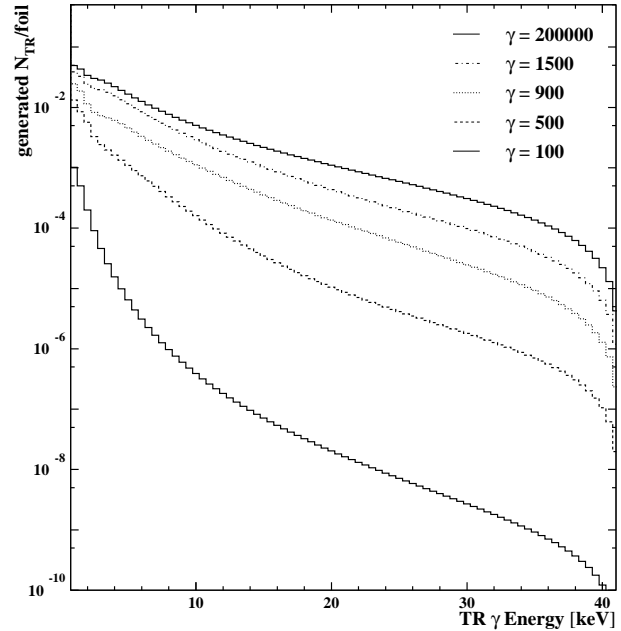


Figure 6.2: *Simulation of TR generation. Integral number of generated TR photons, in a stack of foils, as a function of TR photon energy threshold, displayed for 5 different γ factors.*

simulation, are exemplarily displayed in figure 6.2, for 5 different Lorentz factors. Clearly visible is the drastically rising probability to generate TR photons, with increasing γ factor (see also figure 3.3 from chapter 3).

For the simulated generation of TR, the number of boundary transitions, within the current GEANT step, is calculated. This number and the appropriate probability from the described tables are used to determine the number of generated photons, N_{TR} , from a Poisson distribution. The mean value of this Poisson distribution is corrected for the reduced number² of TR photons generated by the fiber radiator. In a second step, an energy is assigned to each of the N_{TR} photons, according to the relevant distribution as shown in figure 6.2. The such generated TR photons are added as "Geantinos" to the stack of secondary particles.

6.2 Real Detector Monte Carlo

6.2.1 Mechanical Setup

For the beamtest MC studies, the experimental setup, as shown in figure 6.3a, is defined precisely according to the real prototype detector. The straw tubes are implemented with 6 mm inner diameter and a wall thickness of 72 μm , filled with a $Xe/CO_2(80/20)$ gas mixture. A tungsten wire is placed in their centers. The tubes are assembled into straw modules with three integrated carbon fiber stiffeners, each.

¹measured for various particle types and at several particle energies

²compared to that from a foil stack

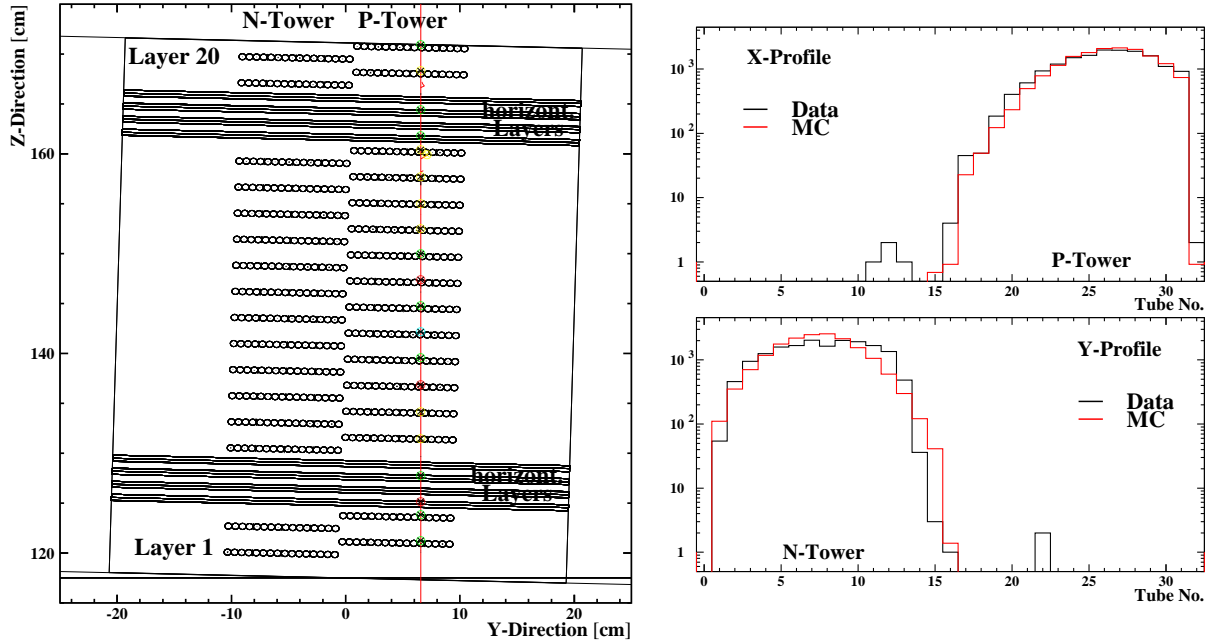


Figure 6.3: a) The prototype as defined for the MC simulations. Additionally plotted is the trajectory of a Proton that passed through the detector. The direction of the beam is from bottom to top; b) Comparison of the X- and Y-beam profiles of MC and data, plotted against the tube number hit in layer 1.

The two towers are shifted by 14.5 mm against each other. The layers of detector tubes are interleaved with 20 mm polypropylene material of the real radiator's density. This whole set of two 20-layer-towers is surrounded by a box of aluminium in which the beam inlet and outlet windows are left open. The such defined setup can be rotated with respect to the beam axis. Two sets of scintillation panels, with 1 and 2 cm thickness, respectively, are placed in front of and behind the prototype. The volume, surrounding the setup, is filled with air. Additionally plotted in figure 6.3a, is the simulated trajectory of a proton that passed through the detector. Each tube on the track is coloured according to the amount of energy deposited inside. The primary particle's origin is chosen to be at a 2 m distance in front of the detector and the beam profile is defined in a Gaussian shape, limited to the full scintillation counter width of 10 cm , to match the beamline conditions at data taking. Figure 6.3b shows separately for X- and Y-direction the comparison of the data and MC beam profiles plotted against the tube number hit in layer 1.

Average Number of Hits A first test run of the simulation uncovered a discrepancy between the average simulated number of hits on the Y-track, compared to that of the measured data. The reasons for that turned out to be twofold. On the one hand, the detector geometry and particle passage are not perfectly reproduced. This causes a smaller number of particle passages through the gaps between two tubes and thus an increased number of hits in the MC. On the other hand, the electronics efficiency is not implemented in the simulation. The upper half of figure 6.4 shows this discrepancy. The slight shift, of the MC distribution to higher numbers, is clearly visible. In order to compensate for this difference the total number of hits in the y-layers are randomly reduced down to 98% of the originally generated number. This reduction noticeably improves the agreement between the MC and data distributions, as the lower half of the figure points out. This second MC distribution features a lower mean value and a slightly increased width.

This adjustment will have special importance for the Cluster Counting Method. This is because an increased average total number of hits is directly related to a larger number of hits that exceed the *Ecut*. This especially worsens the proton rejection derived from Cluster Counting, because this method counts the absolute number of hits. The Likelihood Method is less affected by that, due to the applied averaging in the used methods (see chapter 5, page 73).

In the X-layers, and here especially for the electron runs, the opposite effect, that means an increased number of hits, is seen in the data. These hits are believed to be a result from electronics crosstalk, caused by badly electrically isolated read-out channels. This assumption stands to reason, because the additional hits are usually seen next to a second hit in the same appendant layer with a reduced signal height compared to the adjacent hit. An attempt, though, to introduce this effect into the simulation failed, since it changed from run to run in an unpredictable way. Still this extra number of hits, especially occurring in the electron runs, has a similar effect on the Cluster Counting method, as described above, and thus explains higher rejection factors derived from the data compared to those derived from MC samples (also see section 6.4.1).

Rotation Angle Supplementary, the individual simulation of each data run as well accounts for the appropriate rotation angle of the prototype, with reference to the beam axis. This is necessary, because the distribution of path lengths of the traversing particle through the individual detector tubes depends on the angle. Since a change in average path length affects the mean energy deposition of each hit, in that specific data sample, the angle has to be adapted. During the measurements, angles of -1.5° to 9.3° were used.

Gas Gain Correction In general, the gasgain correction is only applied to the measured data. Only the difference in gas gain dependence on the gas density, of ionisation energy loss and photon absorption, as discussed in chapter 4 (see page 46), has to be corrected for. In order to do so, the energy of each simulated TR photon is gas gain corrected, according to equation 5.1, from chapter 5, with the parameter $|slope|$ set to 1. This correction scales the energy spectrum's TR peak relative to its dE/dx MOP position.

6.2.2 Readout Electronics

The simulation is making use of the intercalibration and gas gain correction factors as applied to the appropriate measured data, as well as the pedestal information from each readout channel. The intercalibration table, for instance, is used to introduce the prototype's "dead" readout channels into the simulation.

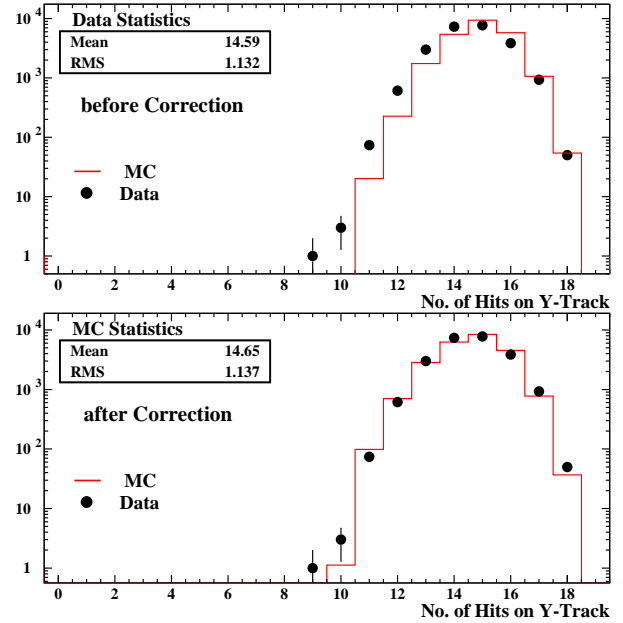


Figure 6.4: *Correction of the number of hits on the Y-track. In the lower distribution the average number of hits in the Y-layers is randomly reduced in number down to 98%, compared to the original GEANT simulation.*

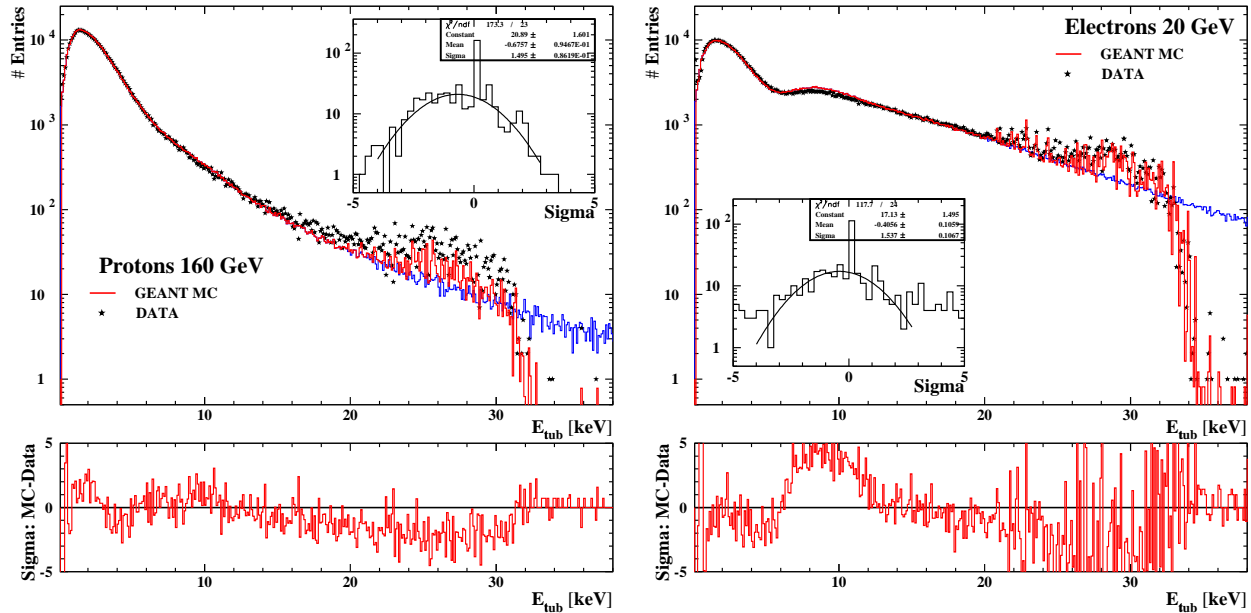


Figure 6.5: Comparison of Data and MC single tube energy spectra for a) 160 GeV protons and b) 20 GeV electrons. In both cases, the spectra without the implemented ADC cut-off, are plotted additionally.

All energy depositions in detector channels with a "zero" intercalibration factor are disregarded for the analysis. It is this introduction of "dead" channels, that represents the main reason to adapt the beam profile and position to that of the X7-beamline.

The ADC Cut-off The limitation of the dynamic range by the ADC is implemented, separately for each of the prototype's readout channels. This is done by introducing the 12bit ADC's overflow bin at 4096 channels, reduced by the appendant pedestal position for each channel. Scaled by the gas gain correction and intercalibration, the maximum resolvable energy is calculated, using the energy calibration factor derived from the test-beam data. Each simulated energy deposition in a single tube, exceeding the maximum value calculated for this channel, is set back to the overflow bin.

6.2.3 First MC Simulations

Using the such defined setup and the described GEANT software package, first MC simulations were carried out. Individually for each of the measurement runs, used in the final data analysis, the measuring conditions have been adapted to give the best agreement between data and MC.

Simulated as described and then analysed, in the way explained in the previous chapter, single tube energy spectra from hits on the track of selected single track events are accumulated. Figure 6.5 shows, exemplary for 160 GeV protons (left) and 20 GeV electrons (right), the comparison of these MC spectra with those derived from the measured data. Additionally displayed are the MC spectra without the ADC cut-off applied. In both cases, the MC spectra are normalised to the appropriate data entry number. For a detailed comparison, the error normalised difference of MC and data bin entry numbers is plotted, for each energy bin, and as the projection onto the y-axis. A perfect agreement of two spectra would lead to a projection peaking at 0 with a width of $\sigma = 1$.

The simulated proton spectrum is already in good agreement with that obtained from the measurements up to an energy deposition of $\sim 15 \text{ keV}$, as figure 6.5a shows. Above this energy threshold, the MC spectrum obviously features a smaller number of entries, amounting to a relative difference of 27.2 %, with respect to the data spectrum. As a matter of this fact, the peak of the projection plot is shifted to below zero and its width is broadened. On the other hand, the implemented ADC cut-off well reproduces the shape of the upper part of the data spectrum and only minor differences are still present in the spectra's most probable (MOP) values (0.7 %) and peak widths (1.0 %). The difference in the MOP peak position lies well within the errors on the energy calibration and gas gain correction, whereas the peak width seems to be slightly underestimated in the MC.

The comparison of the electron spectra, as displayed in figure 6.5b, alike reveals a similar good agreement in the shape of the cut-off region, and the peak position (0.1 %) and width (1.0 %) of the electron MC spectrum only slightly differ from those obtained from the measurement. Less drastic appears the percentally reduced number of entries (7.4 %) in the Landau tail, but the comparison of electron spectra additionally uncovers one of the reasons for this underestimation. It is the overestimated number of generated TR photons and the badly described shape of their energy spectrum in the Monte Carlo, that causes the discrepancy between the two electron spectra. Clearly visible is the surplus of entries in the TR peak and the slightly steeper declension to higher energies.

The described discrepancies between data and MC spectra show the necessity for optimisation, using the described GEANT 3.21 version as starting point.

6.3 MC Parameter Optimisation

For this optimisation process, several parameters are defined to adjust the simulation for best agreement to the measured data spectra and calculated proton rejection factors. This process is divided into two parts. In the first part, the spectra for the lowest proton energies are optimised. These lowest energies are chosen, because protons below 100 GeV do not generate transition radiation, which provides the opportunity to first focus, solely, on the ionisation energy loss optimisation. After applying these same dE/dx adjustments to the simulation of the electron measurements, the second step can separately concentrate on the optimisation of the TR generation. In both parts of this optimisation, several changes to the original GEANT supplements have been applied. Subject of this section is to introduce these changes and to explain their effect on the energy spectra.

6.3.1 dE/dx Adjustment

Cubic Interpolation As explained above, the recalculation of the ionisation energy loss in low density gases is based on the generation of a Poisson distributed number of particle interactions with the detector material. To each of those encounters an energy loss is assigned from so called energy transfer distributions, as displayed in figure 6.1, that exist tabulated in the supplementary GEANT code. In each case, plotting the first entry of each table versus the appendant Lorentz factor, results in a distribution of the typical "Bethe-Bloch" characteristics (see section 3.2.1 on page 26), as figure 6.6b shows. The original GEANT supplement now foresees a linear interpolation between values from those two tables with the appropriate γ factors, closest to that of the traversing particle.

This is changed to cubic interpolation, using the closest two values below and above the current particle's γ . Exemplary for a Lorentz factor between 100 and 300, this interpolation is shown in the figure and compared to the linear interpolation in the embedded plot. The relative difference between those two interpolation methods, at $\gamma = 200$, for example, amounts to 3 %, where this difference can account for a maximum of more than 11 %, around the minimum dip, at $\gamma = 4$.

Knock-on Electron Production In the simulation of ionisation energy loss, special care is taken of all single energy transfers above 10 keV, the lowest particle energy threshold that can be applied to any GEANT simulation. Particles that drop below this energy threshold are absorbed within the next GEANT step. For that reason, knock-on electrons (δ -rays) are generated only above this threshold.

The energy, transferred in such single encounters, is passed on to the electron, as its kinetic energy, E_{kin}^δ , which is emitted under the characteristic angle, θ , of δ -ray emission, defined by $\cos(\theta) = E_{kin}^\delta / (E_{kin}^\delta + 2 \cdot m_e)$ [35].

Primarily, knock-on electrons were generated out of all single energy transfers > 10 keV, which represents the main reason for the underestimated Landau tails of the spectra, shown in figure 6.5. This is because the emission of such low energetic (few keV) δ -rays is mainly perpendicular to the primary particle's direction, which reduces the amount of energy deposited on the primary particle track. Additionally, this simple implementation does not account for the shell electron's binding energy, especially it does not include the interaction with electrons from lower atomic shell levels. The accompanying radiation of escape photons reduces the kinetic energy of the emitted electron, which increases the probability for its absorption inside the same detector volume. As a matter of these facts, the number of generated knock-on electrons is reduced to 73 % and the remaining 27 % of all single energy transfers > 10 keV are treated as instant energy losses to compensate for the explained atomic physics phenomena. This approximate 3:1 ratio was chosen to give best agreement between the optimised MC and the data spectra, at proton energies below 100 GeV.

MOP Peak Position and Width Adjustment After the application of the two explained adjustments, the final step in this process is the adaptation of the simulated spectra's peak positions and widths. At first, the peak position is adjusted by applying a global energy scaling of 1.4 % to the total energy deposited in each read out channel. This same scale factor is used for all simulated proton energies. This scaling lies well within

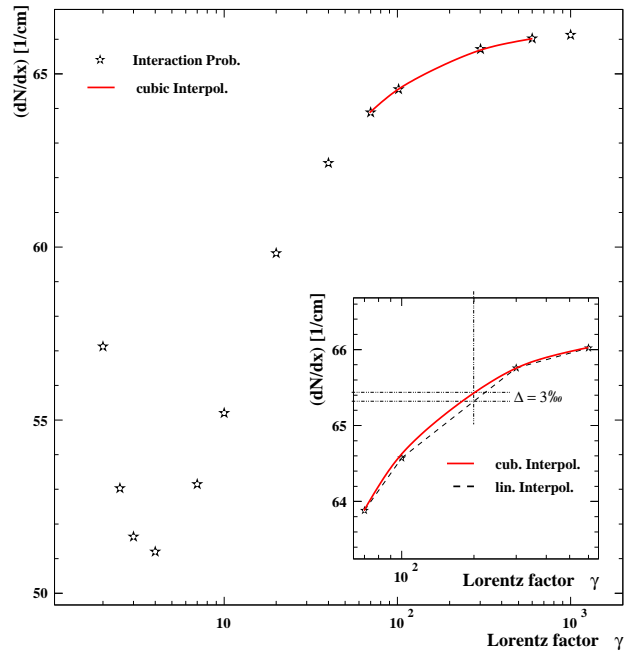


Figure 6.6: *Ionisation energy loss simulation. number of interactions per cm versus γ factor, Embedded: The comparison between linear and cubic interpolation.*

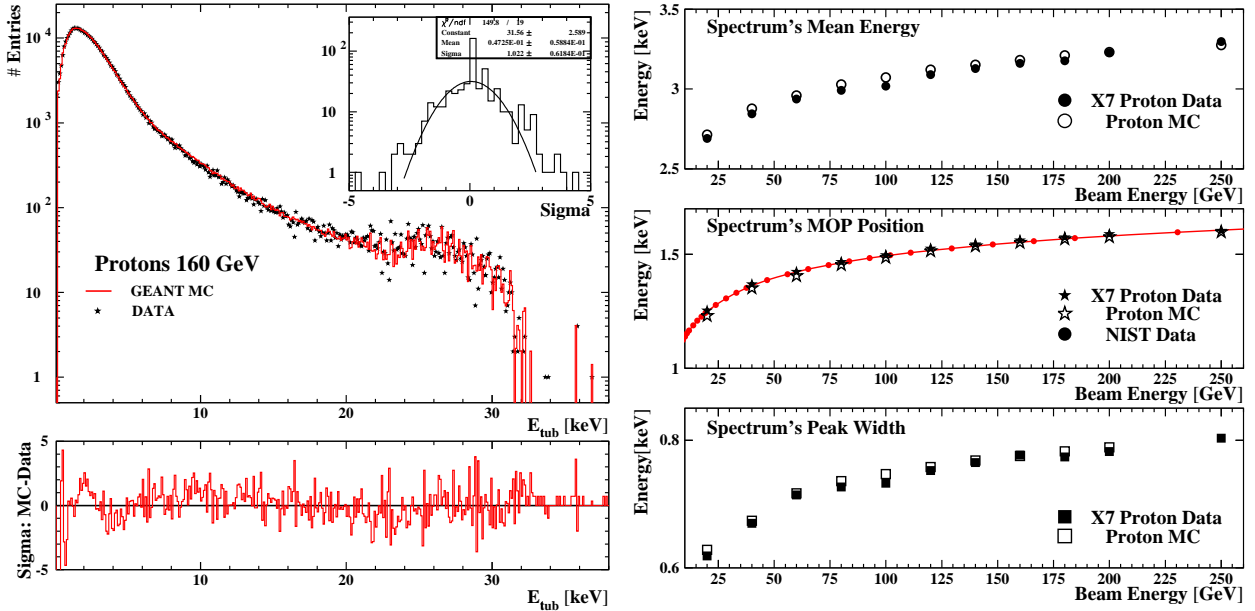


Figure 6.7: Comparison of Data and MC proton spectra. Left) Data and MC single tube energy spectra for 160 GeV protons; Right) Comparison of the spectra's mean energies, MOP positions and widths for all proton energies.

the uncertainties of the data energy calibration and gas gain correction. The widths of the various spectra, that seemed to be underestimated in the first MC, now agree without the necessity of scaling.

Comparison with Data With these changes applied, the comparison of the measured and MC simulated spectra of 160 GeV reveals no visible difference anymore, as shown on the left side of figure 6.7. The sigma distribution features only a minimal remaining structure, such that the peak of its projection no longer significantly deviates from zero and the width of its projection is very close to the nominal value of 1. The mentioned underestimation of the spectrum's tail is reduced down to 3.8 %. An even lower percentage of generated δ -rays would further decrease this numeric difference, but as well worsens the overall agreement of the two spectra's shapes. The right hand side of figure 6.7 displays the comparison of the fit results from the spectra of all available proton energies. The 3 displayed distributions show, from top to bottom, the comparisons of the spectra's mean energies, their MOP positions³ and peak widths. The distributions show the same good agreement, as indicated in the 160 GeV example, over the full range of proton energies.

After this successful adjustment of the dE/dx energy loss, these same adjustments are applied as well to the simulation of electron events. The second part of the adjustment process, can now concentrate on the changes to the generation of TR.

6.3.2 Adjustment of TR

The first step in this adjustment as well is the change from linear to cubic interpolation, in the same way as explained above. The effect here is even smaller than in the case of the dE/dx simulation. The TR adjustment procedure foresees the modification of the global number of TR photons and the overall shape of the TR energy spectrum.

³additionally plotted here is the distribution provided from NIST (see as well page 66).

This is done for a γ factor where the number of generated photons is saturated as well as the TR energy spectrum does not change anymore. As pointed out in the previous chapter (see page 68), this saturation is already reached for 20 GeV electrons ($\gamma=3.91 \times 10^4$) and for that reason the adjustment is carried out, referring to this electron data sample. Finally, the comparison of data and MC pion spectra are used to check the modifications made, for the low end of the Lorentz factor range, where pion and proton data were taken.

Numeric Reduction of generated TR Photons After applying the cubic interpolation, the number of generated photons is the first focus of this TR adjustment process. To alter this average number, the central value of the Poisson distribution, that calculates the number of TR photons in each GEANT step, is scaled. This scaling is used such, that the integral number of entries in the single tube spectrum, below the energy threshold⁴ of 6.5 keV, is equal to that from the data sample. In the final MC simulation, this scaling reduces the average number of generated photons down to 99 %. This reduction can be understood as the compensation for minor differences in the chemical composition, and/or average fiber diameter and spacing, of the used radiator, compared to the material, this GEANT supplement was originally optimised for.

The comparison of the such improved simulated electron spectrum with that from the data is displayed in figure 6.8. The peak positions and the numbers of entries below the 6.5 keV threshold now agree within a 3 % relative range. Still, the width of the dE/dx MOP peak and the general shape of the spectrum, in particular above 6 keV, need further adjustment. Especially, entries from the TR peak have to be redistributed mainly to higher energies. That means, the shape of the TR spectrum itself needs adjustment.

Adjustment of the TR Energy Spectrum In each GEANT step an energy is assigned to each of the generated TR photons, from the appendant distributions, as displayed in figure 6.2. In principle, to change the shape of the TR spectrum these probability distributions have to be modified. Such changes can be introduced by either changing the probability values or altering the appropriate energies. The latter has the advantage, that the application of these changes to the energy scale affects the TR photon spectrum in a similar way for the full range of Lorentz factors.

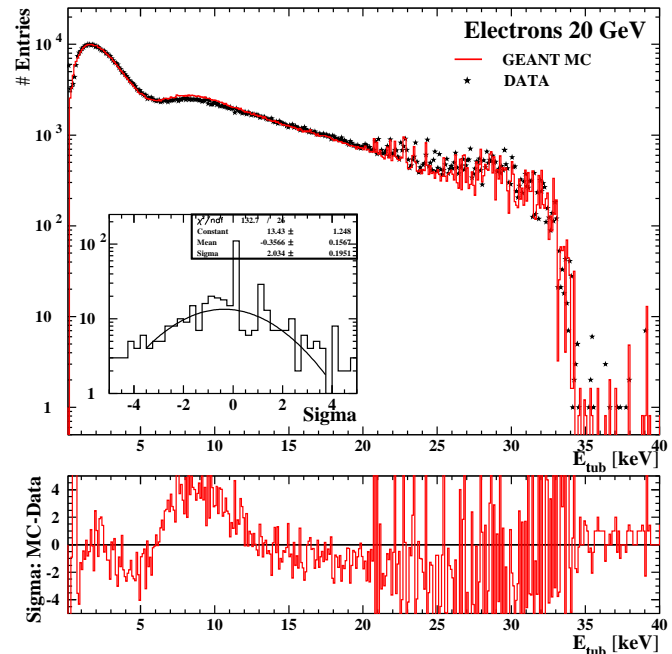


Figure 6.8: Comparison of Data and MC electron spectra. The MC spectrum has the dE/dx adjustment applied. The mean number of generated TR photons is reduced to 99 %.

⁴which is used to divide between the spectrum's dE/dx and TR region.

The difficulty is that a, at generation level, modified TR energy spectrum has to be altered such, that further appearing effects can be compensated. Two processes especially affect the absorbed TR spectrum, namely the photon re-absorption in the radiator and its detection in the proportional gas. Since this turned out to be a very complicated approach, and the only information available from the data is the detected TR spectrum, superimposed, even, by the dE/dx energy loss, the necessary tuning was carried out on this same detected spectrum's level.

The chosen tuning method uses a set of 4 straight lines to modify the energy of each detected TR photon. According to the definition of these straight lines the total TR energy range is divided into 4 sections, in which the appropriate linear function scales the TR photon energy. As displayed in figure 6.9, these linear functions are chosen such, that they continuously cover the full energy range. For the adjustment process, these linear functions were defined by a set of 6 energy parameters and 3 scale factors. The final parameter and scale factor values are mentioned at the bottom of the figure. Additionally plotted is the distribution from a simulated electron sample. The distribution shows the modified photon energy, E'_γ , plotted as a function of the original energy, E_γ . The sizes of the displayed boxes represent the number of entries in the appendant histogram bin. The indicated maximum relative difference, $(E_\gamma - E'_\gamma)/E_\gamma$, is $\sim 10\%$ at photon energies that already exceed the ADC cut-off. The maximal detectable difference stays below 6.5 %. For the best agreement with the data, the such modified TR energy spectrum is overall scaled by +2.4 % relative to the dE/dx MOP position.

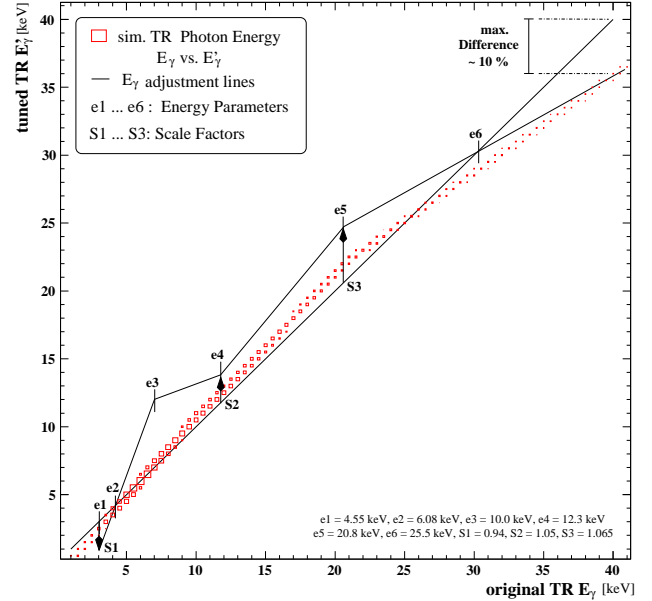


Figure 6.9: a) Comparison of detected TR photon energies before and after the tuning. Additionally plotted is the principal of the tuning along a set of 4 straight lines, defined by 6 parameters and 3 scale factors.

In the same way as before, this tuning can be understood as the compensation for minimal differences in the chemical composition and/or average fiber diameter and spacing, of the radiator used in the prototype, compared to the one, this MC simulation was originally optimised for. Even marginal differences in the named radiator parameters, can have remarkable effects on the TR energy spectrum [31].

Comparison with Data With all these adjustments and modifications applied, the final MC simulated 20 GeV electron spectrum, in comparison with that obtained from the related electron data sample, is displayed in figure 6.10a. The comparison shows a very good agreement between the data and MC spectra over the full energy range. Above the energy of ~ 21 keV the attached sigma plot features increased fluctuations from bin to bin, which is a direct result from the ADC cut-offs of those readout channels with a stronger limited dynamic range⁵.

⁵due to a higher pedestal position, for instance.

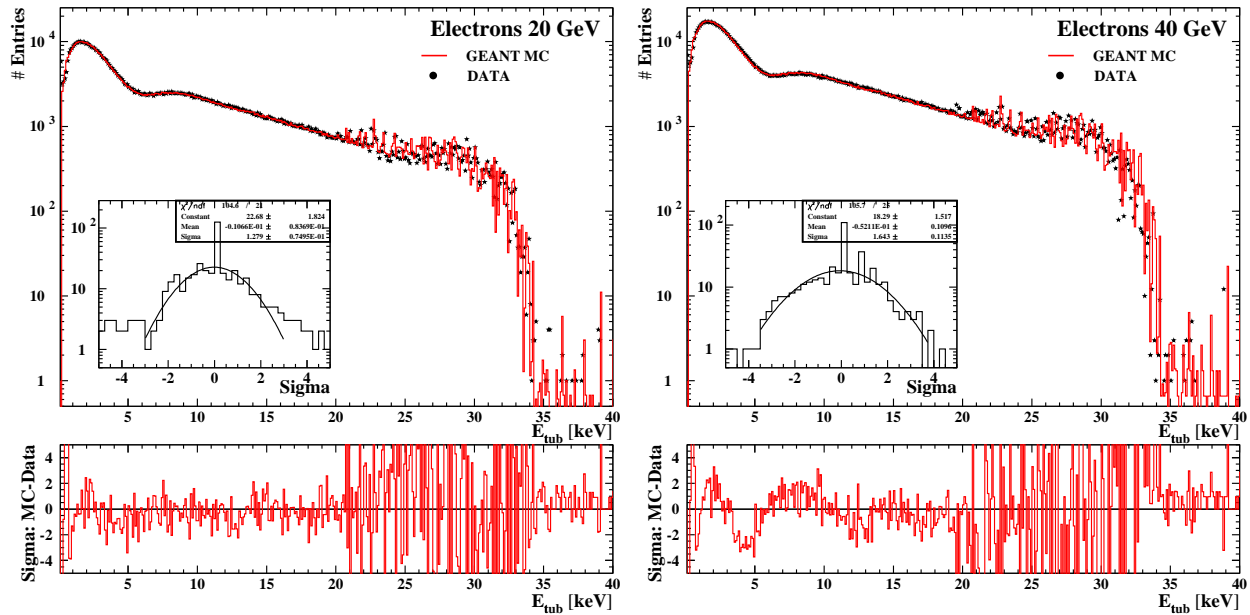


Figure 6.10: Comparison of the Data and final MC single tube energy spectra for a) 20 *GeV* and b) 40 *GeV* electrons.

Even though the introduction of the ADC cut-off is in general very satisfactory, the position can not be reconstructed that precisely to correspond, within the spectra's bin width of 0.1 *keV*, with those from the data. As a matter of that fact, the simulated overflow bins are shifted against those from the data. This causes, together with the high statistics in each bin, these high fluctuations in the sigma plot and a broadening of its projection, as additionally displayed in the figure, but still the projection's peak position agrees with zero, within the fit error. The comparisons of the proton spectra, as displayed earlier in this chapter, do not feature such big fluctuations in their appendant sigma plots, because of the much smaller number of entries and thus the far bigger statistical errors of the highest energy bins of the energy spectra.

A similar well visible agreement is revealed by the comparison of the 40 *GeV* MC and data electron spectra, as displayed in figure 6.10b. Only the additionally plotted sigma distribution discloses a clearly visible difference between the two spectra. This finds its reason in the lower gas density during the data taking. The different environmental conditions on the one hand affect the gas gain, which the data are corrected for, but as well influence the absorption probability, and thus can slightly alter the overall shape of the absorbed TR spectrum. A lower gas density reduces the absorption probability, especially for higher energetic photons, and thus softens the absorbed photon spectrum. The visible dip in the displayed sigma distribution indicates an increased number of data entries in the energy range between the MOP and TR peak, which represents the lowest energetic part of the TR spectrum. The supplementary plotted projection is due to this effect additionally broadened, but its peak does not significantly deviate from zero.

TR Threshold Check-Up A final test of these modifications turns the attention to the low γ factor threshold of TR generation. This threshold, around which all proton measurements were carried out, indicates the lowest Lorentz factor at which the spectrum of the generated transition radiation noticeably extends into the x-ray energy range,

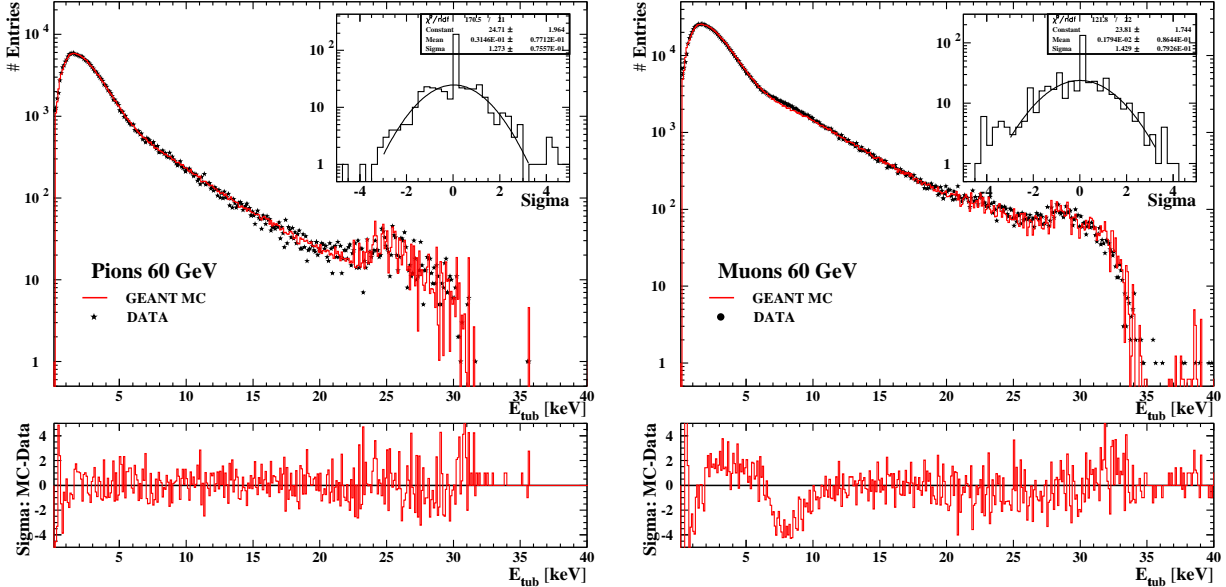


Figure 6.11: Comparison of the Data and final MC single tube energy spectra for a) 60 *GeV* Pions and b) 60 *GeV* Muons.

which makes the TR photons detectable. Since this directly affects the proton rejection, a closer look is given to this threshold. In this concern, the measured pion samples were of special interest for three reasons. First, the existing set of pion data (20-100 *GeV*) cover a larger γ -factor range, compared to the protons. Secondly, pions produce less secondary particles, as discussed at the end of the previous chapter, and thus provide the higher purity samples. The third reason is the independence of this final test from the proton samples, from which the e^-/p^+ separation powers are calculated.

Figure 6.11a shows such a comparison for 60 *GeV* pions. The two spectra show the same very good agreement as the protons, as presented earlier in this chapter. Neither the sigma plot features any visible structure, nor does its projection significantly deviate from the nominal zero. The 20, 40 and 80 *GeV*⁶ pion spectra feature the same good consistency, which leaves no doubt about the consistent simulation of TR over the full γ factor range, covered by the proton data.

As last of these tests, for the carried out adjustments, serves the 60 *GeV* muon spectrum, as displayed in figure 6.11b. In a similar way as the 40 *GeV* electron spectrum, the visible agreement between the MC and data spectra is good, only the sigma distribution features a clearly visible dip. The reason for this difference can be found again in the changed absorption probability due to the changed gas density, which the simulation is not corrected for. The final proton spectra are not significantly affected from the TR adjustment and the comparison displayed in figure 6.7 already represents the best agreement.

6.4 MC Rejection Analysis Results

After the satisfactory adjustment of the MC simulations and the finally good agreement of the single tube energy spectra, the most important part of these simulation studies was to repeat the rejection analysis for the MC simulated data and compare the results with those obtained from the measurements.

⁶80 *GeV* pion $\hat{=}$ $\gamma = 573 \hat{=}$ 538 *GeV* proton

The rejection analysis is performed as described in chapter 5. For that reason only the determined results are presented. In the following the term "hit" always refers to an energy deposition, of greater than 3 pedestal widths of the appendant prototype readout channel, on the reconstructed track.

Selection Cut Efficiency The first concern is given to the efficiency of the selection cuts. Since the MC provides the full information about the processes involved in the passage of each particle through the detector, a more detailed statement about the effectiveness of the chosen set of selection criteria can be given.

At first, a brief glance at the radiation lengths of the traversed materials is necessary. For the two plastic scintillation counters of 1 and 2 *cm* thickness, placed in front of the prototype, 7.1 % of a radiation length is calculated. This is in good agreement with the simulation, which generated 7466 interactions, in front of the detector, within 10^5 simulated 160 *GeV* proton events. Supplementary to this, the material of the prototype detector itself is calculated to an average of 7.7 % of a radiation length. As a result from that, on average 14.8 % of all traversing particles encounter interactions with the material in front of or inside the detector itself. The selection criteria⁷ as specified in table 5.1 (see chapter 5, page 61) select 79.7 % of the mentioned simulated proton event sample as single track events. That means a 93.5 % single track selection efficiency. Simulated 20 *GeV* electron events show a smaller number of generated interactions in front of the detector (3308 out of 10^5) and as a result from that a larger total number of selected single track events (85648). The resulting single track efficiency of 95.1 % only slightly differs from the presented proton result.

6.4.1 Cluster Counting Analysis

The Cluster Counting method is based on the counting of those hits, in each event, above a certain energy threshold, E_{cut} , referred to as "TR-Clusters". This E_{cut} is defined such that 90 % of all electron events are selected by the applied Hit-Cut (H_{cut}), which requires a minimum number of "TR-Clusters" for an event to be selected "electron-like". From those proton events, that are selected by the applied same H_{cut} , the proton rejection is calculated (see also section 5.3.1). Applying this method to MC generated 20 *GeV* electron and 160 *GeV* proton samples results in the comparison as displayed in figure 6.12. In this figure the entry numbers of the derived MC distributions are scaled to those from the appropriate data samples. The comparison of the electron distributions discloses a shifted maximum of the data distribution to higher $N_{TR-Clst}$ values. This is the direct result of the additional hits in the X-layers due to the electrical crosstalk, as discussed earlier in this chapter (see page 84).

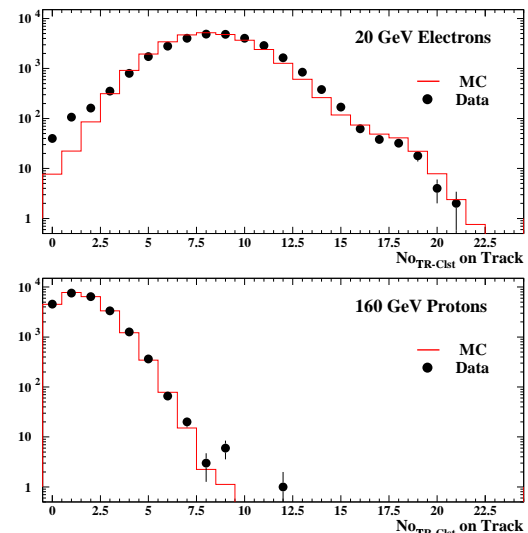


Figure 6.12: Comparison of MC and Data H_{cut} distributions for 20 *GeV* electrons and 160 *GeV* protons.

⁷except the cuts on the Čerenkov Counters

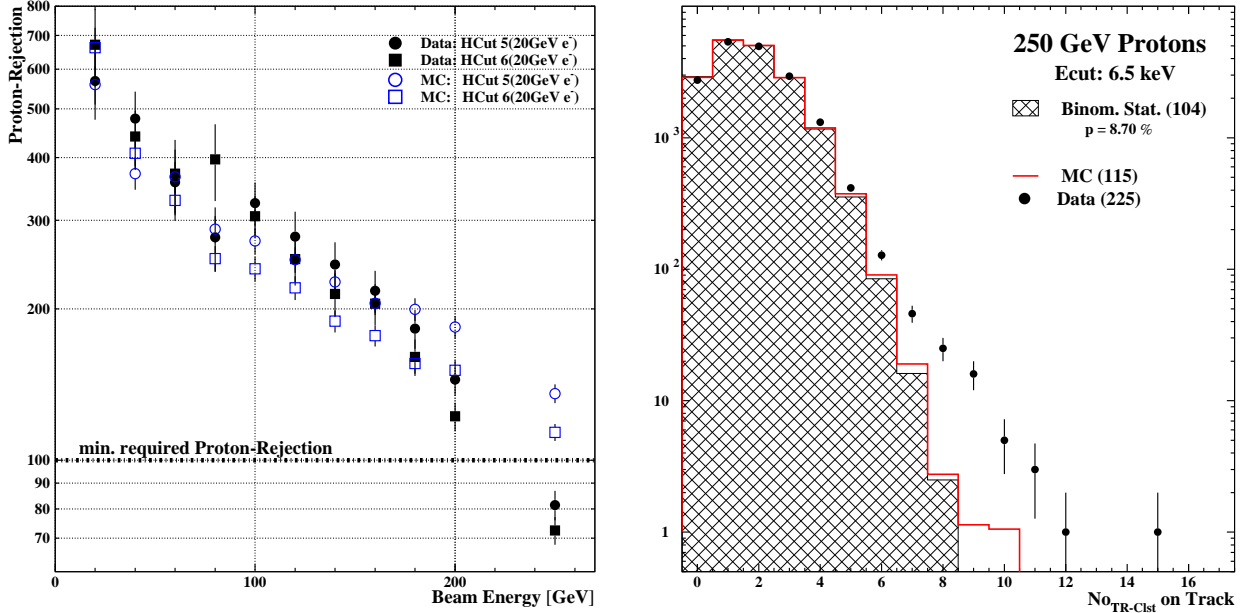


Figure 6.13: a) MC and data proton rejections, derived from Cluster Counting method, as functions of beam energy; b) Comparison of the MC and data proton $Hcut$ distributions. Additionally plotted is the related distribution, derived from binomial statistics. The numbers, given in the brackets, indicate the entries above $Hcut$ 6.

This difference instantaneously reduces the expectation for the MC proton rejection. On the other hand, the two proton distributions are in very good agreement, especially as the result from the adjustment of the hit number on the Y-track (see p. 84). From these two distributions the proton rejection factor is calculated as the number ratio of entries in the full distribution to those in the bins ≥ 6 ($Hcut$ 6). This can be repeated for all available proton energies and the derived rejection factors plotted as a function of beam energy. Figure 6.13a compares these "rejection vs. beam energy" distributions for data and MC.

Comparison of Rejection Factors The two displayed distributions show an agreement within the statistical errors upto a beam energy of 180 GeV , but as well show the expected systematically reduced rejection for the MC distribution at lower proton energies. Despite this difference between data and MC, the displayed comparison features another clearly visible effect. While the data distribution shows the expected exponential reduction, the MC distribution features a more linear behaviour as a function of beam energy. Consequently, the MC and data distributions intersect and on average differ by 62% at 250 GeV beam energy. As already discussed in the previous chapter (see page 70) and indicated again in figure 6.13b, the 250 GeV proton data $Hcut$ distribution has a significantly increased number of entries, compared to the related distribution derived from binomial statistics. On the other hand, the appendant MC distribution well complies with this prediction from statistics.

That means, for a small number of events the measured data show an increased probability for hits to occur, that exceed the ' $Ecut$ ' threshold. Secondary particles, emitted in the primary particle's forward direction, would deposit additional energy in some detector tubes on the track and explain the increased number of high energetic hits. The type of interaction that generates such secondary particles has to be underestimated in the MC.

The analysis was repeated for the 40 *GeV* electron reference sample, with an, on average, even better agreement between the MC and data distributions and the same $\sim 60\%$ relative difference of proton rejection factors at 250 *GeV* beam energy. For means of clarity only, this comparison is not displayed. The mentioned better agreement is based on the reduced extra hits⁸ in the X-layers of the used 40 *GeV* data runs. The direct result from that is the better consistency of the MC and Data electron *Hcut* distributions and thus the derived proton rejection factors are in better agreement.

6.4.2 Likelihood Analysis

The likelihood method is making use of the full information contained in each hit. For that reason, the electron and proton single tube energy spectra are normalised to an integral of one and then used as probability distributions for each hit. The likelihood, for an event to be "electron-like", is calculated from the probabilities of each hit on the reconstructed track (see also page 73). Figure 6.14 compares the MC and data likelihood (Def.I) distributions derived from 20 *GeV* electron and 250 *GeV* proton samples. In the chosen form of display, a small $-\ln(L_e)$ value indicates an electron-like event. The comparison reveals a similar agreement between data and MC likelihood distributions as for the Cluster Counting method. While the proton distributions very well agree in the overall shape, the maxima of the two electron distributions are slightly shifted against each other. The effect of additional hits, due to crosstalk, is still noticeable in the displayed distributions but of less importance, since all three likelihood definitions correct for altering numbers of hits. The uppermost part of the electron and the lowermost part of the proton data distributions feature a few additional entries compared to the appendant MC distributions. The additional entries in the proton data distribution have their origin in the explained lack of secondary particle production in the MC. Those additional entries in the electron data distribution are mainly gathered in the region of high likelihood values, which, in general, indicate "proton-like" events. So it is obvious to assume, that these entries are generated by heavier particles, such as pions, that exist as a marginal contamination in the electron beam. A pion contamination of 6.5 ‰ would already explain the displayed excess of entries⁹. The comparison of the 40 *GeV* electron distribution, that features a similar shape and fraction of additional entries, in this uppermost part, provides a confirmation of this explanation.

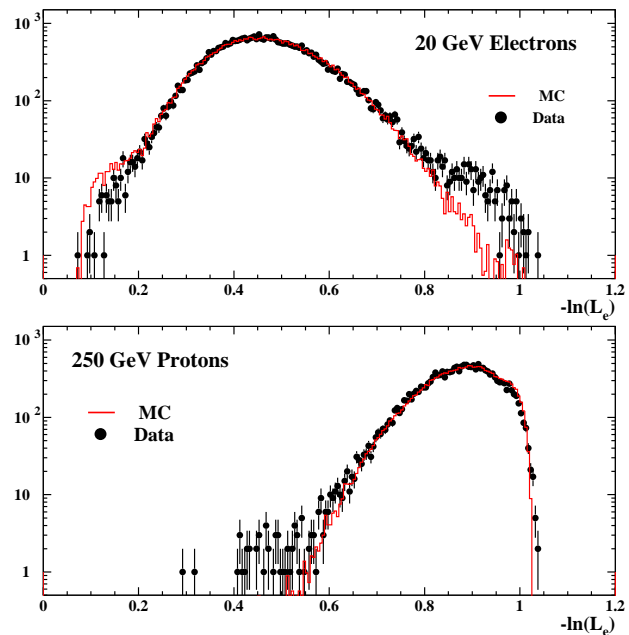


Figure 6.14: Comparison of MC and data definition I likelihood distributions separately for 20 *GeV* electrons and 160 *GeV* protons.

⁸due to the above discussed electric crosstalk

⁹The purity of the X7 electron beam is specified as $\gtrsim 99\%$ [61].

Rejection versus Beam Energy This same procedure has been applied to simulated proton samples of all available data energies. In figure 6.15 the resulting MC proton rejection factors, from likelihood definitions I and II, are displayed as functions of beam energy, in comparison to those distributions derived from the measured data. As a matter of the close concordance of the results from 20 and 40 *GeV* electron references, the clarity is conserved and all four distributions from data and MC are displayed. All 4 distributions feature a very good agreement up to a beam energy of 140 *GeV*. Beyond this proton energy the data and MC distributions start to diverge from each other. The first statistically significant difference is seen at 200 *GeV* particle energy and at 250 *GeV* the comparison reveals an average relative difference of 285 % between the results derived from measurement and simulation. In the same way as before, the MC distributions seem to follow straight lines as functions of beam energy, while the data show the expected exponential behaviour.

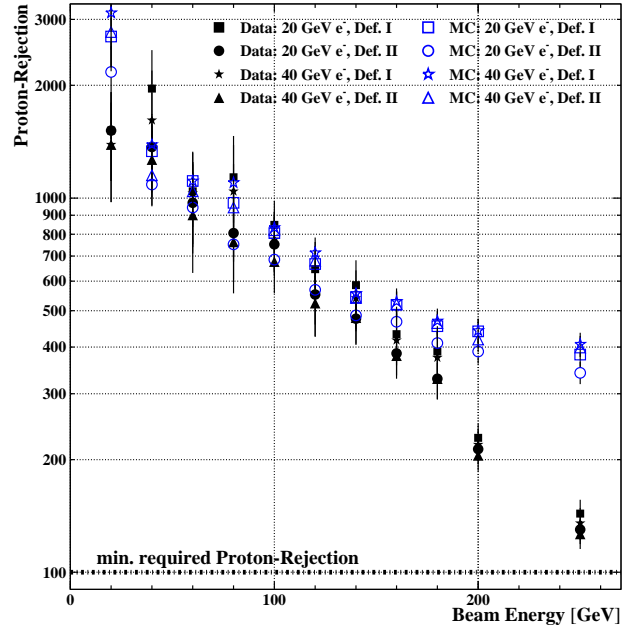


Figure 6.15: *MC and data proton rejections, derived from definition I likelihood, as functions of beam energy.*

Rejection versus γ Factor A first indicator for the described discrepancy to be of other origin than an underestimated generation of transition radiation, is already given by the very good agreement of the simulated and measured pion energy spectra. The pion rejection analysis can provide the necessary information to exclude TR as the reason for this discrepancy. For that reason the pion and muon MC rejection factors are also calculated and compared to those from the measurements. All rejection factors, derived from definition I likelihood and the 20 *GeV* electron reference, are plotted as functions of their appropriate Lorentz factors and summarised in figure 6.16. Supplementary, this figure shows the appendant data distributions, from figure 5.22 at the end of the previous chapter, to allow a direct comparison. The displayed comparisons for pions and muons show the same very good agreement, between the data and MC rejection factors, as already present in the comparison of the single tube energy spectra.

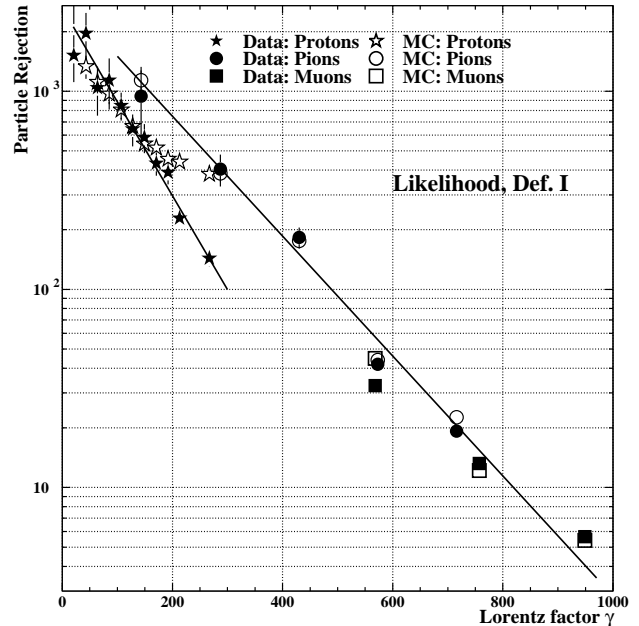


Figure 6.16: *MC and data particle rejection factors versus Lorentz factor, γ .*

This confirms the compatible MC generation of transition radiation, in a Lorentz factor range that covers even more than just the appropriate proton measurement range. A second confirmation lies in the matching rejection factors, derived from 60 *GeV* muons and 80 *GeV* pions, since their Lorentz factors are almost the same¹⁰. The mentioned remarkable discrepancy of the proton rejection factors remains the only difference.

That means, this discrepancy can only be explained by the suggested additional production of secondary particles, emitted in the primary particle's forward direction. Such secondaries mainly deposit additional dE/dx energy in detector tubes on the track, but occasionally this can be accompanied by additionally absorbed TR photons. For that reason, a process has to be found, that especially favours protons (at high energies ($\gtrsim 150$ *GeV*)) to produce such secondaries, and is underestimated in the GEANT 3 simulation.

The total cross section for pp interactions is already a factor of ~ 1.5 bigger than that of πp [36], but this is well known and, for that reason, precisely simulated in the standard GEANT software package. An accomplished scan of simulated pion and proton events resulted in a ratio of hadronic interactions $\frac{\sigma_{pp}}{\sigma_{\pi p}}$, that confirms this expectation.

6.4.3 A possible Solution: Diffractive Proton Dissociation

The solution to this dilemma could be so called diffractive interactions that extend the total interaction cross section especially for pp interactions. In these processes, secondary particles, like pions, are produced, that are emitted in the forward direction of the incident particle. Diffractive interactions mainly occur in high energetic pp or $\bar{p}p$ collisions and are of little importance for πp interactions in the energy region of interest ($E_\pi \lesssim 40$ *GeV*). They effectively occur above ~ 100 *GeV* particle energy and might well be underestimated in the GEANT 3 software (standard parameters) [67]. This is because, occurring diffractive processes cannot be studied in collider experiments, such as at LEP (CERN), which the GEANT 3 software was mainly developed for.

One of the simplest diffractive models is that of the single diffractive dissociation of either the projectile or the target proton in such an encounter. In such processes small momentum transfers and low multiplicity of the generated secondary particles are preferred. In the diffractive reaction

$$p + p \Rightarrow (p + \pi^+ + \pi^-) + p \quad (6.1)$$

one pair of secondary pions is produced with a cross section of $\sigma_{proc.} = (330 \pm 100) \mu b$, at $\sqrt{s} \approx 45$ *GeV*, saturating at higher s [68].

In the following the displayed reaction 6.1 shall be used for a cross check of the proposed hypothesis. According to this, $\pi^+\pi^-$ pairs are produced with fixed energies¹¹ of 40 *MeV*, each, and emitted into the forward direction of the primary proton. The reaction cross section was adjusted such that the discrepancy between the simulated and measured rejection factors is resolved. The cross section value that suits this demand for the 250 *GeV* proton energy works out to be as high as $\sigma_{proc.} \approx 15$ *mb*. With respect to the total pp cross section of $\sigma_{tot}^{pp} \approx 40$ *mb* (at $\sqrt{s} \approx 20$ *GeV*), this denotes a relative extension of ~ 38.5 %. This contribution is programmed to diminish exponentially with decreasing proton energy and is set to 0 below 100 *GeV* particle energy.

¹⁰80 *GeV* pion $\hat{=}$ $\gamma = 573 \approx 568 \hat{=}$ 60 *GeV* muon

¹¹The estimated average energy E_π necessary to pass 4 detector layers before its re-absorption.

A 250 GeV proton sample generated with the so adjusted MC, in the following referred to as "MC2", features a single track efficiency reduced by only $\sim 4\%$ compared to the original MC sample. This reduction is due to further interactions of the additional pions with the material, producing for instance δ -rays. Over the full energy range, the generated MC2 proton energy spectra do not differ significantly from those presented earlier in this chapter. In contrast to that, the MC2 likelihood distribution for 250 GeV protons, as displayed in the embedded plot of figure 6.17, visibly differs from the "original" MC distribution, as additionally displayed. It contains additional "electron-like" entries that enhance the agreement to the data distribution. This displayed good compliance is directly related to the coinciding data and MC2 rejection factors at 250 GeV proton energy. This holds in the same way for the total proton energy

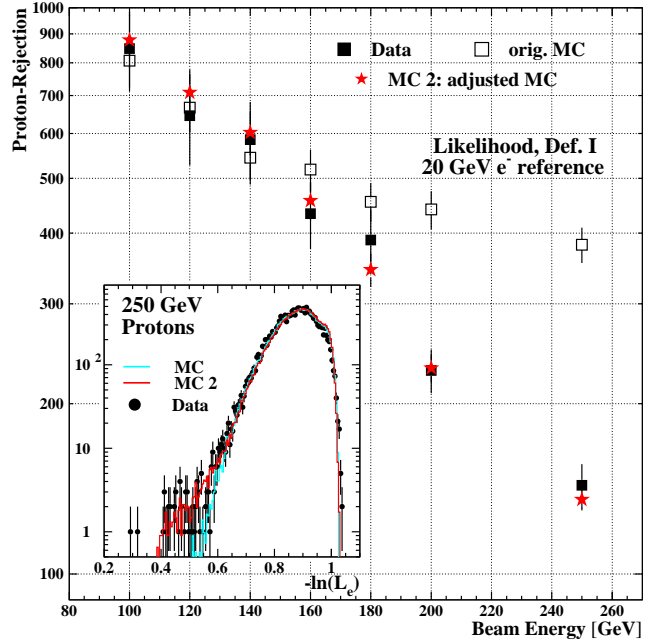


Figure 6.17: *Adjusted MC (labeled "MC2") rejection factors as a function of beam energy in comparison to the data distribution. Embedded: Comparison of the Likelihood distributions from 250 GeV proton data and MC2.*

range, as displayed in figure 6.17 for proton energies above 100 GeV. The displayed distribution is related to the likelihood definition I and the 20 GeV electron reference.

The outcome of the accomplished test supports the made assumption. This simple implemented model is able to resolve the formerly present discrepancy between the rejection factors within the given constraints of, for example, leaving the energy spectra unchanged. Unsatisfactorily remains the fact that the necessary cross section for the process exceeds any reasonable value (an extension of $\lesssim 5\% \sigma_{tot}^{pp}$). Partly this may find its explanation in the simplicity of the used model with a fixed pion energy and multiplicity, where only $\sim 50\%$ of the generated pion pairs cause these specific events to be selected "electron-like". Yet another reason can be found in the variety of such diffractive processes that exist and have all been approximated by only one reaction (6.1) within this simple model. Still, even in the best case scenario, the necessary $\sigma_{proc.}$ exceeds any reasonable value by more than a factor of 3.

On the other hand, a minimal uncertainty about the purity of the data proton samples cannot be excluded, even though all found evidence seem to rule out a possible pion contamination in the proton samples. Nevertheless, the found evidence appeared to be strong enough to favour the first explanation.

Since any other proposed solution failed to follow suit or even to improve this drawback, the described model will be used for subsequent AMS02 full detector MC simulation studies. For a deeper understanding of the assumed real processes involved, additional measurements are required that have not been carried out during the beamtests in 2000.

Chapter 7

Conclusion

From ancient history on, mankind has been fascinated by the view of the night sky. More and more sophisticated technologies have improved our understanding of the heavens, in particular, and the universe, in general. Photon detectors, such as the Hubble Space Telescope, have taken pictures from even far remote interstellar objects and measured photon energy spectra from very low (infrared) up to extremely high, such as γ -ray, energies. The deeper we look into space, the further we also look back in time, and the more we learn about the evolution of the universe. One of the great achievements on this sector was the discovery, that our universe expands and as a direct implication from that, that it was given birth in a tremendous explosion, referred to today as the *Big Bang*. The afterglow of this Big Bang is known today as the cosmic microwave background radiation.

Supplementary to the detection of photons, a flux of high energetic charged particles, the so called cosmic radiation, strikes earth's atmosphere, that could teach us even more lessons about the universe. However, we still know very little about the primary cosmic radiation, because these charged particles interact with earth's atmosphere and thus measurements, to find out more about these cosmic rays, have to be carried out in space. The International Space Station provides the facility for a magnetic spectrometer to be operated under such space conditions for long term measurements.

The Alpha Magnetic Spectrometer (AMS) Experiment, for that reason, will be the first large acceptance particle detector to be operated in space. It will make use of state of the art detector technology for the detailed exploration of the cosmic rays. During the proposed 3 years exposure to the cosmic rays on board the ISS, AMS will especially search for an admixture of antimatter particles ($Z \geq 2$) and pursue precise positron spectroscopy.

The search for antimatter is trying to find an answer to the question about the fate of primordial antimatter. According to the Standard Model of particle physics, antimatter must have existed in equal amounts as matter, in the early universe, but no evidence, for its existence today, has been found. Positron spectroscopy is carried out to find evidence for a possible supersymmetric component of the dark matter in the universe. In order to do so, the positron spectrum has to be measured with high precision to be able to identify a surplus of positrons, generated in potential Neutralino decay or annihilation processes.

Taking into account the flux ratio of protons and positrons ($\sim 10^4$) in the cosmic radiation, the rejection of protons against positrons has to be better than 10^6 , to sample a precise energy spectrum of positrons. For that purpose, the AMS experiment is making use of an Ecal and supplementary to this a Transition Radiation Detector (TRD) that will provide a proton rejection $\gtrsim 10^2$ up to 250 GeV particle energy.

Mounted onto the upper flange of the AMS superconducting magnet, the TRD will comprise 328 proportional chamber modules, arranged in 20 layers and covered with 22 mm thick polypropylene fiber material. Each of the modules consists of 16 single tubes, with 6 mm diameter, filled with a Xe/CO_2 (80/20) gas mixture and a central gold plated tungsten anode wire (\varnothing 30 μm). For the inherent stability of the TRD subsystem the modules are held in a conical octagon support structure. In order to test this detector design for its suitability, a final 20-layer-prototype was built in Aachen and subjected to 2 high energy beamtests at CERN in summer 2000. The two beamtests were carried out at the X7 beamline, using two threshold Čerenkov counters, and at the H6 beamline, using a differential Čerenkov counter, to directly trigger on proton particles. During these beamtests a total of ~ 3 million events from p^+ , e^- , π^- and μ^- particles were recorded.

The work at hand, was concerned about the analysis of the data, taken during these beamtests, and the reproduction of the deduced data results in GEANT Monte Carlo simulations.

The Prototype The prototype has been built with 16 vertical and 4 horizontal layers. Each of the layers consisted of 2 40 cm detector modules interleaved with 20 mm radiator material. One half of the prototype was used for final radiator tests, while in the second half the proton rejection measurements were carried out. This second half was equipped with the radiator material proposed for the final AMS TRD. The gas was supplied sequentially through chains of 6 or 8 modules and the readout was organized in a similar way, as in the final TRD. During the beamtests, 1 absolute and 6 differential pressure as well as 2 temperature sensors were used to monitor changes in the environmental conditions.

Data Analysis After pedestal correction, the inter- and absolute energy calibration of the 640 readout channels, were derived from muon runs and ^{55}Fe measurements, respectively, recorded throughout the entire X7 beamtest. Gas gain corrected and inter-calibrated, a twofold linear regression was applied to reconstruct the particle track and according to this, a set of criteria was employed to select single track events.

The **Rejection Analysis** was carried out in two ways.

1. **Cluster Counting Method** This method is counting the number of hits above a certain energy threshold, E_{cut} , on the reconstructed track, requiring a minimum number, referred to as H_{cut} , of such hits, for an event to be selected "electron-like". For a given H_{cut} the E_{cut} is chosen such, that 90 % of the e^- events are selected. The proton rejection is calculated as the number ratio of the total single track proton events to those selected by the applied same H_{cut} . The deduced rejection factors range from (625 ± 117) at 20 GeV beam energy up to (80 ± 5) at 250 GeV.
2. **Likelihood Method** This second method is making use of the full information of the energy in each of the hits on the track. For that reason the single tube energy spectra of protons and electrons are normalised to an integral of 1 and then used as $P_{e,p}$ probability distributions. According to these distributions, the likelihood L_e for an event to be "electron-like" is calculated from the following definition

$$L_e = \frac{P_e^{mean}}{P_e^{mean} + P_p^{mean}} \quad \text{with} \quad P_{e,p}^{mean} = \sqrt[n]{\prod_{k=1}^n P_{e,p}^k(E_{dep})} \quad \text{and} \quad n = \#hits$$

From the requirement of a 90 % electron efficiency the Likelihood Cut ($LHcut$) is defined. In the same way as before, the proton rejection is deduced as the number ratio of the total single track proton events to those selected by the applied same $LHcut$. The such derived proton rejection factors range from (1429 ± 408) at 20 GeV beam energy up to (143 ± 12) at 250 GeV , as displayed in figure 7.1.

3. **Pion Analysis** Pion events in the energy range between 20 and 100 GeV were recorded and the described rejection analysis repeated for the available pion data. The rejection factors derived from likelihood analysis range from (1000 ± 400) at 20 GeV beam energy up to (19.2 ± 0.7) at 100 GeV , as also displayed in figure 7.1.

This described rejection analysis was carried out, using the 20 GeV electron sample as reference. The repeated analysis, using a 40 GeV electron reference sample, reproduced the derived rejection factors, within the statistical errors.

The comparison of the results derived from proton and pion measurements, taken at comparable Lorentz factors, reveals a discrepancy of more than a factor of two at the highest measured proton energy. A possible explanation for this discrepancy is an increased number of proton events with produced secondary particles, emitted into the forward direction of the proton. The GEANT3 simulation studies finally suggest diffractive pp interaction processes to be responsible for this increased number of events, with produced secondary particles. These secondaries mainly deposit additional dE/dx energy loss in the detection gas, occasionally accompanied by the absorption of a TR photon.

Monte Carlo Simulation The GEANT 3.21 software package, improved in the simulation of dE/dx energy loss, and additional supplements to generate and detect transition radiation, first implemented by members of the HERA-B Collaboration, were used to reproduce the beamtest results. The detector characteristics, like the geometry and part of the readout electronics, as well as the beamtest conditions, have been introduced into the GEANT as precisely as possible. Supplementary to this, several adjustments to the above mentioned, original GEANT supplements, have been accomplished to give the best agreement to the measured energy spectra.

The such optimised "original" MC simulation is capable to reproduce the proton energy spectra over the full range of proton energies. The rejection factors of protons¹, up to a particle energy of 160 GeV , and those of pions, over the full pion energy range, very well agree with those rejection factors derived from the measured data.

¹derived from the "original" MC (not shown in the figure).

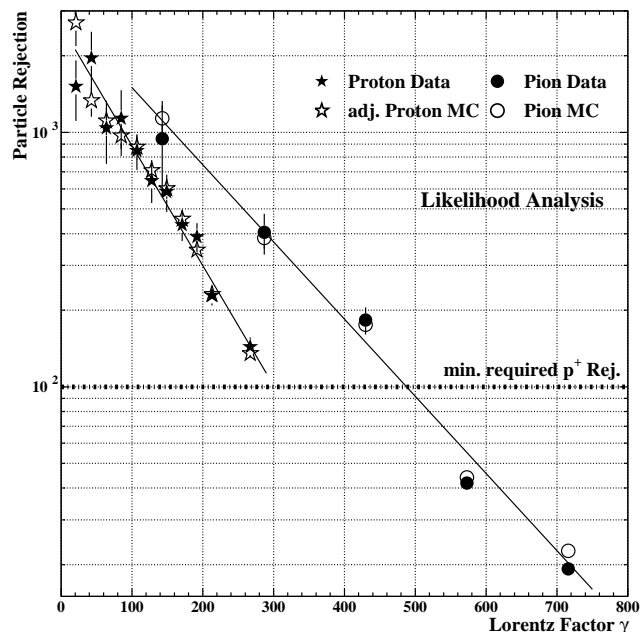


Figure 7.1: *MC and Data particle rejection factors versus Lorentz factor γ .*

The disagreement between data and "original" MC proton rejection factors above the energy of 160 GeV amount to more than a factor of 2 at 250 GeV particle energy. This discrepancy is believed to be related to an underestimated interaction cross section for single diffractive dissociation of protons in pp interactions. Whereas diffractive πp interactions, especially in the energy region of interest ($E_\pi \lesssim 40 GeV$), hardly ever occur, which as well explains the discrepancy between proton and pion rejection factors calculated from the data at equivalent Lorentz factors.

A simple diffractive model implemented into the GEANT 3 software was able to resolve the mentioned discrepancy and thus supports the made hypothesis, even though the necessary cross section $\sigma_{proc.}$ exceeds any reasonable value. The final agreement between the data and MC rejection factors achieved by this simple model is displayed in figure 7.1. Any other proposed solution failed to follow suit.

Acknowledgement

My first thanks goes to Prof. Dr. S. Schael for the interesting and challenging assignment of this work and all the confidence he had in me to work on this project without his permanent surveillance.

My special thanks goes to Prof. Dr. W. Wallraff, who's kind and competent supervision i could always count on. Whenever my "frustration tolerance" had reached its limit, it was often especially his encouragement that gave me the necessary strength to carry on. Additionally, i want to thank Prof. Wallraff for his detailed revision of the manuscript to this thesis, no matter that his time has always been strictly limited.

Furthermore i want to thank Dr. Th. Siedenburg and Dr. Th. Kirn for their support and advice throughout the whole scientific work and the revision of the manuscript. Especially Th. Siedenburg was always available for fruitful discussions about the analysis and MC simulations, whenever i asked him for advice. Not even seldom he extended his working hours for our knowledge exchange.

Another special thanks goes to Dr. M. Fernández García, who has become a friend in the final year of my PhD thesis. He has always been there to listen and advice me in scientific as well as personal matters. With his kind and straightforward character he was able to make the months of writing the thesis more tolerable and to cheer me up whenever necessary. I am as well grateful for his detailed revision of the manuscript and his profound proposals for improvements.

Yet another thanks i owe Dr. H. Fesefeldt and Dr. V. Saveliev, who both helped and supported me with their specific knowledge of the GEANT software and the mentioned TRD supplements.

I as well want to thank all my co-workers in the I. Physikalisches Institut b for the friendly working atmosphere, here especially, in alphabetical order, R. Brauer, C.H. Chung, F. Doemmecke and formerly V. Vetterle, with whom i shared my office. The workers in the mechanical and electronics workshops deserve a special thanks for their work during the building stage of the prototype.

The most grateful i am for my family. With their love and advice my parents have always been there for me, believing in me and my abilities. Their personal support and education represent the basis for what i am today. I thank my sister for being one of the best friends that i have.

List of Figures

1.1	The two spiral galaxies NGC 2207 and IC 2163	1
2.1	The AMS-Detektor on board the ISS	6
2.2	<i>CMBR Spectrum \Rightarrow 2.73 K blackbody</i>	7
2.3	The development of the universe from the Big Bang until today.	8
2.4	<i>Rotational velocity distribution from M33 galaxy.</i>	10
2.5	Two SUSY fit results to the HEAT and AMS01 data	12
2.6	Positron fraction as expected after one year of AMS on the ISS.	13
2.7	AMS-02 configuration on the ISS	15
2.8	Momentum resolution of the Silicon-Tracker.	16
2.9	The superconducting magnet.	16
2.10	Anti-counter system.	17
2.11	Time of flight system.	17
2.12	<i>Ring imaging Čerenkov counter.</i>	18
2.13	The electromagnetic calorimeter.	18
2.14	The transition radiation detector with the M-support structure	19
3.1	<i>Electric charge in front of a perfectly conducting surface.</i>	22
3.2	<i>A charged particle traverses a stack of radiator foils.</i>	23
3.3	<i>Transition Radiation Yield</i>	25
3.4	<i>Energy loss according to Bethe-Bloch</i>	28
3.5	<i>Schematic illustration of the photoelectric effect.</i>	29
3.7	<i>Schematic illustration of the Compton effect.</i>	29
3.6	<i>Absorption coefficient</i>	30
3.8	Schematic illustration of a proportional chamber.	31
3.9	<i>The Effect of a wire displacement on the gas amplification.</i>	32
3.10	<i>AMS TRD mounted on the upper flange of the magnet.</i>	32
3.11	<i>Straw wall cross section.</i>	33
3.12	<i>a) Cross section and b) photo of a straw module.</i>	34
3.13	<i>The front end electronics scheme.</i>	34
3.14	<i>TRD electronics design.</i>	35
3.15	<i>Photo of an UFE board.</i>	35
3.16	TRD gas supply system.	36
3.17	3D view of the TRD octagon support structure.	37
3.18	<i>Modal Analysis: FEC and Verification from Measurement</i>	38
3.19	<i>Thermal model of the TRD subsystem.</i>	39
3.20	The 8 thermo-cycles of a thermo-vacuum test.	39

4.1	<i>Building sequence for the straw modules.</i>	42
4.2	<i>Schematic illustration of the Preview Test.</i>	42
4.3	<i>Schematic illustration of the Serial Test.</i>	43
4.4	<i>^{55}Fe and ^{241}Am photon spectra.</i>	44
4.5	<i>Homogeneity distributions for 3 prototype modules.</i>	45
4.6	<i>Gas gain in three different gas mixtures.</i>	46
4.7	<i>Gas gain as a function of gas density.</i>	47
4.8	<i>Gas gain as a function of E_γ.</i>	48
4.9	<i>Zoom into the layer structure.</i>	50
4.10	<i>Photo of the 20-layer TRD prototype.</i>	51
4.11	<i>Principle of the prototype's gas supply system.</i>	52
4.12	<i>Gain linearity of the VA chips.</i>	53
4.13	<i>General beamtest set-up and trigger logic.</i>	55
4.14	<i>Threshold Čerenkov detector efficiencies.</i>	56
4.15	<i>Differential Čerenkov counter efficiency.</i>	57
5.1	<i>Pedestal width distribution for all 640 channels.</i>	60
5.2	<i>Principle of the track reconstruction in the vertical layers.</i>	61
5.3	<i>Single tube energy spectrum.</i>	62
5.4	<i>Inter-Calibration table from muon runs.</i>	63
5.5	<i>Errors on the inter-calibration factors.</i>	63
5.6	<i>Gas gain correction derived from muon runs.</i>	64
5.7	<i>Gas gain correction derived from ^{55}Fe random trigger spectra.</i>	65
5.8	<i>Mean energy calibration factor.</i>	65
5.9	<i>100 GeV proton single tube energy spectrum.</i>	66
5.10	<i>20 GeV electron single tube energy spectrum; Radiator test results.</i>	67
5.11	<i>Comparison of 20 and 80 GeV electron spectra.</i>	68
5.12	<i>The Cluster Counting method.</i>	69
5.13	<i>p^+-rejection as a function of e^--efficiency.</i>	70
5.14	<i>Hit-Cut distributions in comparison with binomial distributions.</i>	71
5.15	<i>Selection cut adjustment.</i>	72
5.16	<i>Likelihood distributions for protons and electrons.</i>	73
5.17	<i>Likelihood proton rejection as a function of electron efficiency.</i>	74
5.18	<i>Proton rejection as a function of beam energy.</i>	75
5.19	<i>Comparison of the 160 GeV proton spectra from X7 and H6 beamtests.</i>	76
5.20	<i>Proton rejection as a function of active layer number.</i>	77
5.21	<i>Single tube energy spectra measured at various Lorentz factors.</i>	78
5.22	<i>Particle rejections as a functions of the Lorentz factor.</i>	79
6.1	<i>Energy transfer distributions for the ionisation energy loss simulation.</i>	82
6.2	<i>Integral number of generated TR.</i>	83
6.3	<i>The Prototype as defined for the MC simulations.</i>	84
6.4	<i>Correction of the number of hits on the Y-track.</i>	85
6.5	<i>Comparison of Data and "first" MC single tube energy spectra.</i>	86
6.6	<i>Adjustment of ionisation energy loss simulation; cubic interpolation.</i>	88

6.7	Comparison of Data and adjusted MC proton spectra.	89
6.8	Comparison of Data and partly adjusted MC electron spectra.	90
6.9	Comparison of detected TR Photon energies before and after tuning.	91
6.10	Comparison of the Data and final MC electron single tube energy spectra.	92
6.11	Comparison of the Data and final MC Pion and Muon energy spectra.	93
6.12	Comparison of MC and data <i>Hcut</i> distributions.	94
6.13	Cluster Counting: MC and data proton rejections versus beam energy.	95
6.14	Comparison of MC and data likelihood distributions.	96
6.15	Likelihood: MC and data proton rejections versus beam energy.	97
6.16	<i>MC and data particle rejection factors versus Lorentz factor, γ.</i>	97
6.17	Likelihood: "MC2" and Data proton rejections versus beam energy.	99
7.1	<i>MC and Data particle rejection factors versus Lorentz factor γ.</i>	103

Bibliography

- [1] B.W. Carroll, D.A. Ostlie. *An Introduction to Modern Astrophysics*. Addison Wesley, 1996, ISBN: 0-201-54730-9.
- [2] NASA and The Hubble Heritage Team (STScI). *A Grazing Encounter between two Spiral Galaxies*. <http://heritage.stsci.edu/1999/41/table.html>
- [3] Malcolm S. Longair. *Our Evolving Universe*. Cambridge University Press, 1996, ISBN: 0-521-55091-2.
- [4] J. Silk. *A short History of the Universe*. Scientific American Library, New York, 1994, ISBN: 0-7167-6020-7.
- [5] W. deBoer. *Positron Fraction from Dark Matter Annihilation in the CSSM*. Proceedings for the SUSY02, The international Conference on Supersymmetry and Unification of fundamental Interactions, Desy (Hamburg), 2002.
- [6] G.L. Kane et al. *Supersymmetry and the positron excess in cosmic rays*. Physical Review **D 65** (2002) 577.
- [7] NASA Human Spaceflight. <http://spaceflight.nasa.gov/gallery/images/station/index.html>.
- [8] *The International Space Station: An Overview*. NASA Facts, IS-1999-06-ISS022, June 1999. <http://spaceflight.nasa.gov/spaceneeds/factsheets/index.html>.
- [9] A. Cohen et. al. A Matter-Anti-Matter Universe? *arXiv:astro-ph/9707087 v2*, 1997.
- [10] A. Yamamoto et. al. *BESS-Polar Long Duration Flights in Antarctica*. Proceedings of the 27th ICRC (Hamburg), p. 2135, 2001.
- [11] AMS Collaboration et. al. AMS on ISS, Part I, Results from the test flight on the Space Shuttle. Physics Reports, Vol. **366,6** (Aug. 2002) 331-404.
- [12] S. Straulino et al. *The PAMELA Experiment on Satellite and its Capability in Cosmic Rays Measurements*. Nucl. Inst. and Meth. **A 478** (2002) 114.
- [13] C. Lefevre, J. Gillies. *Back to Creation - the story of the Big Bang*. <http://outreach.web.cern.ch/outreach/public/cern/PicturePacks/BigBang.html>.
- [14] Paul A. M. Dirac. *Theory of electrons and positrons*. Nobel Lecture, Dec. 12, 1933. Nobel Lectures, Physics 1922-1941; Elsevier Publishing Company. <http://www.nobel.se/physics/laureates/1933/dirac-lecture.html>.

-
- [15] R. Hagedorn *Cargese Lectures in Physics* **6** (1973) 643.
- [16] K. Hagiwara et al. *The Review of Particle Physics*.
Physical Review **D 66** (2002) 010001. <http://pdg.lbl.gov/pdg.html>.
- [17] C.L. Bennett et al. *First Year WMAP Observations: Preliminary Maps and Basic Results*. arXiv:astro-ph/0302207v2 (2003).
- [18] James E. Hill et al. *Recent Results from Experiments Using the Super-K. Detector*.
Proceedings of the 3rd Intern. Conference on DM in Astro and Particle Physics.
ed. H.Klapdor-Kleingrothaus, (Springer, Heidelberg 2000).
- [19] J. Borger et al. *The Sudbury Neutrino Observatory*.
Nucl. Inst. and Meth. **A 449** (2000) 172-207.
- [20] F. Pilo et al. *Electromagnetic Calorimeter for the AMS-02 Experiment*.
Talk at 1st Space Part Conference, Elba, May 2002. (Proceedings in Preparation)
<http://www.pg.infn.it/spacepart/presentazioni/presentazioni.html>.
- [21] S. Ting. *The Alpha Magnetic Spectrometer*. unpubl. Report. MIT, May 1998.
<http://ams.pg.infn.it/ams-italy/pub/index1.htm>
- [22] R. Becker. *AMS II Mechanical Integration Homepage*.
Internet: <http://home.cern.ch/~rbecker/AMSII.html>, 2002.
- [23] S. Fopp. *Dissertation in Preparation*. unpubl. PhD thesis, RWTH Aachen, 2003.
- [24] R. Battiston. *Astroparticle Physics in Space with AMS-02*.
Talk at 1st Space Part Conference, Elba, May 2002. (Proceedings in Preparation)
<http://www.pg.infn.it/spacepart/presentazioni/presentazioni.html>.
- [25] D. Rapin. *The AMS Microstrip Silicon Tracker*.
Proceedings of the 27th ICRC (Hamburg), p. 2206, 2001.
- [26] J. Vandenhirtz et al. *Space flight experience with the AMS infrared tracker alignment system*.
Proceedings of the 27th ICRC (Hamburg), p. 2197, 2001.
- [27] B. Blau et al. *Status of the AMS-02 Superconducting Magnet*.
Talk at 1st Space Part Conference, Elba, May 2002. (Proceedings in Preparation)
<http://www.pg.infn.it/spacepart/presentazioni/presentazioni.html>.
- [28] S. Schael et al. *AMS02 ACC Progress Report*. unpubl. technical Report.
I. Physikalisches Institut of RWTH Aachen, 2001.
<http://accms04.physik.rwth-aachen.de/~schael/reports.html>.
- [29] L. Baldini. *The AMS Time of Flight System*.
Proceedings of the 27th ICRC (Hamburg), p. 2211, 2001.
- [30] J.Casaus. *Performance of the AMS-RICH prototype*.
Talk at 1st Space Part Conference, Elba, May 2002. (Proceedings in Preparation)
<http://www.pg.infn.it/spacepart/presentazioni/presentazioni.html>.

- [31] W. Struczinski. *Identifizierung hochenergetischer Teilchen d. Übergangsstrahlung*. III. Physikalisches Institut der RWTH Aachen, 1986. habilitation thesis.
- [32] B. Dolgoschein. *Transition radiation detectors and particle identification*. Nucl. Inst. and Meth. **A 252** (1986) 137-144.
- [33] B. Dolgoschein. *Transition radiation detectors*. Nucl. Inst. and Meth. **A 326** (1993) 434-469.
- [34] S. Fopp. *Untersuchungen zur Entwicklung eines Übergangsstrahlungsdetektors für das AMS-Experiment*. Master Thesis. I. Physikalisches Institut of RWTH-Aachen, Jan. 1999. published: PITHA 99/3.
- [35] M. Pindo. Nucl. Inst. and Meth. **A 395** (1997) 360 ff.
- [36] The Particle Data Group. *Review of Particle Physics*. The European Physics Journal C, 2000. Vol. 15, Number 1-4.
- [37] National Institute of Standards and Technology (NIST). *Stopping Power Calculations for Protons (PSTAR) and Electrons (ESTAR) in various Materials*. Internet: <http://physics.nist.gov/PhysRefData/Star/Text/programs.html>, 1996.
- [38] K. Siegbahn. *Alpha-, Beta-, and Gamma-Ray Spectroscopy*. 1. North-Holland Publishing Company Amsterdam, 1965.
- [39] J.H. Hubbell, S.M. Seltzer. *Tables of X-Ray Mass Attenuation Coefficients and Mass Energy-Absorption Coefficients*. Physics Reference Data, U.S. Department of Commerce, NISTIR 5632, 1996.
- [40] W. Leo. *Techniques for Nucl. and Part. Physics Experiments*. Springer Verlag, 1987.
- [41] Th. Siedenburg. private Communication.
- [42] ATLAS Collaboration. *ATLAS Inner Detector, Technical Design Report (TDR)*. CERN/LHC/97-17, April 1997, Vol. II. Page 637 ff.
- [43] J. Orboeck. *Untersuchungen an einem ortsauflösenden Prototypen für den Übergangsstrahlungsdetektor des AMS Exp.* unpubl. Master Thesis, RWTH Aachen, 1999.
- [44] K. Lübelmeyer et. al. *Wire fixation for Proportional and Drift Chambers Using a Cu – Te Alloy*. published: PITHA 93/25, RWTH Aachen, 1993.
- [45] V. Commichau. *Universal Slow Control Module USCM V03/S3b for AMS-II*. unpubl. technical Report. III. Physikalisches Institut, RWTH Aachen, 2002. http://www.physik.rwth-aachen.de/group/IIIphys/Electronics/AMS-II/HARDWARE/USCM_V3S3b_flight.pdf
- [46] S. Schael et al. *Status Report of the AMS-02 Transition Radiation Detector (TRD)*. unpubl. technical Report. I. Physikalisches Institut of RWTH Aachen, 2001.

-
- [47] AMS TRD Page. *Front End Electronics*.
<http://accms04.physik.rwth-aachen.de/%7Eams/ams02/Electronics/index.html>
- [48] U. Becker. *TRD Gas System Summary*. unpubl. technical Report.
MIT Laboratory for Nuclear Science, <http://ams.cern.ch/AMS/TRDGas/>.
- [49] M. Wlochal. private Communication.
- [50] NASA *Alpha Magnetic Spectrometer - Structural Verification Plan for the Space Transportation System and the International Space Station*. unpubl. techn. Report.
http://ams.cern.ch/AMS/INT/ICD/ams-02_svprvb.pdf
- [51] Th. Kirn. private Communication.
- [52] V. Saveliev. *Particle Identification via Transition Radiation and Detectors*.
Nucl. Inst. and Meth. **A 453** (2000) 346-352.
- [53] R. Edenhofer. *Untersuchungen an einem Prototypen des Übergangsstrahlungs-Detektors für das AMS Projekt*. unpubl. Master Thesis, RWTH Aachen, 2000.
- [54] K. Lübelmeyer et al. *A wiring system for mass production of drift and proportional chambers*. Nucl. Inst. and Meth. **A 345** (1994) 256-261.
- [55] W. Karpinski. *Drahtspannungsmessgerät*.
unpubl. technical Report. I. Physikalisches Institut, RWTH Aachen.
- [56] L. Gatignon. *The West Experimental Area at the CERN SPS*.
CERN SL-2000-016 ea, 2000.
- [57] K. Elsener. *Short Introduction to the use of the H6 Beam*.
unpubl. technical Report, CERN. <http://atlas.web.cern.ch/Atlas/GROUPS/GENERAL/TESTBEAM/references/H6manual.html>.
- [58] C. Bovet et al. *The CEDAR Counters for Particle Identification in the SPS secondary Beams: A Description and an operational Manual*.
technical Report. CERN 82-13, 1982.
- [59] J. Moyal. *Theory of Ionization Fluctuations*. *Phil.Mag.* **46** (1955) 263.
- [60] T. Kirn. *AMS02 TRD-Meeting*. Presentation, Nov. 2000.
- [61] L. Gatignon. private Communication.
- [62] S. Schael. *B Physics at the Z-Resonance*. Physics Letters **313,6** (1999) 294-366.
- [63] R. Brun et al. *GEANT*. CERN DD/EE/84-1 (Revised), 1987.
GEANT Version 3.21 is used.
- [64] V. Ermilova et al. *Fluctuations of the most probable value of relativistic charged particle energy loss in thin gas layers*. Nucl. Inst. and Meth. **A 145** (1977) 555-563.

-
- [65] M. Cherry. *Transition Radiation from relativistic Electrons in periodic Radiators*. Physical Review Letters **D 10** (1974) 3594 ff.
- [66] G.M. Garibian. Nucl. Inst. and Meth. **A 125** (1975) 133 ff.
- [67] H. Fesefeldt. private Communication.
- [68] R. Webb et al. *Production of Nucleon Resonances by single Diffraction Dissociation at the CERN ISR*. Physics Letters **B 55** (1974) 331

Curriculum Vitae

Personal Data:

Name: Jörg Orboeck
Date of Birth: 8. August 1972
Place of Birth: Vechta
Parents: Anke Orboeck, nee Müller
Jörg Orboeck

Schooling:

'79 – '83 Grundschole Düsseldorf Lörick (Primary School)
'83 – '92 Städtisches Comenius-Gymnasium, Düsseldorf
June '92 Graduation: Allgemeine Hochschulreife (Abitur)

Military Service:

'92 – '93 Luftwaffe (German Airforce)

University Education:

Oct. '93 Enrolment to Physics studies at RWTH Aachen
April '96 Pre-Diploma Exams, Subject: Physics
Sept.'96 – July '97 2 Semesters at the "University of Liverpool"
Sept. '98 – Aug. '99 Diploma thesis, Subject: Detetctor R&D for the AMS Exp., at I. Physikalisches Institut of RWTH Aachen (Prof. Lübelismeyer)
Sept. '99 Graduation: Diploma
Oct. '99 – July 2003 PhD Student at I. Physikalisches Institut of RWTH Aachen
May, 28th 2003 Day of PhD Exam